
Magnetic Field Control and Laser Frequency Stabilization for Strontium Magneto-Optical Traps

Rodrigo González Escudero



Munich 2016

Magnetfeldkontrolle und Laserfrequenzstabilisierung für Strontium Magneto-Optische Fallen

Masterarbeit an der Fakultät für Physik
Ludwig-Maximilians-Universität München
Max-Planck-Institut für Quantenoptik

vorgelegt von
RODRIGO GONZÁLEZ ESCUDERO
aus Madrid, Spanien

München, den 15.09.2016

Contents

Abstract	1
1 Introduction	3
1.1 Outline	4
2 Laser Cooling of Strontium Atoms	5
2.1 Semi-Classical Theory of Light-Atom Interaction	5
2.2 The Magneto-Optical Trap	8
2.3 Laser Cooling of ^{88}Sr	13
2.3.1 The Blue Magneto-Optical Trap	13
2.3.2 The Red Magneto-Optical Trap	14
3 Spectroscopy of Transitions between Electronically Excited States in ^{88}Sr	17
3.1 Spectroscopy and Laser Frequency Stabilization to the $5s\ 5p\ ^3P_2 \rightarrow 5s\ 6s\ ^3S_1$ Transition	17
3.1.1 Doppler-Free Saturation Spectroscopy	17
3.1.2 Experimental Setup	24
3.1.3 Results	26
3.1.4 Data Analysis	29
3.2 Spectroscopy and Laser Frequency Stabilization to the $5s\ 5p\ ^3P_0 \rightarrow 5s\ 6s\ ^3S_1$ Transition.	31
3.2.1 Frequency Modulation Spectroscopy Measurements	31
3.2.2 Overview of the Error Signal Generation	33
3.2.3 Setup	37
3.2.4 Results	38
3.3 Conclusions	42

4	A Magnetic Field System for Cooling and Trapping of ^{88}Sr	45
4.1	Design considerations	47
4.1.1	Field Stability	47
4.1.2	Switching Time	48
4.1.3	Mechanical Stability	51
4.1.4	Dissipated Electrical Power	55
4.2	Current Control	56
4.3	Fast Switching Circuit	59
4.4	Coil Geometry Optimization	64
4.5	Coil Mount Design	69
4.6	Power Dissipation	70
4.7	Compensation Coils	72
	Acknowledgements	75
	Appendices	77
	Bibliography	85

Abstract

In this thesis I report my work done in Immanuel Bloch's group under the supervision of Dr. Sebastian Blatt at the Max-Planck-Institute for Quantum Optics. This work was part of my Master program at the Ludwig Maximilians University of Munich (Ludwig-Maximilians-Universität München). My work is split into two main projects. I report on the development of a magnetic field system for cooling and trapping of strontium atoms. I designed a system for precise current control and fast switching of inductive loads. Additionally I developed a laser system for frequency stabilization of diode lasers to transitions between electronically excited states in strontium. For one of the transitions I reproduce already existing results, for the other I develop a method for laser frequency stabilization based on enhancing the population of the lower level of the transition by optical pumping.

Chapter 1

Introduction

Proper understanding of quantum phenomena is a vital part of science and technology. One of the most prominent examples is the research on semiconductor materials and the development of the transistor for which Shockley, Bardeen and Brattain received the Nobel price of physics in 1956. Many quantum mechanical effects however, are still not fully understood. The problem is that the computational effort required to numerically describe a quantum system scales exponentially with the number of components. A numerical description of a quantum system is thus limited to a small number of particles.

In 1982 Richard Feynman proposed a solution to this problem [1]. His idea was to artificially engineer a quantum system that presents the same dynamics one wishes to study. One could prepare the system in a state of interest and measure its output at different times. To do this one requires a high level of controllability, to create the desired system, prepare the quantum states of interest, and measure the different observables.

Ultracold atoms trapped in optical lattices are ideal for this purpose. In these systems, a standing wave of light creates a periodic potential that holds the atoms. By changing the intensity or the frequency of the radiation one can control this potential. Moreover, it is also possible to address single sites in the lattice, controlling the atoms at each site and manipulating their quantum state [2]. Using these tools, the authors of Ref. [3] were able to show the existence of a phase transition in a regime where accurate numerical results are not possible. In this context quantum simulation is already a reality.

Due to their simpler electronic structure all of the initial experiments were done with alkali metals. This trend is now changing, and as understanding progresses, more complex atoms are being used. Alkaline-earth atoms for example are now starting to be used as they present properties not found in alkali metals.

In strontium for example, the existence of long lived metastable states, narrowband transitions [4], and the decoupling between the nuclear spin and the electronic states [5] make this atom a good candidate for the study of quantum many-body physics. The developments on strontium based optical atomic clocks [6] show that many of its properties are already well understood and that a high degree of controllability is possible.

In our experiment we intend to study quantum many-body physics in optical lattices

using this atom. To do this we want to be able to cool all of the four natural occurring isotopes of strontium down to degeneracy. Moreover we intend to explore the dynamics of the strontium atom in optical lattices. We want to enhance the lattice potential using a cavity, as this will allow us to obtain larger and more homogeneous systems than the ones currently available. We also intend to use the recently developed techniques of high resolution imaging for the atoms in the lattice [7, 8].

1.1 Outline

In the initial part of the experiment we intend to cool down atoms to the μK regime using magneto-optical traps. In this thesis I report my work on the initial parts of the experiment.

In Chapter 2, I describe the techniques used for laser cooling of strontium relevant for understanding my thesis. Here I will focus on the ^{88}Sr isotope. Although we intend to produce degenerate gases of all the isotopes, my work was closely connected to ^{88}Sr isotope and only knowledge of it is required.

Chapter 3 is divided into two main parts. In the first part of the project I reproduce the results obtained by the authors of Ref. [9] for laser locking on the $5s\ 5p\ ^3P_2 \rightarrow 5s\ 6s\ ^3S_1$ transition. This technique is based on the generation of excited state atoms using the discharge in a hollow cathode lamp.

As I did not find any setup for spectroscopy of the strontium $5s\ 5p\ ^3P_0 \rightarrow 5s\ 6s\ ^3S_1$ transition in literature, in the second part I develop a method for spectroscopy and frequency stabilization to this transition. This method is based on detecting a population increase created by a laser resonant with the $5s\ 5p\ ^3P_2 \rightarrow 5s\ 6s\ ^3S_1$ transition. This population increase is detected on the absorption spectrum of a laser resonant with the $5s\ 5p\ ^3P_0 \rightarrow 5s\ 6s\ ^3S_1$ transition. I also analyse the dependence of the error signal on the different experimental parameters.

In Chapter 4, I describe the setup of the magnetic field system in our experiment. I study some of the most important parameters that need to be taken into account when designing a magnetic field system for laser cooling of ^{88}Sr . These are based on three basic aspects: high current stability, fast switching speed of the magnetic field and high mechanical stability. Based on these ideas I explain how these issues were solved. I also explain how I optimized the coil geometry to obtain the most ideal parameters for our system.

Chapter 2

Laser Cooling of Strontium Atoms

Understanding the interaction of light with matter is key to comprehend the basics of laser cooling of neutral atoms. This interaction can be studied with a simple model of a two level atom within the dipole approximation. In this framework many of the important phenomena relevant for laser cooling and trapping of neutral atoms can be understood. In this Chapter, I will describe the principles of light-matter interaction and laser cooling required to understand this thesis. Following that, I will explain the specifics relevant for laser cooling of strontium. I will focus on the ^{88}Sr isotope as it is the most naturally abundant isotope of strontium [4] and it is the easiest one to cool down to the μK regime in a magneto-optical trap.

2.1 Semi-Classical Theory of Light-Atom Interaction

The length scale of variation of an electromagnetic wave is characterized by the wavelength of the radiation. For optical frequencies and a thermal gas of atoms at room temperature, the wavelength of the light is much larger than the extent of the atomic wavefunction. The interaction of an atom with the electromagnetic field can then be understood as spatially independent (this limit is known as the dipole approximation). Within this approximation the interaction of light with matter can be described by the following Hamiltonian [10]:

$$\begin{aligned} H(t) &= \frac{1}{2m} \sum_{i=1}^N [\vec{p}_i - e \cdot \vec{A}(t)] + V \\ &= \frac{1}{2m} \sum_{i=1}^N \vec{p}_i^2 - \frac{e}{m} \vec{A}(t) \cdot \sum_{i=1}^N \vec{p}_i + \frac{e^2 N}{2m} \vec{A}(t)^2 + V, \end{aligned} \quad (2.1)$$

where \vec{p}_i is the momentum of each of the valence electrons of the atom, $\vec{A}(t)$ is the vector potential of the electromagnetic wave, e is the charge of the electron, m is the electron mass, N is the total number of valence electrons and V is the Coulomb potential due to the charge of the nucleus. The interaction Hamiltonian of Eq. (2.1) takes the form:

$$H_I = -\frac{e}{m} \vec{A}(t) \cdot \sum_{i=1}^N \vec{p}_i + \frac{e^2 N}{2m} \vec{A}(t)^2, \quad (2.2)$$

and the Schrödinger equation becomes:

$$i\hbar \frac{\partial}{\partial t} |\psi\rangle = \left[\frac{1}{2m} \sum_{i=1}^N \vec{p}_i^2 + V + H_I \right] |\psi\rangle, \quad (2.3)$$

where $|\psi\rangle$ is the wavefunction of the atom and \hbar is the reduced Planck constant. Performing the transformation¹:

$$|\psi\rangle = \exp\left(-\frac{ie}{\hbar} \vec{A}(t) \sum_{i=1}^N \vec{r}_i\right) |\psi\rangle_L, \quad (2.4)$$

one obtains the following Hamiltonian:

$$\begin{aligned} H &= \frac{1}{2m} \sum_{i=1}^N \vec{p}_i^2 + V + e \vec{E}(t) \cdot \sum_{i=1}^N \vec{r}_i \equiv H_0 + H_I, \\ H_I &= -e \vec{E}(t) \cdot \sum_{i=1}^N \vec{r}_i = \vec{E}(t) \cdot \vec{D}, \\ H_0 &= \frac{1}{2m} \sum_{i=1}^N \vec{p}_i^2 + V, \end{aligned} \quad (2.5)$$

where \vec{r}_i is the position operator of the electrons, $\vec{E}(t)$ is the electric field of the wave and \vec{D} is the dipole operator given by:

$$\vec{D} = -e \sum_{i=1}^N \vec{r}_i. \quad (2.6)$$

Here, we have used that within the dipole approximation the electric field becomes:

$$\vec{E}(t) \approx \frac{\partial}{\partial t} \vec{A}(t), \quad (2.7)$$

as all the fields are position-independent [10]. Note that the interaction Hamiltonian H_I in Eq. (2.5) is just the classical energy of a dipole in an electric field.

In general, an analytic solution of Eq. (2.5) cannot be obtained. If the dynamics of the interaction are dominated by two quantum states which we will call $|g\rangle$ for the state with the lowest energy and $|e\rangle$ for the state with the highest energy, the Hamiltonian in Eq. (2.5) can be simplified to [11]:

$$H' = \frac{\hbar}{2} (-2\Delta |g'\rangle\langle g'| + \Omega_0 |g'\rangle\langle e'| + \Omega_0 |e'\rangle\langle g'|), \quad (2.8)$$

¹This transformation is known as length gauge.

where we have transformed to a rotating frame:

$$|g'\rangle = |g\rangle e^{-i\Delta t}, \quad |e'\rangle = |e\rangle e^{-i\Delta t}, \quad (2.9)$$

and performed the rotating wave approximation [12]. The Rabi frequency

$$\Omega_0 = \frac{e E_0}{\hbar} \langle e' | \vec{D} | g' \rangle \quad (2.10)$$

is a parameter that characterizes the coupling strength between the two quantum states and $\Delta = \omega_l - \omega_{eg}$ is the light detuning. Here ω_l is the light frequency, and $\omega_{eg} = \omega_e - \omega_g$, where $\hbar \omega_e$ is the energy of $|e'\rangle$ and $\hbar \omega_g$ is the energy of $|g'\rangle$.

According to the Von Neumann equation, the time evolution of the density matrix operator ρ follows the equation [13]:

$$i \hbar \frac{d\rho}{dt} = [H, \rho]. \quad (2.11)$$

Using the Hamiltonian introduced in Eq. (2.8) one obtains:

$$\frac{dw}{dt} = -i\Omega_0(\rho_{eg} - \rho_{ge}), \quad \frac{d\rho_{eg}}{dt} = -i\Delta\rho_{eg} - \frac{i\Omega_0}{2} w, \quad (2.12)$$

where we have introduced the population imbalance as $w = (\rho_{22} - \rho_{11})$. The density matrix formalism is useful as it allows us to accurately describe the properties of the atomic ensemble and to introduce the spontaneous decay of the atom, Γ . Following the approach given by the authors of Ref. [11], we obtain² :

$$\begin{aligned} \frac{dw}{dt} &= -\Gamma(w + 1) - i\Omega_0(\rho_{eg} - \rho_{ge}), \\ \frac{d\rho_{eg}}{dt} &= \left(i\Delta - \frac{\Gamma}{2}\right)\rho_{eg} - \frac{i\Omega_0}{2} w. \end{aligned} \quad (2.13)$$

These equations are known as the optical Bloch equations. Their steady state solution can be calculated by setting the left hand side of Eqs. (2.13) to zero:

$$\frac{dw}{dt} = 0, \quad \frac{d\rho_{eg}}{dt} = 0, \quad (2.14)$$

to obtain

$$\rho_{ee} = \frac{1}{2}(1 - w) = \frac{s_0/2}{1 + s_0 + 4\frac{\Delta^2}{\Gamma^2}}. \quad (2.15)$$

²The spontaneous decay as introduced here follows a phenomenological approach, to explain the results of the experiment. The rate of spontaneous decay can be derived from basic principles, within the framework of quantum electrodynamics or quantum optics. The theory is known as Wigner-Weisskopf theory of spontaneous emission [14].

Here we have introduced the saturation parameter s_0 :

$$s_0 \equiv \frac{I}{I_{sat}} \equiv \frac{2|\Omega_0|^2}{\Gamma^2}, \quad (2.16)$$

where I is the laser intensity and I_{sat} is the saturation intensity [11]:

$$I_{sat} = \frac{2 \pi^2 \hbar c \Gamma}{3\lambda^3}. \quad (2.17)$$

Here, c is the speed of light in vacuum and λ is the wavelength of the light. In the steady state the excitation rate and the decay rate are equal, and the total scattering rate of the light field becomes:

$$\Gamma_{sc} = \Gamma \rho_{ee} \frac{1}{2}(1 - w) = \Gamma \frac{s_0/2}{1 + s_0 + 4 \frac{\Delta^2}{\Gamma^2}}. \quad (2.18)$$

Equation (2.18) shows two different regimes. For low intensities, $s_0 \ll 1$ or equivalently $I \ll I_{sat}$, the scattering rate increases linearly with the saturation parameter as:

$$\Gamma_{sc} \approx \frac{\Gamma}{2} s_0 \frac{1}{1 + 4 \frac{\Delta^2}{\Gamma^2}}. \quad (2.19)$$

As can be seen in Fig. 2.1, when $s_0 \gg 1$, the scattering rate becomes independent of the light intensity and saturates to $\Gamma/2$. The full width half maximum (FWHM) of the profile increases as:

$$\text{FWHM} = \Gamma \sqrt{1 + s_0}. \quad (2.20)$$

This effect is known as power broadening. This will be the observed linewidth in a spectroscopy experiment like the one discussed in section 3.1.

2.2 The Magneto-Optical Trap

In this section we will introduce the working principle of a magneto-optical trap (MOT). A more detailed overview of the concepts introduced here can be found in Refs. [11, 15].

The force that a light field applies to a two level atom is:

$$\vec{F}(\Delta) = \hbar \vec{k} \Gamma_{sc}(\Delta), \quad (2.21)$$

where \vec{k} is the wavevector of the light and $\Gamma_{sc}(\Delta)$ is the scattering rate introduced in the previous section. Note that Eq. (2.21) assumes that the momentum gain due to spontaneous emission averages to zero, while the momentum transfer by the laser light is always in the direction of the light propagation, given by \vec{k} .

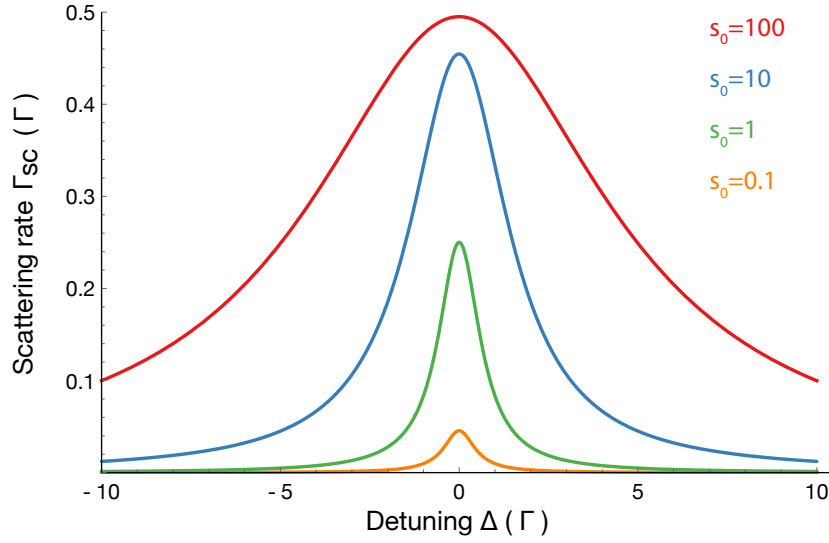


Figure 2.1: Scattering rate as a function of the detuning for different saturation parameters.

Atoms will only react to light when the Doppler shift ($\vec{k} \cdot \vec{v}$, where \vec{v} is the velocity of the atom) compensates the light detuning Δ , i.e. when $\Delta = \vec{k} \cdot \vec{v}$. Because of the Doppler shift, the scattering rate calculated of Eq. (2.18) becomes velocity-dependent:

$$\Gamma_{sc}(\Delta - \vec{k} \cdot \vec{v}) = \Gamma \frac{s_0/2}{1 + s_0 + 4 \frac{(\Delta - \vec{k} \cdot \vec{v})^2}{\Gamma^2}}, \quad (2.22)$$

The force applied to the atoms becomes:

$$\vec{F}(\vec{v}) = \hbar \vec{k} \Gamma_{sc}(\Delta - \vec{k} \cdot \vec{v}). \quad (2.23)$$

The force applied by two counter-propagating laser beams will be:

$$\begin{aligned} \vec{F}_t(\vec{v}) &= \vec{F}(\vec{v}) - \vec{F}(-\vec{v}) \\ &= \hbar \vec{k} \Gamma \frac{s_0}{2} \left(\frac{1}{1 + s_0 + 4 \frac{(\Delta - \vec{k} \cdot \vec{v})^2}{\Gamma^2}} - \frac{1}{1 + s_0 + 4 \frac{(\Delta + \vec{k} \cdot \vec{v})^2}{\Gamma^2}} \right). \end{aligned} \quad (2.24)$$

Figure 2.2 shows the resulting velocity-dependent force for red-detuned light with $\Delta = -\Gamma/2$ and $s_0 = 1/2$. Around $\vec{v} = 0$ this force is proportional to the velocity with a negative slope (blue dashed line). Equation (2.24) can be expanded around $\vec{v}=0$ to obtain:

$$\vec{F}(\vec{v}) = \frac{8 \hbar k^2 \Delta s_0 \vec{v}}{\Gamma (1 + s_0 + (2 \Delta/\Gamma)^2)} + \mathcal{O}(\vec{v}^3) \equiv \beta \vec{v} + \mathcal{O}(\vec{v}^3), \quad (2.25)$$

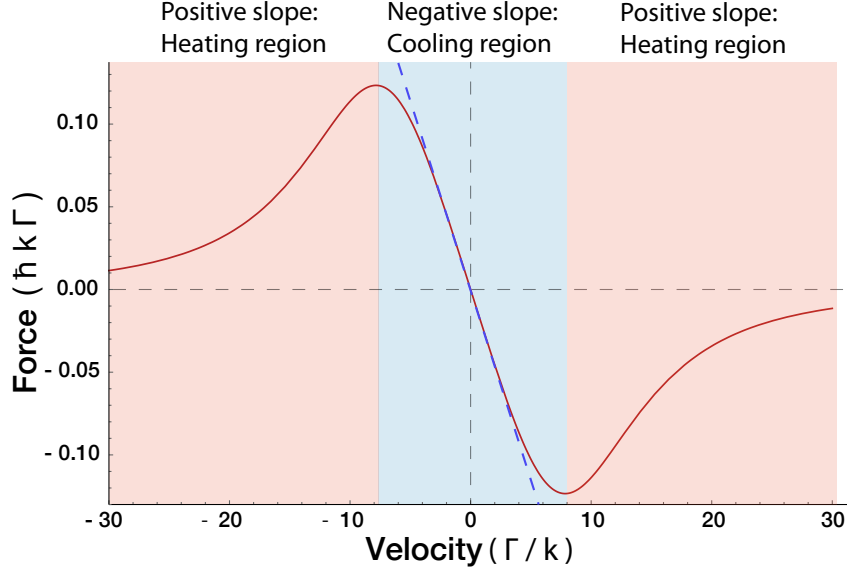


Figure 2.2: Two red-detuned counter-propagating beams will create a velocity-dependent force (solid red line) which can be estimated to be linear around $v = 0$ (dashed blue line). The parameters used here are $\Delta = -\Gamma/2$ and $s_0 = 1/2$. When the slope is negative the atoms will be slowed down (light blue regions) while when the slope is positive atoms will gain energy (red regions).

where β is the damping coefficient. For red detuned light $\Delta < 0$ this force opposes the velocity and the atoms are slowed down. This cooling process is known as optical molasses. Equation (2.25) indicates that the atoms will slow down to zero velocity. In reality the final velocity will not be zero. Although the average momentum gain due to spontaneous emission is zero, each single emission results in a momentum transfer of $\hbar \vec{k}$ to the atom in a random direction. This random walk in momentum space will limit the final temperature to be [11]:

$$T_d = \frac{\hbar \Gamma}{2 k_B}. \quad (2.26)$$

Here, we have used that the optimal detuning for cooling is $\Delta = -\Gamma/2$ [11]. Equation (2.26) seems to indicate that the ideal transition for cooling atoms is a narrow-line transition. Two details need to be considered:

- Laser cooling requires a damping coefficient which is negative. As can be seen in Fig. 2.2 this is only true between the two extrema. The positions of the extrema scale with Γ . Therefore a narrow-line transition will only be able to cool atoms with low velocities. For $\Delta \gg \Gamma \sqrt{1 + s_0}$ the position of these extrema is given by $v_c = \Delta/k$, where v_c is defined as the capture velocity.
- A more fundamental limit to the final temperature achievable by laser cooling will be given by the recoil limit. An atom at rest after absorbing a photon will need to emit it, gaining momentum in a random direction. The recoil temperature limit

is given by $T_r = 2 E_r/k_B$, where $E_r = \hbar^2 k^2/2m$ is the recoil energy. As shown in Ref. [16] the limit of laser cooling will be given by $T_r/2$.

The difference between the Doppler temperature limit and the recoil limit can be confusing. In the first case, the limit is given by the average momentum gain by scattering of multiple photons, this being a statistical effect, while in the second case, the limit is given by the momentum gain obtained by the scattering of single photons.

The force given in Eq. (2.24) is position-independent, and therefore not confining. Applying an external magnetic field will shift the energy of each magnetic sublevel due to the Zeeman effect as [10]:

$$\Delta E = \mu_B g_j m_j B, \quad (2.27)$$

where μ_B is the Bohr magneton, g_j is the Landé g factor, B is the external magnetic field and m_j is the z component of the total angular momentum (j is the quantum number related to the total angular momentum of the atom). The main working principle of the MOT is to use a position dependent magnetic field of the form $B(x) = P x$ to generate a restoring force. In this case the light detuning becomes:

$$\tilde{\Delta} = \omega_l - \omega_{eg} + \mu_B g_j m_j P x, \quad (2.28)$$

where $\tilde{\Delta}$ is the shifted detuning due to the Zeeman effect. Using this new detuning Eq. (2.24) becomes:

$$\vec{F}(\vec{v}, x) = \hbar \vec{k} \Gamma \frac{s_0}{2} \left(+ \frac{1}{1 + s_0 + 4 (\Delta - \vec{k} \cdot \vec{v} - \mu_B g_j m_j P x/\hbar)^2/\Gamma^2} - \frac{1}{1 + s_0 + 4 (\Delta + \vec{k} \cdot \vec{v} + \mu_B g_j m_j P x/\hbar)^2/\Gamma^2} \right) \quad (2.29)$$

and expanding Eq. (2.29) around $\vec{v} = 0$ and $\vec{x} = 0$ we obtain:

$$\vec{F}(\vec{v}, \vec{x}) \approx \beta \vec{v} - \kappa \vec{x}, \quad (2.30)$$

where β is the same damping coefficient as in the previous section and we identify κ as a spring constant with the form:

$$\kappa = \frac{g_j m_j P}{\hbar k} \beta. \quad (2.31)$$

The size of the MOT region where atoms in state m_j interact with light is given by:

$$\Delta x = 2 \frac{\hbar \Delta}{\mu_B g_j m_j P'} \quad (2.32)$$

As shown in Fig. 2.3, the typical setup of a MOT will employ 3 pairs of laser beams and two coils with counter-propagating currents to obtain a confining force in three dimensions. The magnetic field gradient is generated by this coil pair. As we will explain

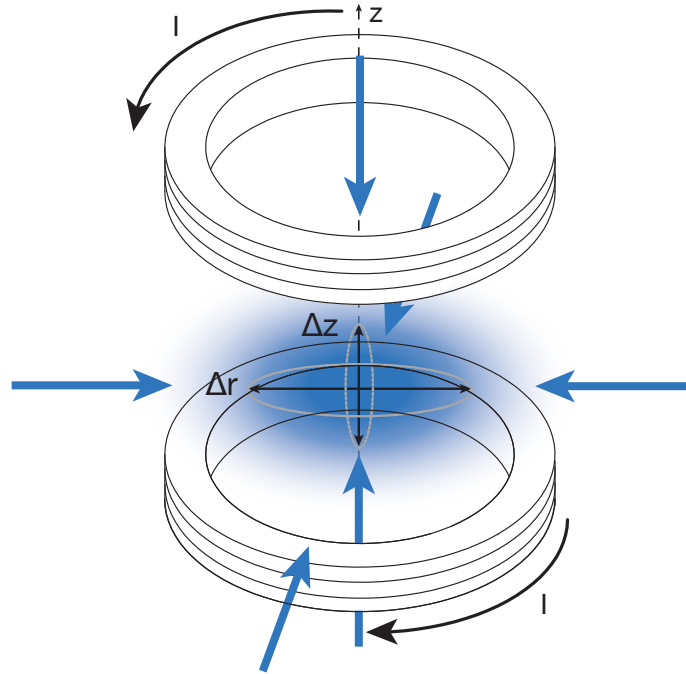


Figure 2.3: A pair of coils with counter propagating currents generates a field gradient around the origin. Since the size of the MOT cloud is inversely proportional to the field gradient, the cloud will be asymmetric. The size of the atomic cloud is not drawn to scale.

in Chapter 4 the magnetic field gradients in the radial and axial directions follow the relation:

$$\left| \frac{d\vec{B}}{dz} \right| = 2 \left| \frac{d\vec{B}}{dr} \right|, \quad (2.33)$$

where z is the coordinate along the symmetry axis of the coils and r is the radial distance to the symmetry axis. Therefore, the region where atoms interact with light resembles an ellipsoid with major and minor axes given by (see Fig. 2.3):

$$\Delta z = 2 \frac{\hbar \Delta}{\mu_B g_j m_j dB/dz'}, \quad (2.34)$$

$$\Delta r = 2 \Delta z$$

2.3 Laser Cooling of ^{88}Sr

Laser cooling of ^{88}Sr is usually done in three steps: Atoms effusing from the oven are slowed down in a Zeeman slower [11] and loaded into a MOT resonant with the $5s^2\ ^1S_0 \rightarrow 5s\ 5p\ ^1P_1$ transition (blue MOT). In this blue MOT atoms are cooled down to $T \approx 1\text{mK}$ [4].

To achieve lower temperatures after the blue MOT stage, atoms are loaded into a narrowband MOT on the $5s^2\ ^1S_0 \rightarrow 5s\ 5p\ ^3P_1$ transition (red MOT). The final temperature of the red MOT depends on the laser intensity, its detuning and the isotope. However, in Ref. [17] temperatures as low as $250 \pm 20\ \text{nK}$ are reported.

While the atomic oven and the Zeeman slower are two fundamental parts of the experiment, understanding of these two stages is not fundamental for understanding this thesis, therefore they will not be discussed here. For an explanation of the working principle of our Zeeman slower and our atomic oven see Ref. [18].

In this section, I will focus on the blue and red MOT for ^{88}Sr . This isotope is the most simple to cool due to its high natural abundance and its more simple internal structure because of the lack of hyperfine structure (see Table 2.1). However, also the other isotopes can be very interesting, for example ^{87}Sr based atomic clocks hold the record of relative precision in the measurement of frequency [6].

Isotope	Nuclear Spin	Natural abundance
^{88}Sr	0	82.58 %
^{87}Sr	9/2	7.00 %
^{86}Sr	0	9.86 %
^{84}Sr	0	0.56 %

Table 2.1: Data for the isotopes of Strontium. The data is taken from Ref. [19].

2.3.1 The Blue Magneto-Optical Trap

The blue MOT is operated on the $5s^2\ ^1S_0 \rightarrow 5s\ 5p\ ^1P_1$ transition, the linewidth of which is $\Gamma = 2\pi \times 30.5\ \text{MHz}$. This corresponds to a Doppler temperature of $720\ \mu\text{K}$ which is larger than the recoil temperature of the transition $T_r = 1.02\ \mu\text{K}$. The final temperature of the cloud, as reported in Ref. [4] is $1\ \text{mK}$.

The blue MOT transition ($5s^2\ ^1S_0 \rightarrow 5s\ 5p\ ^1P_1$) is not completely closed as atoms can decay into the $5s\ 5p\ ^3P_2$ and the $5s\ 5p\ ^3P_1$ states through the $4d\ ^1D_2$ decay channel (see Fig. 2.4). Atoms in the $5s\ 5p\ ^3P_1$ state will relax back to the ground state on a timescale of several ms and thus return to the main cooling transition. Atoms in the

$5s\ 5p\ ^3P_2$ state, however, will be stored in this state for several minutes and will be lost from the cooling transition.

As can be seen in Fig. 2.4, an atom will reach the $4d\ ^1D_2$ state every 50,000 scattering events. The probability for an atom to decay from the $5s\ 4d\ ^1D_2$ state to the $5s\ 5p\ ^3P_2$ state is $1/3$. Therefore, on average, every $\sim 150,000$ scattering events an atom will be stored in the $5s\ 5p\ ^3P_2$ state. Although the effect is small, taking into account the scattering rate of the blue MOT, which is on the order of half the linewidth of the $5s^2\ ^1S_0 \rightarrow 5s\ 5p\ ^1P_1$ transition (see section 2.1), we can estimate the lifetime of an atom in the blue MOT to be:

$$\tau_b \approx \frac{150,000}{\Gamma_b/2} \approx 1.6\ \text{ms}, \quad (2.35)$$

where Γ_b is the linewidth of the $5s^2\ ^1S_0 \rightarrow 5s\ 5p\ ^1P_1$ transition. Atoms stored in the $5s\ 5p\ ^3P_2$ state must return to the ground state. This can be done by optically pumping them to the $5s\ 6s\ ^3S_1$ excited state using a 707 nm laser. From the $5s\ 6s\ ^3S_1$ state atoms can decay to the $5s\ 5p\ ^3P_1$ and from here return to the $5s^2\ ^1S_0$ state. This approach has one drawback, as the $5s\ 6s\ ^3S_1$ state is also coupled to the $5s\ 5p\ ^3P_0$ state. This state has a lifetime of ~ 150 s, therefore an additional laser of 679 nm is required to optically pump these atoms to the $5s\ 6s\ ^3S_1$ state. Using these two lasers the authors of Ref. [20] measure an increase of the steady state population of the blue MOT by a factor of 10.

Other authors use different transitions to optically pump these atoms back to the ground state. In Ref. [4] a review of all the possible transitions that can be used for this purpose is given.

2.3.2 The Red Magneto-Optical Trap

To obtain much lower temperatures than in the blue MOT, a MOT on the $5s^2\ ^1S_0 \rightarrow 5s\ 5p\ ^3P_1$ transition (red MOT) is used. The linewidth of the red MOT transition, $\Gamma = 2\ \pi \times 7.4$ kHz, is much narrower than the linewidth of the blue MOT transition and therefore a lower final temperature is obtained. In this case the recoil temperature, $T_r = 460$ nK, is larger than the Doppler temperature $T_D = 180$ nK. Experimentally, temperatures as low as 250 ± 20 nK are obtained [17].

The capture velocity of the red MOT, $v_c = \frac{\Gamma}{2k}$ is lower than the average thermal velocity of the atoms at the temperature of the blue MOT. To increase the capture velocity of the red MOT the linewidth of the red MOT lasers is artificially broadened which can increase the fraction of atoms captured [4].

Moreover, the optimal magnetic field gradient for the red MOT of 2 G/cm is very different than the required gradient for the blue MOT 52 G/cm. To prevent atom losses while loading the blue MOT, the magnetic field needs to be switched on a timescale of 0.1 ms [4].

To achieve low temperatures the red MOT usually goes through a complicated se-

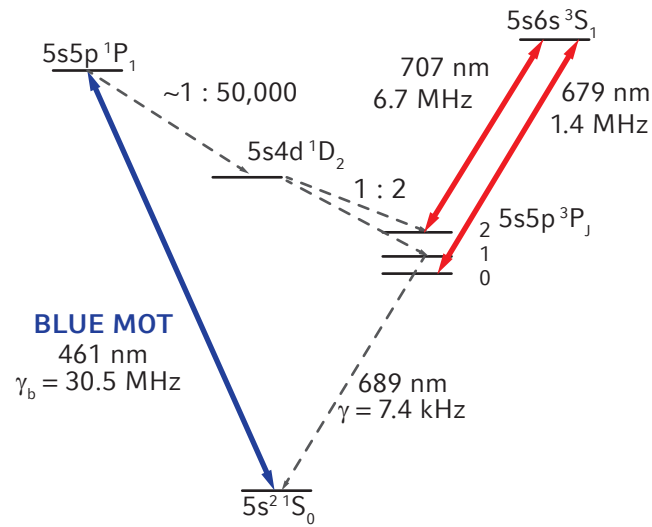


Figure 2.4: Simplified diagram of the energy level structure of the strontium atom. The linewidths of the transitions involving the triplet states and the $5s\ 6s\ ^3S_1$ state were taken from Ref. [21]. The rest of the information presented in this diagram was taken from Ref. [4]. The grey dashed lines denote spontaneously decaying transitions in the blue MOT cooling stage. The colored lines indicate driven transitions.

quence in the magnetic field gradient and the laser parameters. A description of the red MOT experimental sequence is given by Refs. [4, 18] and will not be described here.

Chapter 3

Spectroscopy of Transitions between Electronically Excited States in ^{88}Sr

As described in Chapter 2, the blue magneto optical trap (MOT) requires two extra lasers resonant with the $5s\ 5p\ ^3P_2 \rightarrow 5s\ 6s\ ^3S_1$ and $5s\ 5p\ ^3P_0 \rightarrow 5s\ 6s\ ^3S_1$ transitions. In this Chapter we will describe the techniques required for laser frequency stabilization of these two lasers.

3.1 Spectroscopy and Laser Frequency Stabilization to the $5s\ 5p\ ^3P_2 \rightarrow 5s\ 6s\ ^3S_1$ Transition

3.1.1 Doppler-Free Saturation Spectroscopy

Absorption of light in a medium

Consider a flux of photons incident on a medium as shown in Fig. 3.1. We are interested in the number of photons lost in the medium, $N_2 - N_1$. This photon loss can be caused by different processes. Some photons will be absorbed and re-emitted in random directions by the atoms that form the medium (being lost from the laser light). In general the number of photons lost will depend on the medium. However, if we assume that the probability of absorbing a photon per unit of length α is constant, then we can estimate the average number of photons absorbed in the Δz to be¹:

$$\Delta N = -\alpha N \Delta z. \quad (3.1)$$

Here we assume that the total number of photons absorbed per unit of length, Δz , is proportional to the total number of photons N in Δz . As we will show later, this is only true for low intensities because the scattering rate is a nonlinear function of the light intensity. The light intensity I is proportional to the total photon number, $I \propto N$, and

¹The absorption of light in a medium is a probabilistic process, therefore only average values for absorption of photons can be calculated. For simplicity in the notation we have omitted the angle brackets denoting the average symbol. ΔI and ΔN must always be understood as $\langle \Delta I \rangle$ and $\langle \Delta N \rangle$.

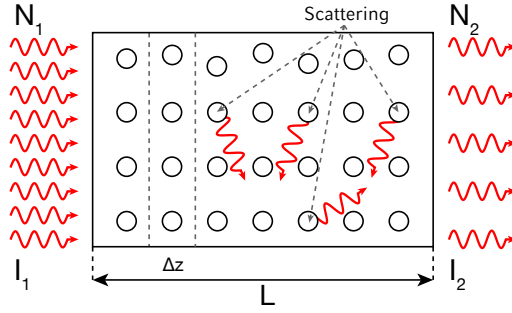


Figure 3.1: A flux of photons incident on a medium. Due to scattering with atoms some of the photons will be lost.

therefore Eq. (3.1) becomes:

$$\frac{\Delta I}{\Delta z} = -\alpha I. \quad (3.2)$$

For small absorption probability in the length interval Δz Eq. (3.2) becomes

$$\frac{\Delta I}{\Delta z} \approx \frac{dI}{dz} = -\alpha I. \quad (3.3)$$

Equation (3.3) can be solved to obtain the transmission coefficient of light through the medium:

$$T \equiv \frac{I}{I_0} = e^{-\alpha L} \equiv e^{-n \sigma L}, \quad (3.4)$$

where L is the length of the medium, n is the density of the medium and σ is the scattering cross section. Equation (3.4) is known as Lambert–Beer law for the attenuation of light in a medium. It predicts that the transmission of light intensity through the medium is independent of the input intensity. This is only true for low intensities. To show this we need to consider the time it takes a photon to travel through Δz :

$$t_l = \frac{\Delta z}{c}, \quad (3.5)$$

where c is the speed of light. If the photon flux is constant through the material then the probability for a photon to be scattered by an atom located within Δz is

$$P_a \approx t \Gamma_{sc} = \frac{\Delta z}{c} \Gamma_{sc}, \quad (3.6)$$

where Γ_{sc} is the scattering rate.

If N atoms (N_{atm}) are present in the sample then ΔN becomes

$$\Delta N = N_{atm} P_a = \frac{N_{atm}}{V} V P_a = \frac{\Delta z}{c} \Gamma_{sc} n V, \quad (3.7)$$

3.1 Spectroscopy and Laser Frequency Stabilization to the $5s\ 5p\ ^3P_2 \rightarrow 5s\ 6s\ ^3S_1$

Transition

19

where n is the density of atoms and V is the volume of the sample exposed to the beam.

Multiplying the left and right hand side of Eq. (3.7) by $\hbar \omega_l/V$ (\hbar is the reduced Planck constant and ω_l is the angular frequency of the radiation) yields:

$$\hbar \omega \Delta N/V = \frac{\Delta z}{c} \Gamma_{sc} n \hbar \omega, \quad (3.8)$$

The flux of light energy through a medium per unit of area and time, or light intensity, is:

$$I = n_p \hbar \omega_l c = \frac{N}{V} \hbar \omega_l c, \quad (3.9)$$

where n_p is the density of photons in the medium. The change of light intensity follows the equation:

$$\Delta I = \frac{\Delta N}{V} \hbar \omega_l c \quad (3.10)$$

Using equations (3.10) and (3.8) we obtain:

$$\Delta I = n \Gamma_{sc} \hbar \omega_l \Delta z, \quad (3.11)$$

and for small length changes:

$$\frac{dI}{dz} = n \Gamma_{sc} \hbar \omega_l \quad (3.12)$$

In chapter 2, Eq. (2.18) we showed that the probability of absorbing a photon per unit of time proportional to:

$$\Gamma_{sc} = \Gamma \frac{s_0/2}{1 + s_0 + 4 \frac{\Delta^2}{\Gamma^2}}. \quad (3.13)$$

which for low intensities becomes:

$$\Gamma_{sc} \approx \Gamma \frac{s_0/2}{1 + 4 \frac{\Delta^2}{\Gamma^2}} \equiv \frac{\Gamma}{2} \frac{I/I_{sat}}{1 + 4 \frac{\Delta^2}{\Gamma^2}} \quad (3.14)$$

If we use Eq. (3.14) in Eq. (3.12) we arrive at Eq. (3.3) with the following probability for absorbing a photon per unit of length:

$$P = \frac{\Gamma}{2} \frac{1/I_{sat}}{1 + 4 \frac{\Delta^2}{\Gamma^2}} n \hbar \omega_l \quad (3.15)$$

Using Eq. (3.14), Eq. (3.11) can also be formulated as:

$$\Delta I = -n \sigma I \Delta z, \quad (3.16)$$

And σ now becomes :

$$\sigma = \frac{3 \lambda^2}{2 \pi} \frac{1}{1 + 4 \Delta^2/\Gamma^2} = \frac{3 \lambda^2}{2 \pi}, \quad (3.17)$$

where the last step is only valid if $\Delta = 0$ and we have used the saturation intensity given in Eq. (2.17)².

For low intensities, $s_0 \ll 1$, the total absorption of light in the medium becomes:

$$\Delta I = \int_0^L n \frac{3 \lambda^2}{2 \pi} \frac{1}{1 + 4\Delta^2/\Gamma^2} I dz. \quad (3.18)$$

Equation (3.18) cannot be integrated directly as the light intensity depends implicitly on z . If the absorption of light intensity per unit of length can be considered to be small, for a low density medium or for off-resonant light ($|\Delta| \gg \Gamma$) for example, the light intensity can be considered to be independent of z . Under this approximation Eq. (3.18) can be integrated to obtain the total absorption of light in a medium, u :

$$u \equiv \frac{\Delta I}{I_0} \approx n \frac{3 \lambda^2}{2 \pi} \frac{1}{1 + 4\Delta^2/\Gamma^2} L, \quad (3.19)$$

where I_0 is the incoming light intensity. Additionally one could calculate the solution of Eq. (3.19) to obtain:

$$\begin{aligned} T \equiv 1 - u &\equiv \frac{I}{I_0} = \exp\left(-n \frac{3 \lambda^2}{2 \pi} \frac{1}{1 + 4\Delta^2/\Gamma^2} L\right) \\ &\approx 1 - n \frac{3 \lambda^2}{2 \pi} \frac{1}{1 + 4\Delta^2/\Gamma^2} L. \end{aligned} \quad (3.20)$$

Using Eq. (3.20) the absorption u becomes

$$u \equiv \frac{\Delta I}{I_0} \approx n \frac{3 \lambda^2}{2 \pi} \frac{1}{1 + 4\Delta^2/\Gamma^2} L, \quad (3.21)$$

the same result obtained in Eq. (3.19).

Given Eq. (3.19) one would expect the absorption spectrum of a cloud of atoms to have a width on the order of the natural atomic linewidth, Γ . However, for a cloud of strontium atoms at 550 °C the authors of Ref. [9] measure the full width half maximum (FWHM) of the absorption signal to be 940 MHz, while the natural linewidth of the transition, in this case $5s \ 5p \ ^3P_2 \rightarrow 5s \ 6s \ ^3S_1$, is 6.7 MHz, a factor more than 100 times wider. This effect is related to the thermal distribution of the atoms. As we showed in chapter 2, [Eq. 2.22] due to the Doppler effect, the scattering rate becomes shifted:

$$\Gamma_{sc}(\Delta - \vec{k} \cdot \vec{v}) = \Gamma_{sc} \frac{s_0/2}{1 + s_0 + 4 \frac{(\Delta - \vec{k} \cdot \vec{v})^2}{\Gamma^2}}, \quad (3.22)$$

²A full quantum mechanical calculation can be found in Ref. [22]. The quantum-mechanical approach shows that Eq. (3.17) presents an extra factor of ω_{eg}/ω_l .

The absorption of light intensity in a medium as given by Eq. (3.12), also becomes shifted:

$$\Delta I = - \int_0^l n \Gamma_{sc} (\Delta - \vec{k} \cdot \vec{v}) \hbar \omega_l dz, \quad (3.23)$$

Following the same approach as in Eq. (3.19) for small changes in light intensity, Eq. (3.23) becomes:

$$u(\Delta - \vec{k} \cdot \vec{v}) \equiv \frac{\Delta I}{I_0} \approx n \frac{3 \lambda^2}{2 \pi} \frac{1}{1 + 4(\Delta - \vec{k} \cdot \vec{v})^2 / \Gamma^2} L, \quad (3.24)$$

Averaging u over all velocities one obtains the expected total absorption profile in the medium:

$$\langle u(\Delta) \rangle = \int_{\mathbb{R}^3} f(\vec{v}) \frac{3 \lambda^2}{2 \pi} \frac{1}{1 + 4(\Delta - \vec{k} \cdot \vec{v})^2 / \Gamma^2} L d^3v, \quad (3.25)$$

where $f(\vec{v})$ is the velocity distribution in the atom cloud. For a non-interacting gas $f(\vec{v})$ factorizes to $f(\vec{v}) = f(v_x) f(v_y) f(v_z)$ [23] where $f(v_i)$ is:

$$f(v_i) = \sqrt{\frac{m}{2 \pi k_B T}} \cdot \exp\left(\frac{-m v_i^2}{2 k_B T}\right), \quad (3.26)$$

and m is the mass of the particles that form the gas, k_B is the Boltzmann constant, T is the temperature of the gas and v_i is the velocity in the i direction (x, y or z). Assuming that the light propagates along the z direction, $\vec{k} \cdot \vec{v}$ becomes $k v_z$ and Eq. (3.25) becomes:

$$\begin{aligned} \langle u(\Delta) \rangle &= \int_{\mathbb{R}^3} f(\vec{v}) u(\vec{v}) d^3v \\ &= \frac{\hbar \omega_l n L}{I_{sat}} \left(\int_{-\infty}^{\infty} f(v_x) dv_x \right) \left(\int_{-\infty}^{\infty} f(v_y) dv_y \right) G(\Delta) \\ &= \frac{\hbar \omega_l n L}{I_{sat}} G(\Delta), \end{aligned} \quad (3.27)$$

where we have taken into account that the velocity distributions in each direction are normalized to one and $G(\Delta)$, known as a Voigt profile, is the convolution of a Gaussian distribution with a Lorentzian distribution³:

$$G(\Delta) = \int_{-\infty}^{\infty} f(v_z) \cdot \frac{\Gamma/2}{1 + 4 \frac{(\Delta - k \cdot v_z)^2}{\Gamma^2}} dv_z \quad (3.28)$$

The Voigt profile is a line profile resulting from two broadening mechanisms, the Doppler shift, given by the Gaussian function, and the natural linewidth of the atom given by the Lorentzian distribution. The FWHM of this profile, is usually much larger than the atomic linewidth, and it is given by the thermal distribution of the atoms in the cloud.

³A more general derivation of the Voigt profile can be found in Ref. [12].

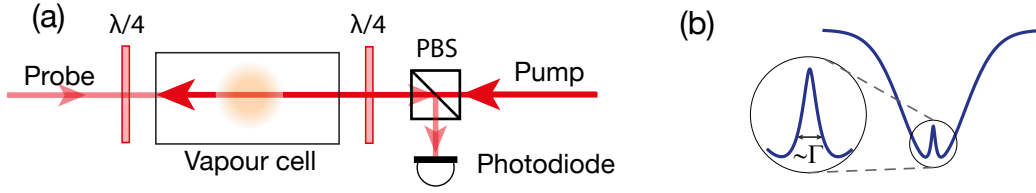


Figure 3.2: (a) Simplified setup of Doppler-free saturation spectroscopy. Two counter propagating beams will only address the same atoms when they are at rest ($v = 0$). The pump beam saturates these atoms and the probe beam shows a dip in the absorption profile due to a reduction of the ground state population. To separate both beams and detect the absorption profile two $\lambda/4$ waveplates and a polarizing beam splitter (PBS) can be used (b) Sketch of the Doppler-free saturated absorption profile. This absorption profile shows a Lamb dip, a reduction of the beam absorption due to depletion of ground state population. The width of this dip is on the order of the linewidth of the atomic transition (Γ).

Doppler-free saturation spectroscopy

To obtain a narrower profile, one of the most widely used techniques is known as Doppler-free saturation spectroscopy. Figure 3.2 (a) shows the basic schematic for Doppler-free saturation spectroscopy. Two counter-propagating beams, usually derived from the same laser address the atoms. As can be seen in Eq. (3.22), the two beams will address atoms with different velocities, v and $-v$, respectively (note the scalar product in Eq. (3.22), $\vec{k} \cdot \vec{v}$). Only when $v = 0$ (when $\Delta=0$) will both beams address the same atoms.

In the normal experimental scheme one beam will have high intensity (pump) and the other low intensity (probe). The pump beam depletes the ground state population and, as sketched in Fig. 3.2 (b), the absorption profile of the probe beam shows a dip known as the Lamb dip. The Lamb dip is a reduction of probe light due to the depletion of atoms in the ground state⁴. The width of this dip is now on the same order of magnitude as the linewidth of the transition.

To obtain a signal that can be used for laser frequency stabilization, the raw data of the signal sketched in Fig. 3.2 (b) cannot be used and different methods are used to modify it to obtain a signal which can be used for laser locking.

Modulating the beam frequency, for example, will create on the detector an oscillating signal which will be proportional to the derivative of the graph shown in Fig. 3.2 (b). To understand this, for small modulation depth m , the signal can be expanded in a Taylor series as:

$$I(\omega) = I[\omega_c + m \cos(\Omega t)] \approx I(\omega_c) + \frac{dI}{d\omega}(\omega_c) m \cos(\Omega t) + \mathcal{O}(m^2), \quad (3.29)$$

where $\omega = \omega_c + m \cos(\Omega t)$ is the instantaneous frequency of the laser and Ω is the

⁴This effect is more complex than this simple picture. For a more accurate explanation see Ref. [24].

modulation frequency. Equation (3.29) shows an oscillating signal at frequency Ω which is proportional to the derivative of the signal presented in Fig. 3.2 (b).

To transform this oscillating signal into a DC signal, a mixer can be used. In a simplified manner, a mixer can be understood as a 3 terminal device, which takes the input of two ports, and gives an output proportional to the product of them. A mixer can be used to multiply the modulated signal of Eq. (3.29) by another oscillating signal at the same frequency to obtain⁵:

$$\begin{aligned} I(\omega) \cos(\Omega t + \phi) &\approx [I(\omega_c) + \frac{dI}{d\omega}(\omega_c) m \cos(\Omega t)] \cos(\Omega t + \phi) \\ &= I(\omega_c) \cos(\Omega t + \phi) + \frac{dI}{d\omega}(\omega_c) \frac{m}{2} [\cos(2\Omega t + \phi) + \cos(\phi)], \end{aligned} \quad (3.30)$$

where ϕ is the phase difference between the two signals being multiplied and we have used the trigonometric identity:

$$\cos(\alpha) \cos(\beta) = \frac{1}{2} (\cos(\alpha + \beta) + \cos(\alpha - \beta)). \quad (3.31)$$

Using a low pass filter with a cutoff frequency much smaller than the modulation frequency the oscillating signals will be attenuated and the signal of Eq. (3.30) will become:

$$\frac{dI}{d\omega}(\omega_c) m \cdot \cos(\phi). \quad (3.32)$$

By slowly scanning the center frequency of the laser, ω_c , we will obtain in the output of the mixer the signal sketched in Fig. 3.3 (a), the derivative of the graph shown Fig. 3.2 (b). This technique is known as frequency modulation spectroscopy. For a more advanced and accurate explanation of the technique see Ref. [26].

This idea is much more flexible however, as it can be used to isolate, removing the unmodulated background, any type of feature that can be modulated. Modulating the pump frequency in Fig. 3.2 (b) will also produce an oscillating signal in the probe beam that after demodulation will produce Fig. 3.4 (a). This technique is known as modulation transfer spectroscopy. See Ref. [27] for more information on this technique as well as a practical example.

If we chop the pump on and off, we will obtain, after demodulation, Fig. 3.4 (b), where the symmetry of the figure depends on the phase of the modulation at each frequency. If we chop the pump on and off, all the points in the Lamb dip of Fig. 3.2 (b) will move in phase, while if we modulate the frequency of the pump beam, we effectively move the Lamb dip left and right. In this last case, the modulation of two points

⁵This idealized process is indeed more complex, a mixer will not only attenuate the output signal but will also distort it producing higher order harmonics [25].



Figure 3.3: (a) Schematic of the signal obtained after demodulation of the absorption signal with the pump unblocked. A Doppler-free feature appears in the center of the signal. (b) Schematic of the signal obtained after demodulation with the pump blocked. Since there is no pump, the Lamb dip shown in Fig. 3.2 (b) is no longer present and no Doppler-free feature can be seen.

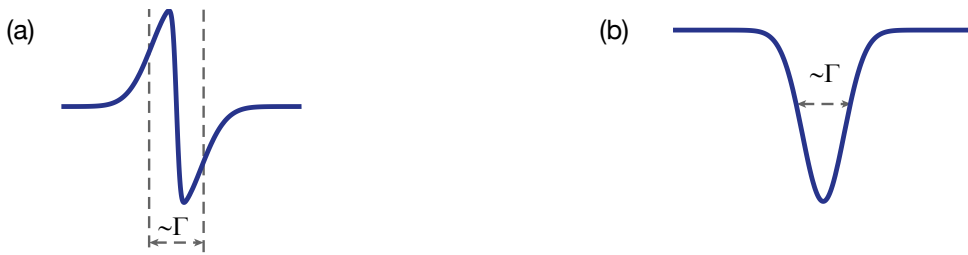


Figure 3.4: (a) Output of the mixer after modulation of the pump beam. (b) Output of the mixer after chopping the pump beam

located at each side of the Lamb dip will now be dephased by π , and the output of the mixer will be antisymmetric (note that the output of the mixer is proportional to $\cos(\phi)$ and $\cos(\phi) = -\cos(\phi + \pi)$ therefore a sign change when the frequency of the laser is situated at the position of the Lamb dip will be present).

Chopping the pump on and off can also allow us to switch between Fig. 3.3 (a) and Fig. 3.3 (b), thus modulating the Doppler-free feature and, after demodulation, obtaining a signal similar to the one shown in Fig. 3.3 (a) (this can be useful to compensate for fluctuations in the laser intensity for example). This last idea will be applied in the next section to obtain a clear and well defined error signal.

3.1.2 Experimental Setup

An overview of the optical setup used to generate the error signal to stabilize the frequency of the 707 nm laser is given in Fig. 3.5. A similar setup was reported by the authors of Ref. [9].

Thermal excitation of the strontium triplet states is not possible as the temperature required is too high:

$$T \approx \frac{E_o}{k_B} \approx 21,000 \text{ K}, \quad (3.33)$$

where E_o is the energy of the $5s\ 5p\ ^3P_0$ state and T is the required temperature to popu-

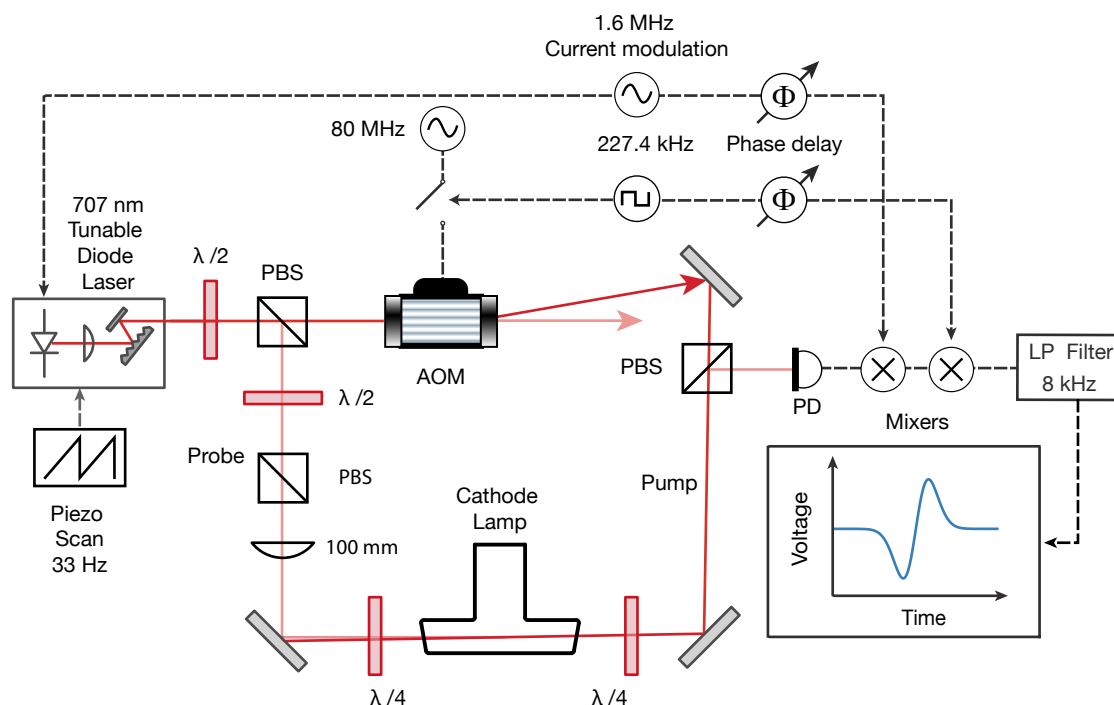


Figure 3.5: Schematic of the experimental setup used to obtain the error signal.

late the $5s\ 5p\ ^3P_0$ state thermally. For this reason we use a see-through hollow cathode lamp (Hamamatsu L2783-38NE-SR) to generate the cloud of strontium atoms. The lamp is operated with a high voltage power supply (SRS-PS310) at 18 mA and 900 V DC. The energies involved in the lamp discharge are much higher than the relevant optical energies and therefore population of the excited states can be expected:

$$E_e \approx 300\text{ eV} = 160 E_o\text{ eV}. \quad (3.34)$$

Here E_e is the energy that a single free electron would gain travelling from one electrode of the lamp to the other⁶.

To address the atoms we use a grating stabilized diode laser from Toptica. The laser output is divided by a polarizing beam splitter and a $\lambda/2$ waveplate to generate probe and pump beams. The pump beam passes through a 80 MHz acousto-optic modulator (AOM) from Gooch & Housego (3080-120). The first diffracted order then passes through the cathode lamp to saturate the atoms.

To match the waist of the probe beam to the size of the atom cloud a plano convex lens from Thorlabs (AC254 $f=100$ mm) focuses the light to the center of the lamp. At

⁶In steady state the voltage drop in the lamp is 300 V, the rest of the power is dissipated in an external resistor used in series with the lamp.

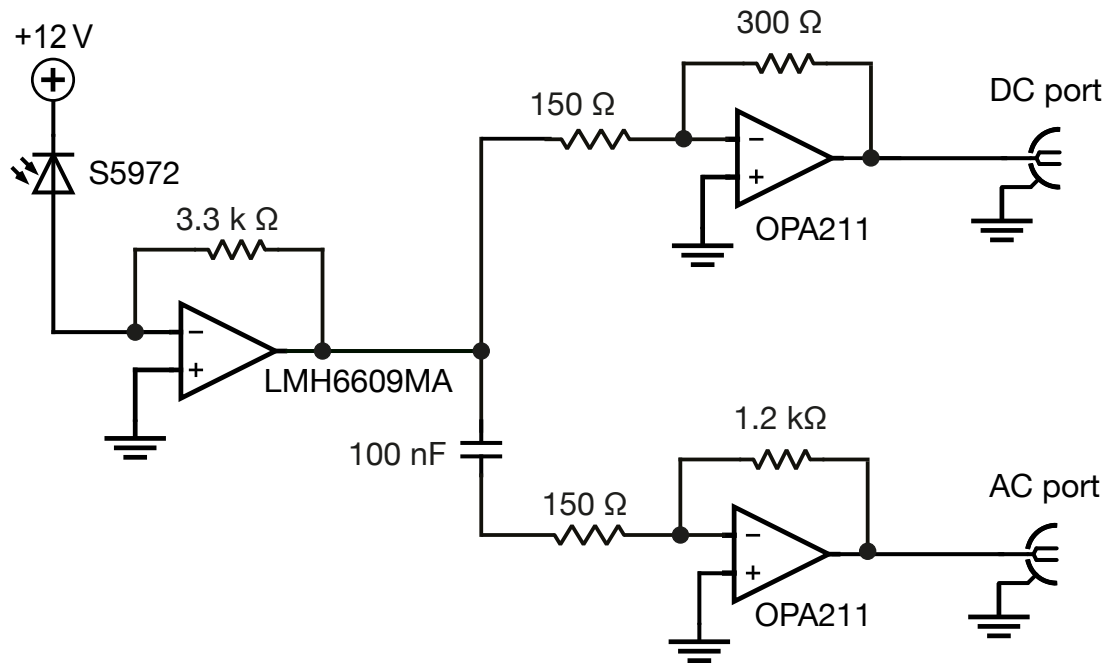


Figure 3.6: Simplified photodiode diagram. A Hamamatsu S5972 photodiode is coupled to a 3.3 k Ω transimpedance amplifier. The output of the amplifier is divided into an AC and a DC port.

this point, the waist of the probe beam is 225 μm , while the waist of the pump beam is 800 μm . The power of the pump beam is 4.7 mW and the power of the probe beam is 140 μW .

The polarization of both pump and probe beams is modified by two $\lambda/4$ waveplates on both sides of the lamp to make the polarization of both beams circular at the atoms.

Figure 3.6 shows the sensing circuit used to detect the probe transmission (see Ref. [18] for a discussion of the design criteria, noise limitation and bandwidth of the circuit). A Hamamatsu S5972 photodiode is coupled to a LMH6609 3.3 k Ω transimpedance amplifier. The output of the transimpedance amplifier is then divided into an AC port and a DC port. Modulation is detected on the output of the AC port while the DC port is used for monitoring purposes. The total bandwidth of the circuit (≈ 15 MHz) is much higher than the modulation bandwidth (≈ 1.6 MHz) while the DC offset in both ports was ≈ 0.300 mV. The response of the photodiode to the laser power is 2.3 V/mW (measured using a 707 nm beam in the DC port). The output of the AC port is amplified using two Minicircuits amplifiers (ZFL-1000 LN+).

3.1.3 Results

Figure 3.7 (a) shows the absorption signal measured at the photodiode when the pump is blocked (black) and unblocked (red) as the laser wavelength is slowly swept across the atomic resonance. With no pump present, approximately 1.5 % of the total optical power

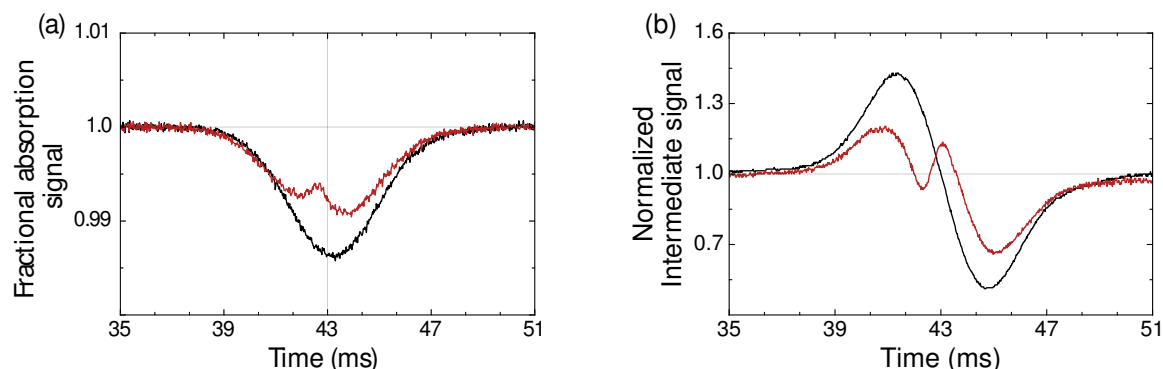


Figure 3.7: (a) Absorption signal with pump on (red trace) and off (black trace) With no pump present, approximately 1.5 % the optical power is absorbed, when the pump is on, the absorption is reduced. (b) Intermediate signal after first demodulation at 1.6 MHz with pump on (red) and off (black). Both signals have been normalized to the background intensity to compensate for intensity variations due to the laser scan. For display purposes, the data was averaged a total of 8 times.

is absorbed. With the pump unblocked, a Doppler-free peak of height $\approx 0.8\%$ appears (referenced to the bottom of the unsaturated spectrum). Due to the AOM frequency shift in the pump beam there is an offset between both peaks.

To obtain a clear error signal we first perform frequency modulation spectroscopy by modulating the current of the laser at 1.628 MHz frequency and 5 mA (peak-to-peak amplitude). A Minicircuits ZRPD-1+ phase detector is used to demodulate the signal. Figure 3.7 (b) shows the output of the mixer with the pump blocked (black) and unblocked (red)⁷. For clearness the signals have been normalized to compensate for intensity fluctuations due to the piezo scan of the laser (see section 3.1.4 for the raw data). An extra DC offset was also present due to intensity fluctuations caused by the current modulation. The intensity changes due to the current modulation have sinusoidal shape and add an extra component oscillating at the same frequency in Eq. (3.29) resulting in a total DC offset in the signal after demodulation.

To compensate for changes in the laser intensity, to suppress the DC offset, and to obtain a well-defined error signal, the AOM chops the pump on and off at a frequency of 227.4 kHz. After a second demodulation step using a Minicircuits ZLW-3+ mixer and the same low pass filter previously described the error signal is obtained. Figure 3.8 (a) shows the final error signal used for locking the laser. Intensity fluctuations are completely suppressed. However, due to mixer imbalance, a small residual DC offset of 1 mV remains⁸.

Using a High Finesse WS7 wavemeter, we estimate the error in the locking frequency

⁷The output is low pass filtered using a single pole RC low pass filter circuit with a $50\ \Omega$ and a ceramic capacitor of capacitance $1\ \mu\text{F}$.

⁸We estimated the total DC offset due to the mixer using the isolation value between the two ports in the manner described by the authors of Ref. [25].

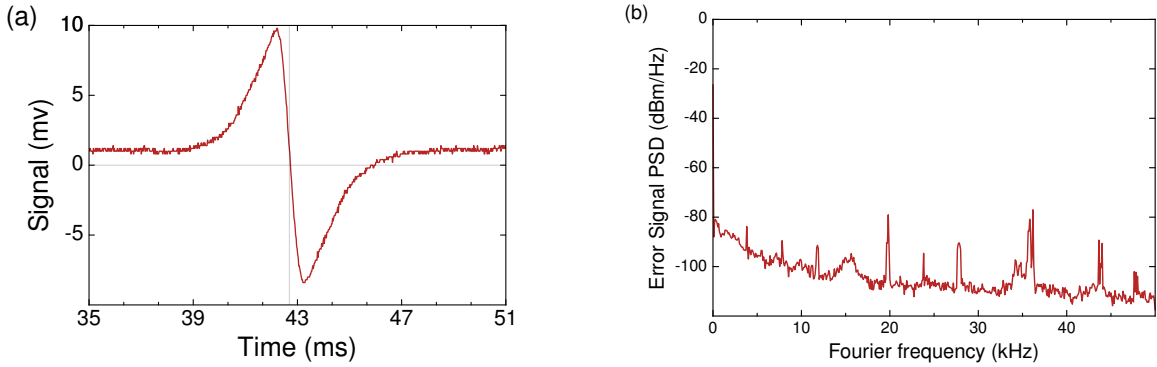


Figure 3.8: (a) Final error signal used to lock the laser. For display purposes, the data was averaged a total of 8 times. Without averaging, the signal to RMS noise ratio was ≈ 40 . (b) Power spectral density (PSD) of the error signal in open loop configuration. Intermodulation between the different mixing stages causes different peaks to appear. The modulation and chopping frequencies were chosen to suppress these features. The output was AC-coupled at 9 kHz

to be:

$$\frac{\Delta\omega}{\Gamma} = \frac{d\omega}{dV} \frac{1}{\Gamma} \Delta V \approx 0.4, \quad (3.35)$$

where $\Delta\omega$ is the error in the locking frequency, Γ is the linewidth of the $5s\ 5p\ ^3P_2 \rightarrow 5s\ 6s\ ^3S_1$ transition (this value was measured in Ref. [21] to be 6.7 MHz) and ΔV is the DC offset of the error signal. We estimated $\frac{d\omega}{dV}$ to be $\approx \frac{\Delta\omega}{\Delta V}$ where ΔV is the peak-to-peak voltage of the error signal and $\Delta\omega$ is the frequency separation of both peaks.

Without averaging the signal-to-noise ratio in Fig. 3.8 (a) was 40. Equation (3.35) can also be used to estimate the root mean squared (RMS) frequency noise imposed on the laser to be $\approx 0.2\ \Gamma$. It is important to understand that in Fig. 3.8 (a) there are two sources of noise, the noise of the error signal, which will be imposed on the laser, created by the photodiode, mixing stages and other electronic devices and the laser frequency fluctuations. Therefore the value given can only be taken as a very rough estimation of the frequency noise imposed on the laser.

As will be explained in section 3.1.4, these estimates must be taken with care, as the measurement error of the wavemeter is on the order of the linewidth of the transition. Both of these results however are consistent with the saturation parameters of the beams. Using the saturated linewidth of the probe beam as a measure of the frequency spread of both peaks [as given by Eq. (2.20) $\Gamma' = \Gamma \sqrt{1 + s_0} = 9\ \Gamma$], gives an error in the locking point of $\Delta\omega \approx 0.45\ \Gamma$. For the pump beam the saturated linewidth is $14\ \Gamma$. This width gives an error in the locking point of $\Delta\omega \approx 0.7\ \Gamma$.

Figure 3.8 (b) shows the error signal power spectral density in open loop configuration. Due to intermodulation between the current modulation and the pump chop, different peaks appear. Small changes in the current modulation frequency, or in the



Figure 3.9: Power spectral density of the error signal when the laser is locked (left) and when the laser is left free running (right)

chopping frequency, change the position and the height of these peaks. The values of the frequencies must be optimized so that the peak frequencies are well above the low pass filter cutoff frequency and the feedback bandwidth.

For frequency stabilization we use a double integrator feedback circuit for stabilization of the piezo of the laser, while at the same time, performing feedback in the current of the diode with a single proportional integral (PI) controller⁹. Fig. 3.9 shows the power spectral density of the error signal when the laser is in closed loop (left) or when it is left free running (right). A noise suppression of several dB for frequencies below 3 kHz can be seen. This locking bandwidth is similar to that reported by the authors of Ref. [9].

3.1.4 Data Analysis

Figure 3.10 shows the raw data of the absorption spectrum (red and black traces). A linear fit was performed to the background for normalization (blue dashed traces). Figure 3.7 (a) was obtained by taking the ratio of this signal by the fit. For the fit, the frequency scan was tuned to be approximately two times wider than the absorption signal. Data points were selected at both sides of the absorption signal where the light was not resonant. In all cases, the goodness of the fit, which we determine by the r -squared coefficient (R^2), was deemed to be good if $|1 - R^2| < 10^{-3}$. All the absorption data presented in this chapter was normalized using this procedure.

There is also an extra offset between the red and the black traces. This offset is produced by unwanted reflections of the pump beam from optical surfaces.

When the pump beam is modulated, the signal detected on the photodiode (S_d) due to these reflections shows an added time-dependent signal of the form:

$$S_d(t) = x_s(t) A_c \sin(\Omega_c t), \quad (3.36)$$

⁹See Ref. [28] for details on feedback control of physical systems.

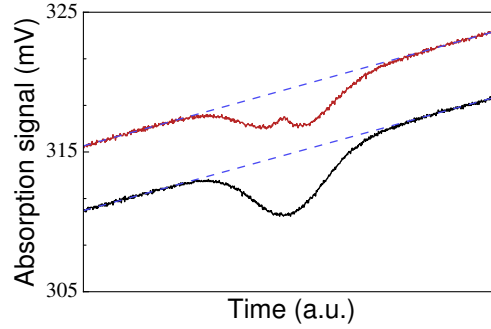


Figure 3.10: Raw data of the absorption signal with pump (red) and without pump (black). To normalize the background a linear fit was performed (blue dashed traces). The offset between the two traces is produced by reflections of the pump beam from different optical surfaces. Both traces were averaged a total of 8 times.

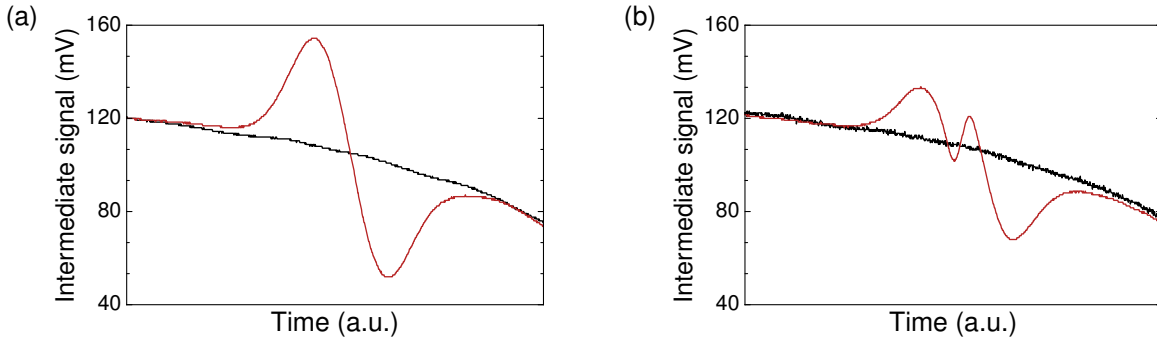


Figure 3.11: (a) Raw data of the intermediate absorption signal without pump (a) with pump (b). The black trace shows the background trace obtained by turning the lamp off.

where $x_s(t)$ is a square wave with amplitude of 5 mV and frequency of 227.4 kHz (the pump chop frequency), Ω_c is the frequency of the current modulation and A_c is the voltage amplitude in the photodiode created by the current modulation (see Fig. 3.5).

The offset of Fig. 3.10 S_d presents the same modulation as the signal we want to detect. After demodulating at Ω_c and at the chopping frequency, this signal will show up as a phase dependent offset independent of the laser frequency. This is undesirable as the offset will change the zero crossing of the error signal, and thus change the frequency of the locking point. The angle of the pump beam must be tuned to eliminate this effect. Using our experimental parameters given in section 3.1.2 we calculate that in the signal presented in Fig. 3.10 only a small fraction of $\approx 0.03\%$ of the pump beam power was collected by the photodiode.

For the signal presented in Fig. 3.7 (b) the background trace could not be fitted by a linear function. For this reason we measured the background signal for each graph and used it for normalization. The background trace of the signal shown in Fig. 3.7 (b) was measured by turning the lamp off and leaving the rest of the experimental components

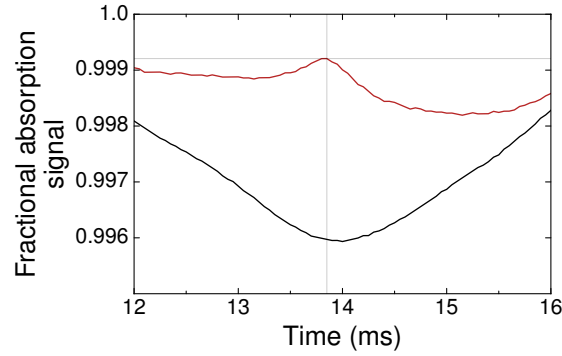


Figure 3.12: Fractional absorption signal with pump on (red trace) and off (black trace). With no pump present, approximately 0.4 % the optical power is absorbed. When the pump is on, the absorption is reduced. For display purposes, the signals have been averaged a total of 8 times.

unmodified. Fig. 3.11 (a) and Fig. 3.11 (b) show the intermediate signal with the pump blocked and unblocked (both red) and their correspondent background traces used for normalization in each case (black). The result of the normalization process can be seen in Fig. 3.7 (b). To reduce the error in the normalization a higher order polynomial fit could be used, however we found this not to be necessary.

To estimate the RMS frequency noise and locking error, calibration of the frequency was done using a High Finesse WS7 wavemeter. The relative precision of the wavemeter is $\Delta\omega \approx 2\pi \times 10$ MHz which is on the order of the $5s\ 5p\ ^3P_2 \rightarrow 5s\ 6s\ ^3S_1$ transition linewidth. This calibration method severely limits the precision. For better results a Fabry-Perot cavity or a Michelson interferometer could be used. To better understand the physics and to test the precision of the calibration, all results can be compared to the expected linewidth given the saturation parameters of each of the beams.

3.2 Spectroscopy and Laser Frequency Stabilization to the $5s\ 5p\ ^3P_0 \rightarrow 5s\ 6s\ ^3S_1$ Transition.

3.2.1 Frequency Modulation Spectroscopy Measurements

Stabilization to the $5s\ 5p\ ^3P_0 \rightarrow 5s\ 6s\ ^3S_1$ proves more challenging. Using the data from Ref. [21] we calculated the ratio between the different Einstein coefficients:

$$\frac{A(5s\ 5p\ ^3P_2 \rightarrow 5s\ 6s\ ^3S_1)}{A(5s\ 5p\ ^3P_0 \rightarrow 5s\ 6s\ ^3S_1)} \approx 4.7, \quad (3.37)$$

which shows that a much smaller signal-to-noise ratio is to be expected.

Figure 3.12 shows the fractional absorption signal when scanning the laser through

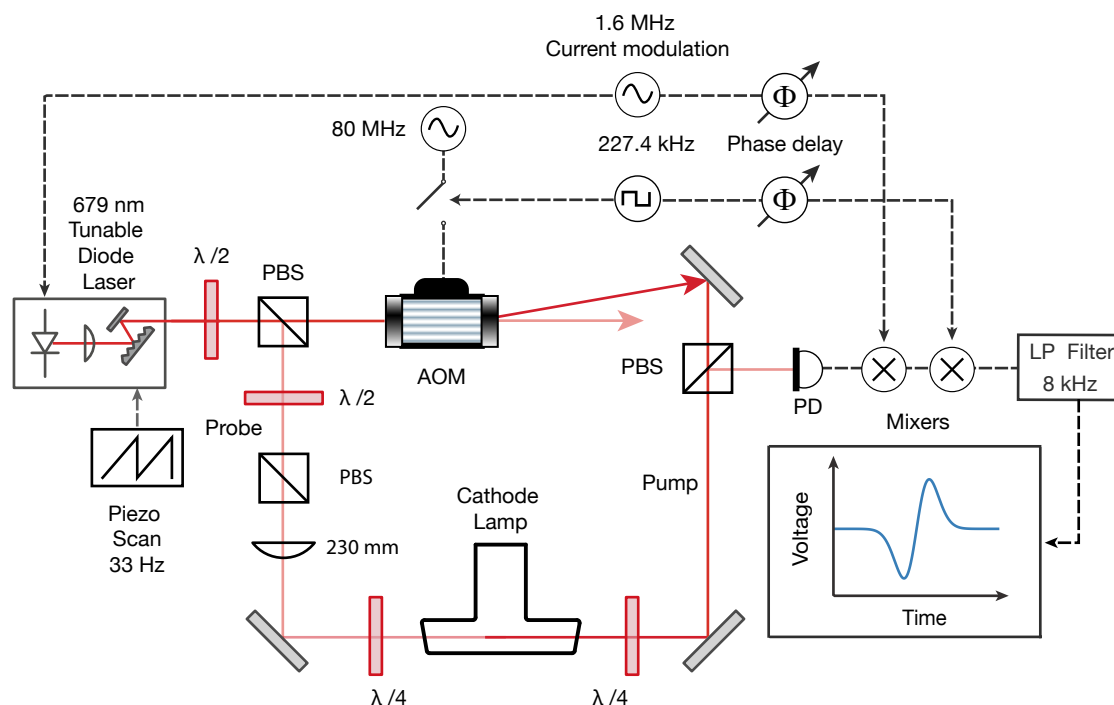


Figure 3.13: Schematic of the experimental setup.

the atomic resonance¹⁰. The factor of 4.7 is larger than the ratio between the signals presented in 3.14 (a) and Fig. 3.12. However, for an accurate calculation of this factor Eq. (3.28) with the proper experimental parameters must be used.

Using the same setup described in section 3.1.2 we obtained the error signal shown in Fig. 3.14 (b). The experimental parameters in this case can be seen in Fig. 3.13. We used a grating stabilized diode Laser from Toptica tuned to 679 nm wavelength. The output of the laser was divided into probe and pump beams. A plano convex lens from Thorlabs (LA1461-B 250 mm) focuses the probe beam at the center of the lamp. At this point, the beam powers are $450 \mu\text{W}$ for the probe and 4.5 mW for the pump. The beam waists are $390 \mu\text{m}$ and $800 \mu\text{m}$ respectively.

In a similar fashion as in section 3.1.2 the laser current was modulated with 1.6 MHz frequency and 5 mA (peak-to-peak amplitude) and the pump was chopped at a frequency of 130 kHz. Figure 3.14 (a) shows the output of the first demodulation stage with pump blocked (black), and unblocked (red). The output of the second demodulation stage at this frequency can be seen in Fig. 3.14 (b)¹¹. Again a DC offset of 1.3 mV

¹⁰The normalization procedure used for all the absorption and intermediate signals shown in this section is described in section 3.1.4.

¹¹The output of both mixers was filtered with a single pole RC low pass filter of with a 50Ω resistors and a capacitance of $1 \mu\text{F}$.

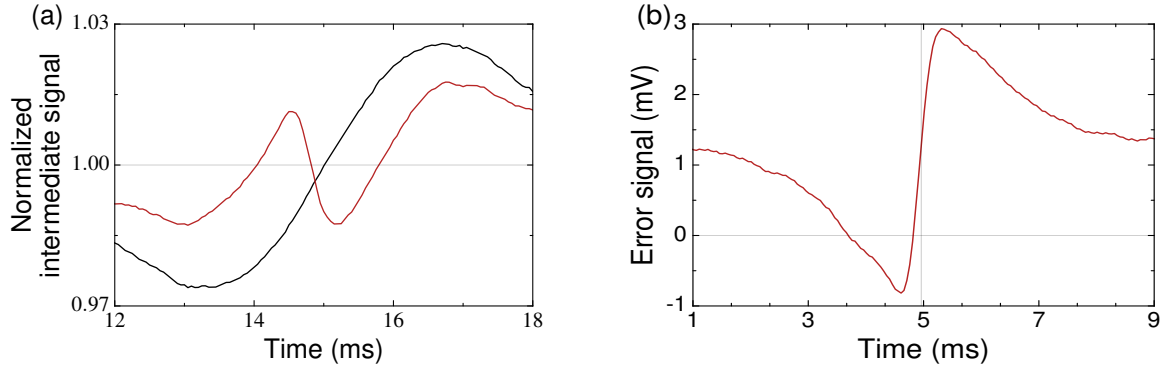


Figure 3.14: (a) 679 nm signal after first demodulation at 1.6 MHz with pump unblocked (red) and blocked (black). (b) Error signal after second demodulation at 130 kHz. The signal has a total offset of 1.3 mV. Without averaging figure (b) presented a signal-to-noise ratio to of 3 (both traces have been averaged a total of 8 times).

is present, which can also be explained by mixer imbalance. The rest of the experimental parameters of the devices shown in Fig. 3.13 remain unchanged and can be taken from Fig. 3.5. Two major problems are associated with the final error signal presented in figure 3.14 (b):

- Using Eq. (3.35) the error in the locking point can be estimated to be $\approx 4.7 \Gamma$, where Γ now is the linewidth of the $5s\ 5p\ ^3P_0 \rightarrow 5s\ 6s\ ^3S_1$ transition. Therefore offset compensation is necessary. An oscillation of 0.1 mV in the compensation voltage however, will change the locking frequency by $\approx 0.47 \Gamma$.
- The signal-to-noise ratio of was ≈ 3 . This voltage noise directly translates to frequency noise. Using Eq. (3.35) one can estimate the frequency fluctuations to be $\approx 1.5 \Gamma$.

These estimations were made with the wavemeter calibrations described in section 3.1.4. Taking into account our saturated linewidths as a measure of the frequency separation between the maxima we obtain compatible results with the wavemeter calibrations. The authors of Ref. [9] also report the signal-to-noise ratio of the $5s\ 5p\ ^3P_0 \rightarrow 5s\ 6s\ ^3S_1$ error signal to be a fundamental limitation to the locking procedure.

3.2.2 Overview of the Error Signal Generation

For the reasons expressed in the last section we developed a new procedure for frequency stabilization. In this section we will explain the physical principles of the frequency locking technique.

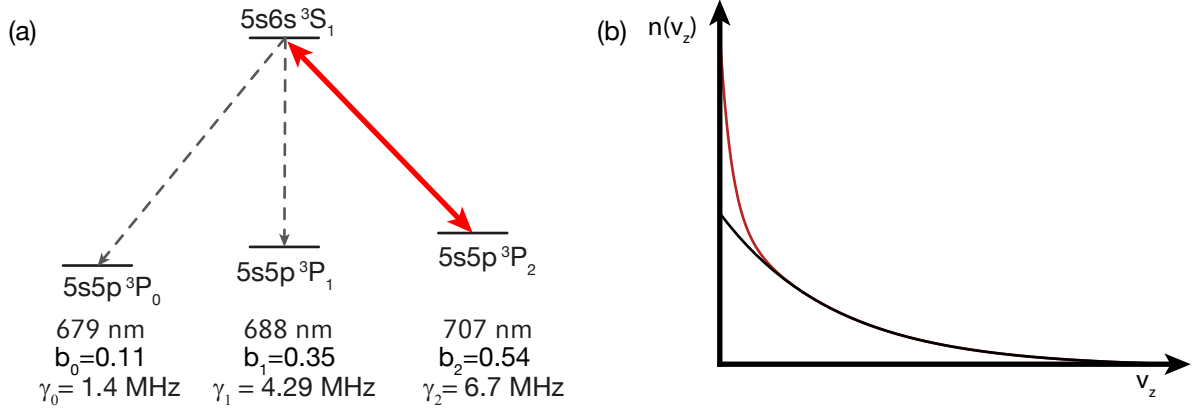


Figure 3.15: (a) Diagram of the transition between the triplet states and the $5s\ 6s\ ^3S_1$ state. The branching ratios are denoted below for each of the transitions as b_i . The data was taken from Ref. [21]. A 707 nm laser beam resonant with the $5s\ 5p\ ^3P_2 \rightarrow 5s\ 6s\ ^3S_1$ pumps atoms to the $5s\ 6s\ ^3S_1$ state (red solid line). From here atoms can spontaneously decay to the $5s\ 5p\ ^3P_2$ and $5s\ 5p\ ^3P_1$ states (grey dashed traces). (b) Drawing of the 1D thermal distribution for the atoms. In absence of pumping light the expected 1D velocity distribution of the atoms is just a Gaussian function (black trace). With the 707 nm light on, an increase of atoms at low velocities is seen (red).

The main idea is to use a 707 nm laser to increase the population in the $5s\ 5p\ ^3P_0$ state by optically pumping atoms from the $5s\ 5p\ ^3P_2$ state [29]. As we will show later the effect of a 707 laser resonant with the $5s\ 5p\ ^3P_2 \rightarrow 5s\ 6s\ ^3S_1$ transition can also be understood to partially close the $5s\ 5p\ ^3P_0 \rightarrow 5s\ 6s\ ^3S_1$ transition, see Fig. 3.15 (a). A locked laser resonant with the $5s\ 5p\ ^3P_2 \rightarrow 5s\ 6s\ ^3S_1$ transition will only address atoms with zero transverse velocity. As sketched in Fig. 3.15 (b), the laser will modify the thermal distribution of the gas, increasing the number of atoms with low velocities. As can be seen in the graph of Fig. 3.16 (a), the laser creates a feature in the absorption spectrum of 679 nm beam of several MHz width.

To better understand this process, a simple model of rate equations can be developed. For closed transitions, the populations in the steady state are only dependent on the detuning, the intensity of the laser as well as the thermal properties of the cloud. For open transitions, the situation is a bit more complex as atoms will be lost over time on a timescale determined by the scattering rate and the branching ratio. The population $\rho_{11}(t)$ of the $5s\ 5p\ ^3P_0$ state decays as:

$$\frac{d\rho_{11}(t)}{dt} \approx -\Gamma_s (1 - b)\rho_{11}(t), \quad (3.38)$$

where b is the branching ratio of the corresponding transition (see Fig. 3.15), $1 - b$ is the probability of losing an atom after each scattering event and Γ_s is the light scattering rate.

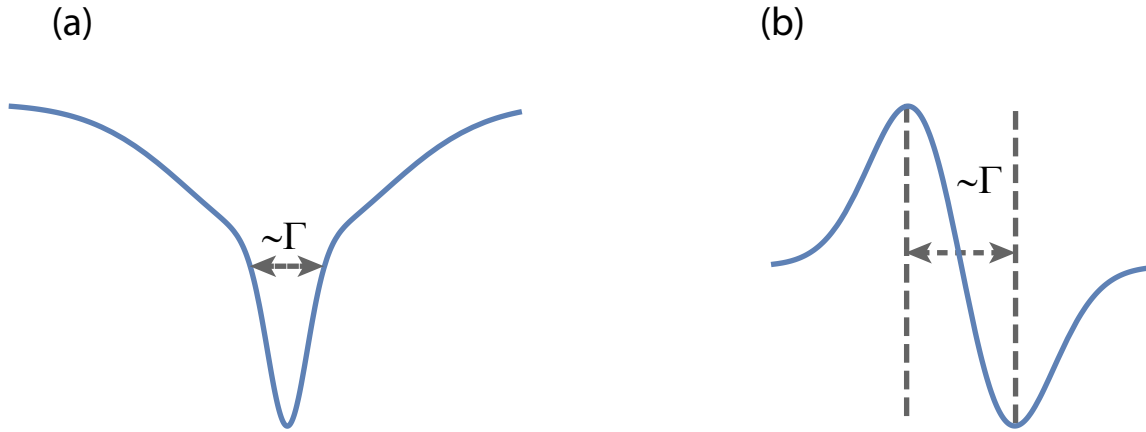


Figure 3.16: (a) Sketch of the expected absorption signal when probing the $5s\ 5p\ ^3P_0 \rightarrow 5s\ 6s\ ^3S_1$ transition with a 679 nm laser. The signal shows an increase in the absorption due to the pumping of the 707 nm laser. The width of the feature is on the order of the linewidth of the $5s\ 5p\ ^3P_2 \rightarrow 5s\ 6s\ ^3S_1$ transition. Modulating the 707 nm beam results in a modulation of this feature. The modulated feature can be isolated by demodulation, in the manner explained in section 3.1.1. (b) Sketch of the signal after demodulation. Here Γ is the linewidth of the $5s\ 5p\ ^3P_2 \rightarrow 5s\ 6s\ ^3S_1$ transition.

The population will not be zero because the discharge of the cathode lamp will add atoms to each of the levels at a rate independent of the population:

$$\frac{d\rho_{11}(t)}{dt} = \Gamma_l, \quad (3.39)$$

where Γ_l is defined to be the rate at which the medium adds atoms in each of the levels. Atoms will also be lost at a rate which we estimate to be proportional to the population:

$$\frac{d\rho_{11}(t)}{dt} = -\Gamma_c \rho_{11}(t). \quad (3.40)$$

Here Γ_c is defined to be the probability of losing an atom per unit of time.

Combining the last three equations one obtains:

$$\frac{d\rho_{11}(t)}{dt} = -(\Gamma_s (1 - b) + \Gamma_c) \rho_{11}(t) + \Gamma_l, \quad (3.41)$$

Before turning on the light the population rate has to be equal to the loss rate (assuming the lamp has reached the steady state). Therefore Eq. (3.39) and Eq. (3.40) are equal and it follows that:

$$\Gamma_c \rho_{11}(0) = \Gamma_l, \quad (3.42)$$

One can calculate the steady state solution¹²:

$$\rho_{11}(t)(\infty) = \frac{\Gamma_l}{\Gamma_s(1-b) + \Gamma_l}. \quad (3.43)$$

Here we have normalized the population at $t = 0$ to one:

$$\rho_{11}(0) = 1, \quad (3.44)$$

and we have used Eq. (3.42).

Using a 707 nm laser, one can partially close the $5s\ 5p\ ^3P_2 \rightarrow 5s\ 6s\ ^3S_1$ transition and decrease the probability of losing an atom per scattering event from 0.9 to 0.4.

Assuming $\Gamma_s \gg \Gamma_l$, Eq. (3.43) can now be used to estimate the increase in population as:

$$\frac{\rho_1}{\rho_2} = \frac{\Gamma_s 0.9 + \Gamma_l}{\Gamma_s 0.4 + \Gamma_l} \approx \frac{0.9}{0.4} = 2.25, \quad (3.45)$$

where ρ_1 and ρ_2 refer to the population of the $5s\ 5p\ ^3P_0$ state with and without 707 nm light respectively.

With a 707 nm laser resonant with the $5s\ 5p\ ^3P_2 \rightarrow 5s\ 6s\ ^3S_1$ transition we can expect to double the population in the $5s\ 5p\ ^3P_0$ state therefore doubling the absorption signal. A laser resonant with the $5s\ 5p\ ^3P_2 \rightarrow 5s\ 6s\ ^3S_1$ transition will only address atoms with $\vec{k} \cdot \vec{v} = 0$ velocity (see section 3.1.1). Therefore a feature with a width comparable to linewidth of the $5s\ 5p\ ^3P_2 \rightarrow 5s\ 6s\ ^3S_1$ transition is expected (see Fig. 3.16 (a)).

It is possible to use the setup described in section 3.1.2 with this increase in population to generate the error signal. If we assume that the signal to noise ratio of Fig. 3.14 (b) to be proportional to the total population of atoms in the ground state, then we obtain a signal-to-noise ratio of 6 (or frequency noise of 0.75 Γ). The expected error in the frequency lock will be $\approx 2.85\ \Gamma$, where Γ is the linewidth of the $5s\ 5p\ ^3P_0 \rightarrow 5s\ 6s\ ^3S_1$ transition. For these reasons we proceed with a different approach that will allow us to obtain better results.

The ideas explained in section 3.1.1 can also be used here. Modulating the 707 nm beam frequency can be done to isolate this feature and to obtain, after a single demodulation step, Fig. 3.16 (b)¹³.

To estimate the signal-to-noise ratio increase between both systems, we need to take into account that the peak-to-peak voltage of the signal shown in Fig. 3.14 (b) is proportional to the height of the Doppler-free feature presented in Fig. 3.14 (a). The signal

¹²To calculate this solution we approximate that in the steady state (when $t = \infty$) there is no population change $\frac{d\rho_{11}(t)}{dt}(\infty) \approx 0$.

¹³The points located at each side of the feature will now oscillate with a total phase of π . Therefore the final signal will be antisymmetric.

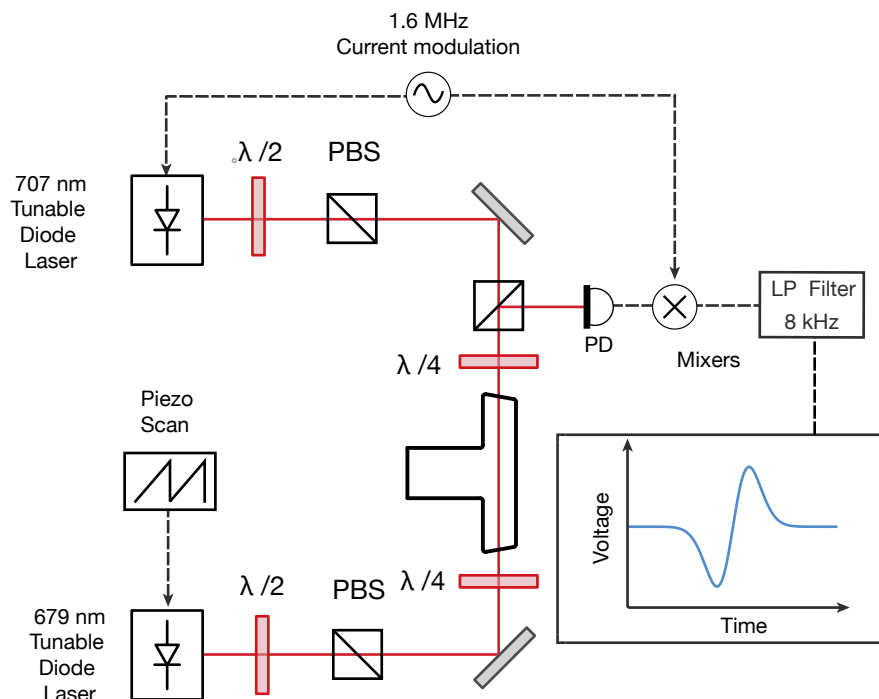


Figure 3.17: Experimental setup used to stabilize the 679 nm laser.

presented in Fig. 3.14 (a) is approximately the derivative of Fig. 3.12 (with an added offset). The derivative of this signal scales with the height of the Doppler-free peak referred to the minimum of the absorption signal. Therefore the signal-to-noise ratio of Fig. 3.14 (b) is proportional to the height of the Lamb dip.

Similarly the peak-to-peak voltage of the graph shown in Fig. 3.16 (b) will increase proportionally with the absorption increase.

In view of the previous considerations we can estimate the signal-to-noise increase between both signals to be equal to the ratio of the height of the Lamb dip seen in Fig. 3.12 to the total increase in absorption (using the unnormalized values) times three¹⁴. Using the data presented in Fig. 3.12 we estimated this to be a factor ≈ 11 .

3.2.3 Setup

Figure 3.17 shows an overview of the optical setup used to generate the error signal to stabilize the 679 nm laser. A 707 nm laser (pump) resonant with the $5s\ 5p\ ^3P_2 \rightarrow 5s\ 6s\ ^3S_1$ transition increases the $5s\ 5p\ ^3P_0$ state population at low velocities. The current of the laser is modulated at 1.6 MHz and 5 mA (peak-to-peak amplitude). To probe the

¹⁴This factor of three comes from the losses in the second mixing stage.

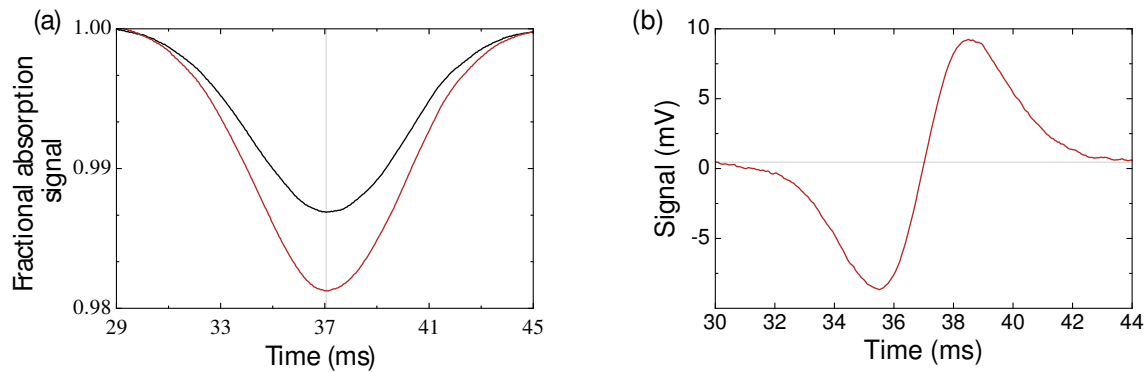


Figure 3.18: (a) Fractional absorption signal with the 707 laser blocked (black) and unblocked (red). An increase in the population of 41 % can be seen across all velocity classes. The beam parameters are 1 mm (0.8 mm) waist 0.4 mW (6.9 mW) for the 679 nm (707 nm) laser. (b) Final error signal after demodulation at 1.6 MHz. For display purposes both images have been averaged a total of 8 times.

$5s\ 5p\ ^3P_0 \rightarrow 5s\ 6s\ ^3S_1$ transition the 679 nm diode laser (probe) is scanned across the atomic resonance.

The rest of the parameters for the experimental devices shown in Fig. 3.17 remain unchanged in the setup and are described in section 3.1.2

3.2.4 Results

Figure 3.18 (a) shows the fractional absorption signal when the 707 nm laser is blocked (black trace) and unblocked (red trace). A maximum absorption increase of $\approx 50\%$ is seen. Figure 3.16 (a) shows a much broader profile than the profile sketched in Fig. 3.16 (b). This should be expected if the thermalization timescales are smaller than the linewidth of the $5s\ 5p\ ^3P_0 \rightarrow 5s\ 6s\ ^3S_1$ transition. The thermalization time scales inversely proportional to the density as:

$$t_{th} \propto \frac{1}{n \sigma_c \langle v \rangle},$$

where t_{th} is the thermalization time, n is the density of atoms, σ_c is the collisional cross section, and $\langle v \rangle$ is the average velocity of atoms in the gas.

Therefore we expect ground state atoms to act as a thermal bath since both Fig. 3.12 and Fig. 3.7 (a) show that very low density of atoms in the triplet states must be expected. The heat bath will tend to thermalize the distribution sketched in Fig. 3.15 (b) broadening it. Ultimately this effect will limit the width of the locking signal. Moreover, the linewidth of the pump beam could also be another potential limitation, we show later this was not the case.

Using the data presented in Fig. 3.18 (a) we calculated an inhomogeneous absorption increase of 41 %. The RMS deviation around all velocity classes shown in the figure is of $\sim 10\%$.

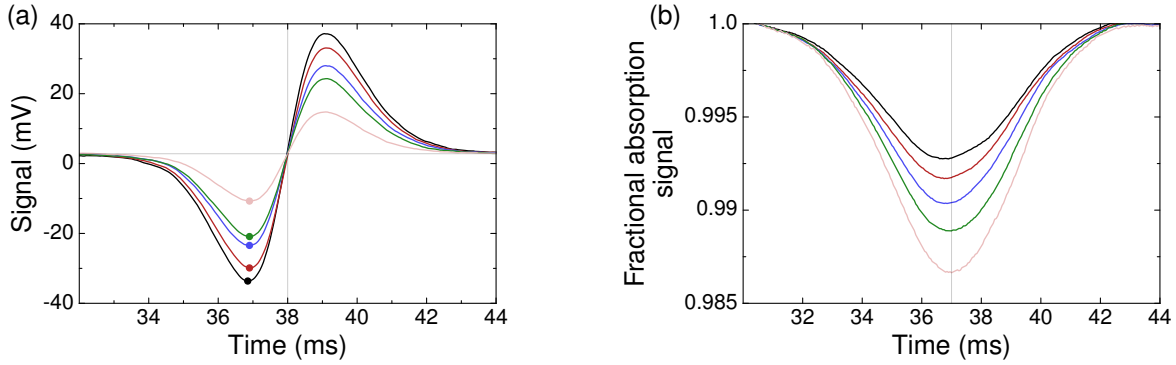


Figure 3.19: (a) Change in the error signal with the probe beam optical power. The signal increases with increasing probe beam power. The colored dots show the minimum of the absorption signal. These stay constant up to a total optical power of 4 mW. (b) Fractional absorption signal corresponding to the results in figure (a). As the atoms get saturated the fractional absorption decreases. However it is the absolute absorption which determines the signal increase in (a). The beam powers are 3.94, 3.1, 2.71, 1.81, 0.9 (mW) from black to light red respectively while the waist is keep constant at 1 mm. The 707 nm beam parameters were 1 mW of power and 1 mm beam waist. For display purposes both images have been averaged a total of 8 times.

To obtain a clear error signal we perform a single demodulation step at 1.6 MHz using a Minicircuits ZPRD-1+ phase detector obtaining Fig. 3.18 (b)¹⁵. Direct comparison between Fig. 3.18 (b) and Fig. 3.14 (b) shows a peak-to-peak voltage increase of a factor of 5. This signal increase is consistent with the estimation made in section 3.2.2¹⁶ if we take into account the real population increase of 41 %.

The peak-to-peak voltage of the error signal is therefore expected to increase with increasing probe beam power. As the distance between both peaks in the frequency scale is limited by the thermalization effects and by the linewidth of the 707 nm transition (which is 4.7 broader than the $5s\ 5p\ ^3P_0 \rightarrow 5s\ 6s\ ^3S_1$ transition) increasing the 679 nm laser power can be done without increasing the separation of both peaks in the frequency scale.

Figure 3.19 (a) shows the error signal for different probe beam powers. The colored dots show the measured point of minimum voltage. The expected behavior is confirmed as the peak height increases while the position of the minimum stays constant. When the power reaches 4 mW a change in the position in frequency scale of the minimum can be detected. This corresponds to a broadened linewidth of $\approx 21\Gamma$. Using this value we can estimate the derivative of the error signal to be:

$$\frac{dV}{d\omega} \approx 3.6 \frac{\text{mV}}{\Gamma}$$

¹⁵The output is low pass filtered using a single pole RC low pass filter with $R=50\ \Omega$ and $C=1\ \mu\text{F}$.

¹⁶In this section we assumed that the signal-to-noise ratio would increase with the ratio of the height of the Lamb dip shown in Fig. 3.12 to the total absorption increase of Fig. 3.18 times 3.

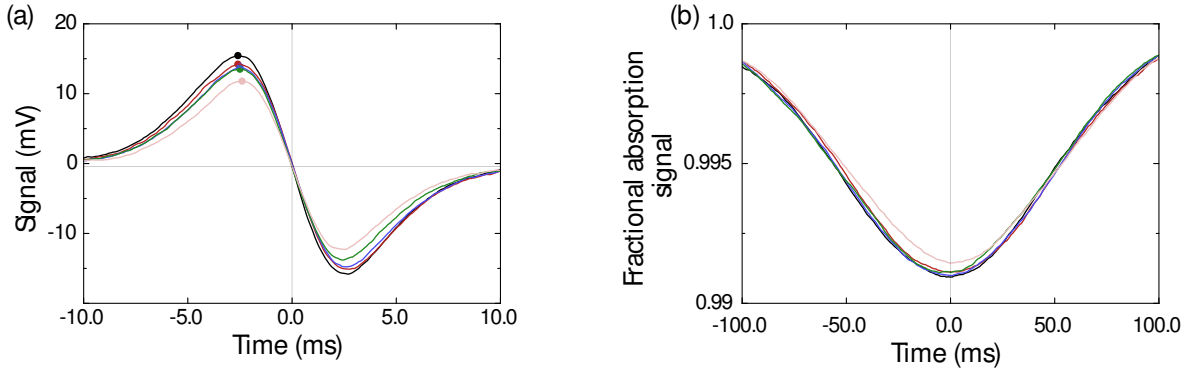


Figure 3.20: (a) Change in the error signal for different pump beam optical powers. (b) Absorption signal corresponding to a. The pump powers are 1,2,3, 3.9, 5 mW while the power of the probe beam is left constant at 0.69 mW. The waists of the beams are kept constant at 1 mm. With increasing power, only small changes on the error signal can be seen. While a small increase on the distance in frequency of the peaks is seen (both figures have been averaged a total of 8 times).

approximately a factor of 10 larger than that obtained in figure Fig. 3.14.

From this measurement we conclude that the distance between both peaks in the frequency scale must be limited by the linewidth of the 707 nm transition or by thermalization effects. To probe the effect of the pump laser on the error signal, we measured the error signal for different pump powers. The signal increase depends directly in the population of the $5s\ 5p\ ^3P_2$ state. As the excited state population is independent of the beam power once the saturation parameter is much larger than one, increasing the power of the pump beam over this limit should have little effect on the peak-to-peak amplitude of the signal. However as the transition gets saturated, the frequency separation should scale as:

$$\Gamma' = \sqrt{1 + s_0} \Gamma, \quad (3.46)$$

where s_0 is the saturation parameter, Γ the linewidth of the transition, and Γ' is the saturated linewidth.

Figure 3.20 (a) shows the change in the error signal for different pump beam powers. As the beam saturation increases, a small change in the peak height and width can be seen. The fractional absorption signal shown in Fig. 3.20 (b) also shows small changes depending on the pump power.

As expected the change in the peak height is small. The change in frequency spread however is smaller than the expected increase from the saturated linewidth. Note that between the black and light red traces there is a factor of 5 in optical power. Therefore an increase of $\Gamma' \approx 2\Gamma$ in frequency spread should be seen. From this measurement we conclude that thermalization or other effects independent of the laser parameters are limiting the derivative $d\omega/dV$ of the error signal. Not shown in the figure is the change in peak-to-peak voltage when the power of the pump beam is changed below

saturation. In this case the changes are quite dramatic and the signal approaches zero rapidly.

Figure 3.21 (a) shows the change in the error signal with the pump beam frequency. Changing the pump beam frequency, changes the velocity class of atoms that this beam addresses, and thus changes the center and the symmetry of the error signal. The absorption profile also becomes displaced and asymmetric [see Fig. 3.21 (b)]. As the zero crossing of the error signal is determined by the pump beam frequency two factors must be taken into account:

- The error in the locking point of the 707 nm laser described in section 3.1.3 will also affect the error in the locking of the 679 nm probe.
- The power spectral density (PSD) measured in Fig. 3.9 will limit the bandwidth and noise suppression of the error signal.

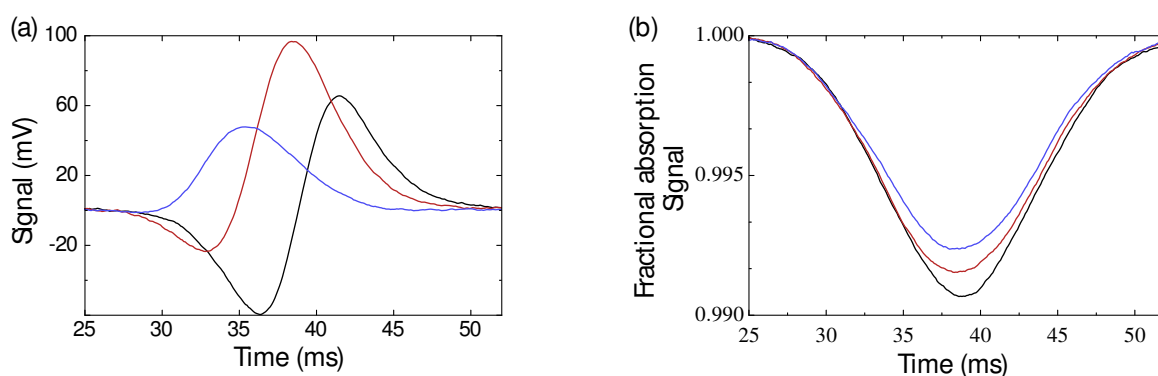


Figure 3.21: (a) Changing the frequency of the 707 nm pump laser offsets the zero of the error signal. (b) Changing the beam frequency also makes the absorption profile slightly asymmetric. The pump and probe beam parameters remain unchanged (6.79 mW and 1 mm waist for the pump and 0.42 mW and 1 mm waist for the probe). The blue profile has an offset of 450 ± 14 MHz from the resonance while the red one has a offset of 300 ± 14 MHz. For display purposes both images have been averaged a total of 8 times.

The final error signal used for locking the laser is shown in Fig. 3.22 (a). We measured the separation between the peaks of the error signal to be $270 \text{ MHz} \pm 14 \text{ MHz}$. Taking into account the peak-to-peak voltage we can estimate the slope of the error signal to be 1.7 MHz/mV or $0.2\Gamma/\text{mV}$. Using Eq. (3.35) we calculate the error in the locking point to be $0.5 \text{ MHz} \approx 0.06\Gamma$. The offset of the signal is $\approx 0.3 \text{ mV}$.

From these measurements and given the data of section 3.1.3 we conclude that the limitation in the locking technique in terms of the error in the locking point and RMS frequency noise is given by the quality of the pump beam lock. Using the data of section 3.1.3 we estimate the final error in the locking point to be 1.8Γ .

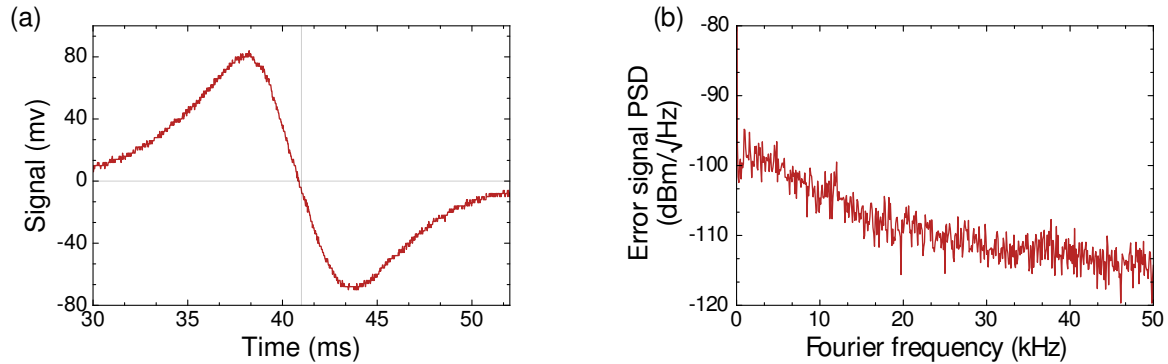


Figure 3.22: (a) Raw data of the final error signal used for laser locking. The measured offset was 0.3 mV which corresponds to a total error in the locking point of 0.5 MHz. (b) Power spectral density of the error signal. The probe beam power was 5.3 mW and the pump beam power was 6.8 mW while the waist of the beams remains unaltered as in Fig. 3.19.

3.3 Conclusions

A compact setup for laser locking both the 707 nm and the 679 nm lasers.

Both setups reported in section 3.1.2 and section 3.2.1 can be combined as shown in Fig. 3.23.

To confirm this we measured the effect of chopping the pump at frequency of 224 kHz in the error signal as done in section 3.1.2. A total reduction of the peak-to-peak voltage of the error signal shown in Fig. 3.22 (a) of a factor of 2 was measured. Mathematically this can be understood, as a square wave $Sq(t)$ can be expanded in a cosine series as:

$$Sq(t) = \frac{H}{2} + \sum_{n=1}^{\infty} a_n \cos(n \omega_0 t),$$

where H is the total amplitude of the square wave, ω_0 is the angular frequency of the wave and a_n are the terms of the expansion given by:

$$a_n = \frac{2}{T} \int_{-T/2}^{T/2} Sq(t) \cos(n \omega_0 t). \quad (3.47)$$

Here T is the period of the wave. The low pass filter will attenuate all of the high frequency harmonics leaving only the DC signal, which is half of the total signal without chopping¹⁷. The low pass with the high frequency chopping amounts to averaging the signal. Since half of the time the signal is on, and half off, the signal is divided by two. The error signal slope will be half of that of signal Fig. 3.22 and, more importantly, the error in the locking frequency will remain unchanged as the DC offset will also be divided by 2.

¹⁷We use a RC low pass filter circuit with a 50 Ω and a ceramic capacitor of capacitance 1 μF .

Two important factors must be taken into account:

- In the same fashion as in Fig. 3.8 (b) intermodulation between the chopping and the frequency modulation could be present. The modulation frequencies reported in section 3.1.2 were optimized to minimize this effect, therefore this should not be an issue.
- The high frequency harmonics will not be completely suppressed and potentially they could couple to the laser. The maximum locking bandwidth however is much smaller than the frequency of the harmonics therefore they should not couple to the laser.

The main challenge will be to overcome the frequency shift caused by the AOM, as shown in Fig. 3.21, as it will change the symmetry of the error signal.

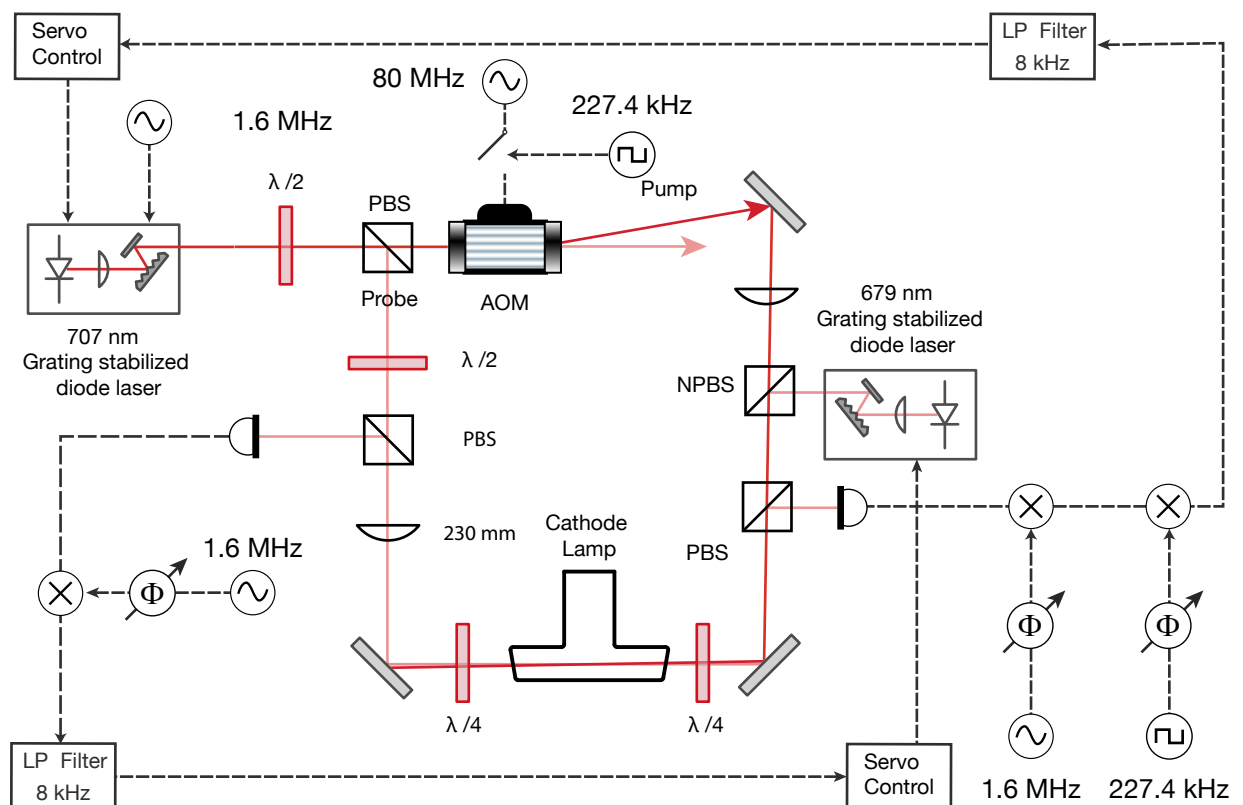


Figure 3.23: Proposed final experimental setup. Both setups can be combined in a single compact unit. Here the same modulation frequencies and the same optical and electrical components as in the cases of section 3.1.2 and section 3.2.1 should be used.

The $5s\ 5p\ ^3P_1 \rightarrow 5s\ 6s\ ^3S_1$ 688 nm laser

A loading rate increase of the blue MOT of up to 65 %, can be obtained by using an extra 688 nm laser resonant with the $5s\ 5p\ ^3P_1 \rightarrow 5s\ 6s\ ^3S_1$ transition [20]. However, to stabilize this laser the authors of Ref. [9] were unable to obtain a high signal-to-noise ratio using the setup reported in section 3.1 and therefore were not able to lock the laser.

The setup described in section 3.2.1 could potentially provide enough signal-to-noise ratio increase to stabilize the laser, because the decay between the $5s\ 5p\ ^3P_1$ state and the ground state is negligible compared to the pumping rate of atoms given in Eq. (3.39).

Chapter 4

A Magnetic Field System for Cooling and Trapping of ^{88}Sr

As explained in Chapter 2, operation of a magneto optical trap (MOT) requires a spatially dependent magnetic field of the form:

$$\begin{aligned}\vec{B}(z, \rho) &= \left. \frac{d\vec{B}(z, \rho)}{dz} \right|_{z, \rho=0} z \vec{e}_z + \left. \frac{d\vec{B}(z, \rho)}{d\rho} \right|_{z, \rho=0} \rho \vec{e}_\rho \\ &\equiv B_z^1(z, \rho=0) \vec{e}_z + B_\rho^1(z=0, \rho) \vec{e}_\rho\end{aligned}\quad (4.1)$$

Here we use the standard notation for cylindrical coordinates where z is the height, and ρ is the radial distance to the symmetry axis of the magnetic field coils. The subscript z refers to the z component of the magnetic field and equivalently for ρ . Adding such field to an optical molasses results in a restoring force for the atoms, confining them.

The coil geometry shown in Fig. 4.1 (a) generates the field described in Eq. (4.1). Here, a pair of identical coils with counter propagating currents ($I_1 = -I_2$) generates a field along the symmetry axis of the system z that can be calculated as [30]

$$B_z^1(z, \rho=0) = \mu_0 I \frac{3 D R^2}{2 (D^2/4 + R^2)} z + \mathcal{O}(z^3), \quad (4.2)$$

where μ_0 is the vacuum magnetic permeability, D is the distance between coils, R is the radius of the coils, and $I = I_1 = -I_2$ is the current running through each of them. The superscript 1 indicates that a total of two coils are used (one at each side). We have set the origin $z = 0, \rho = 0$ at the center point of the coil configuration.

Figure Fig. 4.1 (b) shows the calculated field strength along the z axis for $R=6$ cm, $D=12$ cm and a current $I = I_1 = -I_2 = 10$ A. As can be seen, the field strength of the coils around $z=0$ is well approximated by Eq. (4.2) (Blue dashed line).

Around the origin, the magnetic field dependence along the radial direction ρ can be approximated as [30]

$$B_\rho^1(z=0, \rho) \approx \frac{1}{2} \mu_0 I 3 \frac{D R^2}{2 (D^2/4 + R^2)} \rho. \quad (4.3)$$

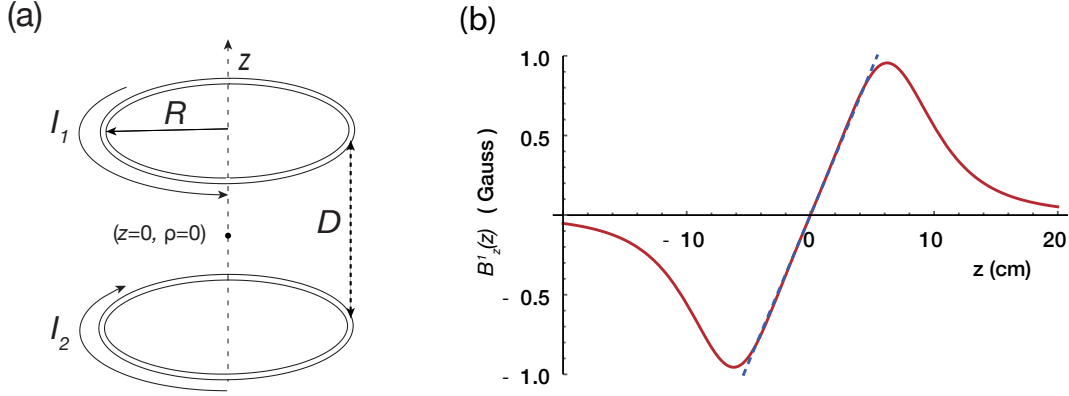


Figure 4.1: (a) Simplified schematic of a magnetic field system for operation of a MOT. (b) Magnetic field created along the z axis by a pair of coils with $R = 6$ cm, $D = 12$ cm, and $I = I_1 = -I_2 = 10$ A (red line). At the center of the system the magnetic field is well approximated by Eq. (4.3) (Blue dashed line).

Equations (4.2) and (4.3) follow the relation

$$\frac{dB_{\rho}^1}{d\rho}(z=0, \rho=0) = \frac{1}{2} \frac{dB_z^1}{dz}(z=0, \rho=0). \quad (4.4)$$

This relation is independent of the number of coils on each side, their radius, and their position. It holds as long as the whole configuration is symmetric around the plane $z=0$. Therefore, the magnetic field around the origin is fully defined by dB_z^N/dz . This justifies the usual convention found in literature where only the magnetic field gradient along the z axis is used to define the magnetic field around the origin. In this thesis, we follow this convention and only quote the magnetic field gradient along the z direction to fully define the field around the origin.

This Chapter is structured as follows:

In section 4.1, we explain the main issues regarding the design of a magnetic field for laser cooling of ^{88}Sr atoms. When possible, the arguments in this section will be kept general. The main issues are the field stability during the operation of the red MOT, fast switching of the magnetic field gradient, mechanical stability of the coil mount, and the dissipated electrical power of the system.

The solution to these issues is addressed in different sections:

1. In section 4.2, we show how to measure and control the current in a precise and reliable way.
2. In section 4.3, we explain how to control the switching time of the coils. Fast switching of the magnetic fields is required to prevent atoms losses during switching between the red and the blue MOTs.

3. In section 4.4, we explain how we optimized the geometry of the coils to obtained faster switching time.
4. In section 4.5, we explain how we improved the mechanical stability of the MOT coil base.
5. In section 4.6, we describe what measures were taken to reduce the total dissipated electrical power in the system.

Finally, in section 4.7 we will end the Chapter with a description of the compensation coils to cancel Earth's magnetic field.

4.1 Design considerations

In this section, we introduce the main considerations that led to the design of the magnetic field system.

4.1.1 Field Stability

The Zeeman shift of the magnetic m_f states in the $5s\ 5p\ ^3P_1$ state of ^{88}Sr is $2.1\ \text{MHz/G} \times m_f$ [4]. A field change of $3.5\ \text{mG}$ during the operation of the red MOT shifts the red transition by its linewidth. Therefore, during the operation of the red MOT, an absolute stability of the magnetic field better than $3.5\ \text{mG}$ is needed.

For the coil configuration given in Fig. 4.1 (a), with $R=6\ \text{cm}$ and $D=12\ \text{cm}$, we obtain that a current imbalance between the two coils ($\Delta I = |I_2 - I_1|$) of $0.1\ \text{A}$ results in a total field change of $|B| = 3.7\ \text{mG}$. In this configuration, the current needed for the red MOT is $100\ \text{A}$. Therefore, a current stability of $\Delta I/I \approx 10^{-3}$ is required.

Assuming we are using N pairs of coils instead of one we obtain the same result for the relative current stability $\Delta I/I$. To show this we need to take into account that the field created by a single circular current loop on its axis is [31]:

$$B_z^1(z, I) = \frac{\mu_0}{2} \frac{R^2}{((z \mp D/2)^2 + R^2)^{3/2}} I, \quad (4.5)$$

where we follow the convention shown in Fig. 4.1 (a). Here, the coils are located at $z = \pm D/2$. By the superposition principle the field created by N current loops will be:

$$B_z^N(z, I) = \frac{\mu_0}{2} \frac{R^2}{(z \mp D/2)^2 + R^2)^{3/2}} N I. \quad (4.6)$$

Here we are neglecting the finite size of the wire, therefore all the loops can occupy the same location in space. The field at $z=0$ becomes:

$$B_z^N(0, I) = \frac{\mu_0}{2} \frac{R^2}{(D^2/4 + R^2)^{3/2}} N I = C N I \quad (4.7)$$

where C is just a proportionality constant given by:

$$C \equiv \frac{\mu_0}{2} \frac{R^2}{(D^2/4 + R^2)^{3/2}} \quad (4.8)$$

and the direction of the field depends on the sign of the current. The change in the magnetic field created by a current imbalance of ΔI in the magnetic system can be calculated using Eq. (4.7). As the total field is linear in the current, and $B(I) = B(-I)$, the total field created by the current imbalance at $z=0$ will be:

$$\Delta B_z^N = B_z^N(0, I) + B_z^N(0, \Delta I) + B_z^N(0, -I) = B_z^N(0, \Delta I) = C N \Delta I, \quad (4.9)$$

The field gradient produced by N pairs of coils will be the sum of the gradient created by each pair:

$$\frac{dB_z^N}{dz}(z=0) \approx N \frac{dB_z^1}{dz}(z=0) = \mu_0 3 \frac{D R^2}{2 (D^2/4 + R^2)} N I = C' N I, \quad (4.10)$$

where C' is another proportionality constant given by:

$$C' \equiv \mu_0 3 \frac{D R^2}{2 (D^2/4 + R^2)}. \quad (4.11)$$

Using equations (4.9) and (4.10) we obtain for the total current imbalance:

$$\frac{\Delta I}{I} = \frac{\Delta B}{dB/dz(z=0)} \frac{C'}{C} = \frac{\Delta B}{dB/dz(z=0)} 3 D \left(\sqrt{D^2/4 + R^2} \right) \approx 10^{-3}. \quad (4.12)$$

Here we have assumed infinitely thin wire therefore, depending of the configuration, small deviations should be expected.

Note that Eq. (4.12) only depends on the relative distances between the coils and their radius therefore the require current stability is independent of the geometry and a current control system with relative stability of $\frac{\Delta I}{I} \approx 10^{-3}$ is needed.

4.1.2 Switching Time

The optimal detuning for performance of the MOT is given by $\Delta = -\Gamma/2$ [11]. Using this detuning the size of the MOT region where atoms interact with light, given by Eq. (2.32), becomes:

$$\Delta z = 2 \frac{\hbar \Gamma}{\mu_B g_j m_j dB/dz 2'} \quad (4.13)$$

where Γ is the linewidth of the transition.

Equation (2.32) gives the size of the region where atoms interact with laser light. In steady state this size is equal to the size of the atom cloud. We can see that the size of

the region where atoms interact with light is much larger for the blue MOT than for the red MOT (for the same field gradient), as $\Gamma_b \approx 4000 \Gamma_r$, where Γ_b is the linewidth of the blue MOT transition and Γ_r is the linewidth of the red MOT transition. One could use Eq. (2.32) to calculate the ratio between both regions. However, the result would not be realistic, as the linewidth of the red MOT lasers is artificially broadened to increase the capture velocity of the red MOT. However it is true that the size of the red MOT is much smaller than the size of the blue MOT (for the same field gradient).

When switching one needs to match the size of the trap to the size of the atomic cloud. This is done by changing the field gradient. The field gradient needs to be changed before the atoms are lost.

To estimate the time it takes for the atoms to be lost we can use the Maxwell-Boltzmann distribution [23] and the experimentally determined final temperature of the blue MOT of $T \approx 1\text{mK}$ [4] to calculate the average velocity of the atoms after the blue MOT:

$$\langle v \rangle = \sqrt{\frac{8 k_B \times 1\text{mK}}{m_{Sr} \pi}} = 0.49 \text{ m/s}, \quad (4.14)$$

where k_B is the Boltzmann constant and m_{Sr} is the mass of the strontium atom. Using the size of the red MOT $\Delta z_r \approx 220 \mu\text{m}$, as measured by the authors of Ref. [32], we estimate that the majority of atoms will leave this region in a time:

$$t_s \approx \frac{220 \mu\text{m}}{0.42\text{m/s}} = 0.045 \text{ ms}. \quad (4.15)$$

The magnetic field gradient needs to be switched in this time frame to change the confining potential and prevent losses. Experimentally a switching time of $\sim 0.1 \text{ ms}$ is found to be sufficient [4].

The energy stored in each of the coils needs to be released within this time-frame. The energy stored in a coil E_c follows the relation [31]:

$$E_c = \frac{1}{2} L I^2, \quad (4.16)$$

where L is the self-inductance of the coil, and I is the current running through coil. The energy that needs to be released follows the relation¹:

$$\Delta E_c = \frac{1}{2} L (I_b^2 - I_r^2), \quad (4.17)$$

where I_r is the current needed for the red MOT and I_b is the current needed for the blue MOT.

¹For this calculation we have neglected the interaction between the coils. This will be justified in section section 4.1.3.

This energy needs to be released in a time t_s . Using Eq. (4.10) and the typical magnetic field gradients for operation of the blue and the red MOT, $\frac{dB}{dz}(z=0) \approx 52$ G/cm and ≈ 2 G/cm respectively [4], we can calculate the ratio of the currents

$$\frac{dB_N}{dz}_1 / \frac{dB_N}{dz}_2 = I_1/I_2. \quad (4.18)$$

Thus, the currents follow the relation given by:

$$I_b = \frac{52}{2} I_r = 26 I_r, \quad (4.19)$$

Therefore, $I_b \gg I_r$, and we can approximate the energy to be dissipated as:

$$\Delta E_c \approx \frac{1}{2} L I_b^2, \quad (4.20)$$

The self-inductance of a coil can be estimated using the equation [33]:

$$L \approx N^2 R \mu_0 \left(\log \left(\frac{8R}{a} \right) - 2 \right), \quad (4.21)$$

where a is the radius of the conducting cross section of the wire.

At this point we need to use the parameters of our coil system to proceed with the estimation. The justification of the parameters chosen will be given in section 4.3. For our magnetic field system we use a pair of coils with $N = 36$ and average radius $\langle R \rangle = 8.6$ cm. Since we use square wire of cross section 12 mm^2 we estimate the effective radius of the square wire a_{ef} using

$$\pi a_{ef}^2 = 12 \text{ mm}^2, \quad (4.22)$$

to obtain $a_{ef} \approx 2 \text{ mm}$. Using Eq. (4.21), we estimate the self-inductance of the coil system to be $L \approx 140 \mu\text{H}$. The measured inductance is $220 \pm 20 \mu\text{H}$ which shows that Eq. (4.21) can only be used as a very rough estimate. In section 4.4 we show a more accurate way of estimating the self-inductance of a coil.

The operational current of the blue MOT will be 150 A. The energy stored in the field of the coil can be calculated using Eq. (4.20) to be 1.5 J. This energy needs to be dissipated in a time $\Delta t = 0.05 \text{ ms}$.

During switching the total dissipated power is:

$$\Delta P = \frac{\Delta E_c}{\Delta t} \approx 33 \text{ kW}. \quad (4.23)$$

During the switching time, the total voltage across the wire will be [31]:

$$\Delta V = L \frac{dI}{dt} \approx L \frac{\Delta I}{\Delta t} \approx 466 \text{ V}. \quad (4.24)$$

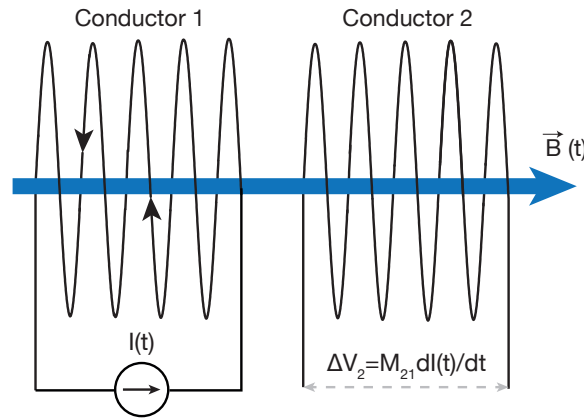


Figure 4.2: System of two conductors, a current change in conductor one (CO1) will induce a voltage in conductor two (CO2) given by $\Delta V = M_{21} I_1$.

Both equations (4.23) and (4.24) show that we need to deal with high powers and voltages. Therefore, the switching of the coils is challenging. In section 4.3, we show how we overcome these problems.

Using Eq. (4.16) and Eq. (4.24), we obtain the switching time of the MOT coils:

$$\Delta t \approx L \frac{I_b}{\Delta V} \approx 2 \left(\frac{1}{2} L I_b^2 \right) \frac{1}{I_b \Delta V} = \frac{2 E_c}{I_b \Delta V}. \quad (4.25)$$

The energy stored in the magnetic field E_c is approximately constant for our experiment as the magnetic field gradient is a fixed experimental parameter 52 G/cm (we showed in Fig. 4.1 (b) the magnetic field is well approximated by the gradient at the center). Therefore, $\Delta t \propto 1/I_b$.

Alternatively, this relation can be deduced from Eq. (4.10) and Eq. (4.21). The switching time follows the relation:

$$\Delta t \approx L \frac{I_b}{\Delta V} = \frac{1}{\Delta V} N^2 R \mu_0 \left(\log \left(\frac{8 R}{a} \right) - 2 \right) \frac{dB_z^N}{dz}(z=0)/C N \propto N \propto 1/I_b \quad (4.26)$$

Equations (4.25) and (4.26) show that for a fixed distance between the coils and fixed radius, the most efficient configuration is the one that requires the most current.

4.1.3 Mechanical Stability

The voltage through a coil is dependent on the conductors around it. As shown in Fig. 4.2, conductor one (CO1) creates magnetic flux through a second conductor (CO2). According to Faraday's law of induction, the voltage across the coil is [31]:

$$\Delta V_2 = -\frac{d\phi_B}{dt}, \quad (4.27)$$

where ϕ_B is the magnetic field flux through CO2 created by CO1, and V_2 is the voltage measured at CO2.

Equation (4.27) can be reformulated to be [31]

$$\Delta V_2 = M_{21} \frac{dI_1}{dt}, \quad (4.28)$$

where M_{21} is known as the mutual inductance between CO1 and CO2. The mutual inductance is a geometrical factor which follows the relation:

$$M_{21} = M_{12}, \quad (4.29)$$

and it is independent of the current. The voltage V_1 created by CO2 also follows the same relation:

$$\Delta V_1 = M_{12} \frac{dI_2}{dt}, \quad (4.30)$$

and the total voltage across each of the coils follows:

$$\Delta V_2 = M_{21} \frac{dI_1}{dt} + L \frac{dI_2}{dt} \quad \Delta V_1 = M_{21} \frac{dI_2}{dt} + L \frac{dI_1}{dt},$$

where we have used Eq. (4.24) and assumed that the self-inductance of each of the conductors is the same. The power dissipated by each of the coils follows the relations [34]:

$$\begin{aligned} dE_1/dt = P_1 &= I_2 V_2 = M_{21} I_2 \frac{dI_1}{dt} + L I_2 \frac{dI_2}{dt}, \\ dE_2/dt = P_2 &= I_1 V_1 = M_{21} I_1 \frac{dI_2}{dt} + L I_1 \frac{dI_1}{dt}. \end{aligned} \quad (4.31)$$

The energy stored in each of the coils can be calculated to be

$$\begin{aligned} E_1 &= \int M_{21} I_2 dI_1 + L I_2 dI_2, \\ E_2 &= \int M_{21} I_1 dI_2 + L I_1 dI_1, \end{aligned} \quad (4.32)$$

and the total energy of the system is equal to the sum of each contribution of Eq. (4.32):

$$\begin{aligned} E_t &= \int M_{21} (I_2 dI_1 + I_1 dI_2) + L (I_2 dI_2 + I_1 dI_1) \\ &= \int M_{21} d(I_2 I_1) + \frac{L}{2} (dI_2^2 + dI_1^2) = M_{21} I_2 I_1 + \frac{L}{2} (I_2^2 + I_1^2), \end{aligned} \quad (4.33)$$

where the integration constant can be shown to be 0 using the conditions, $E_t = 0$ when $I_1 = 0$ and $I_2 = 0$.

The energy given in Eq. (4.33) has two main contributions, the energy of each coil given by the factor proportional to the self-inductance L , and the interaction energy

between the two conductors given by the factor proportional to the mutual inductance M_{21} . Note that the interaction energy:

$$E_i = M_{21} I_2 I_1,$$

can be negative, when the two coils have opposing currents. This can be understood as the energy stored in the magnetic field is given by [31]:

$$E_b = \int_{\mathbb{R}^3} \frac{1}{2 \mu_0} \vec{B}^2(\mathbf{r}) d^3r = \int_{\mathbb{R}^3} \frac{1}{2 \mu_0} (\vec{B}_1(\vec{r}) + \vec{B}_2(\vec{r}))^2 d^3r. \quad (4.34)$$

Here $\vec{B}_1(\vec{r}) + \vec{B}_2(\vec{r})$ is the field created by CO1 and CO2 respectively. When the currents are counter propagating, the fields oppose each other and reduce the total energy stored in the magnetic field.

If $D > R$, then $M_{21} \ll L$ and $E_i \ll E_c$, where E_c is the energy stored in a single coil given by Eq. (4.20). This justifies the approximation made in Eq. (4.17) where we neglected the interaction energy.

The magnitude of the force between the two conductors can be calculated using

$$|\vec{F}_m| \approx |\mathbf{grad} E_t| = |\mathbf{grad} M_{21} I_2 I_1|. \quad (4.35)$$

The mutual inductance of two coils can be approximated by [35, 36]

$$M_{21} \approx N_1 N_2 \frac{(4\pi) R}{\mu_0 2^{3/2}} \left(\frac{1 - \sqrt{k}}{1 + \sqrt{k}} \right)^{3/2}, \quad (4.36)$$

where N_1 and N_2 are the number of loops on CO1 and CO2 respectively, and k is

$$k = \frac{D}{\sqrt{D^2 + 4 R^2}}. \quad (4.37)$$

Equation (4.36) is known as Nagaoka's first formula, and it is only valid when the coils are far away from each other, $D \gg R$. Although this is not the case for our coil system as $D=15$ cm and $\langle R \rangle=8.6$ cm, we use the formula to estimate the following parameters of the system:

$$|\vec{F}_m| = \frac{dM_{21}}{dD} I_1 I_2 \approx 4.1 \text{ N}, \quad |E_i| = 0.26 \text{ J}, \quad (4.38)$$

where the force is repulsive between the two coils and we have used $I_1 = -I_2 = 150$ A.

When switching, the change in force per unit of time is

$$\left| \frac{dF_m}{dt} \right| \approx \left| \frac{\Delta F}{\Delta t} \right| = 41 \text{ kN/s}. \quad (4.39)$$

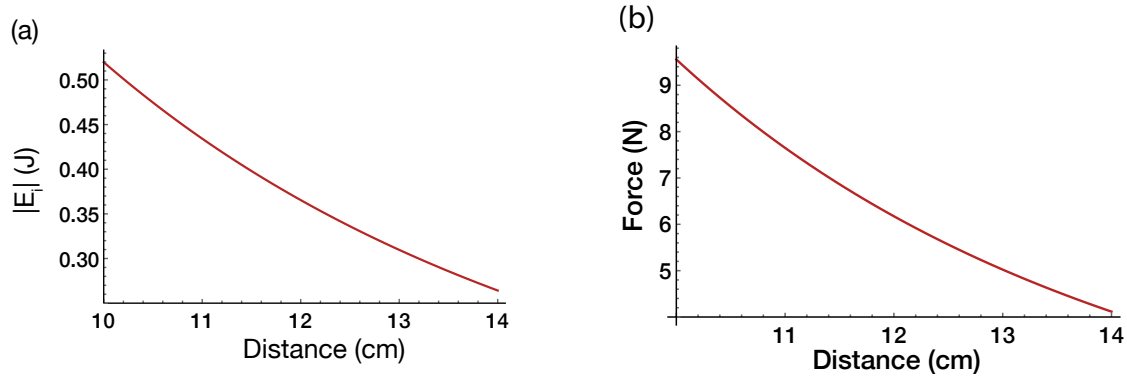


Figure 4.3: (a) Estimation for the absolute value of the interaction energy of the coil system (b) Force between the coils as a function of the separation between them. This calculations were made using equations (4.36).

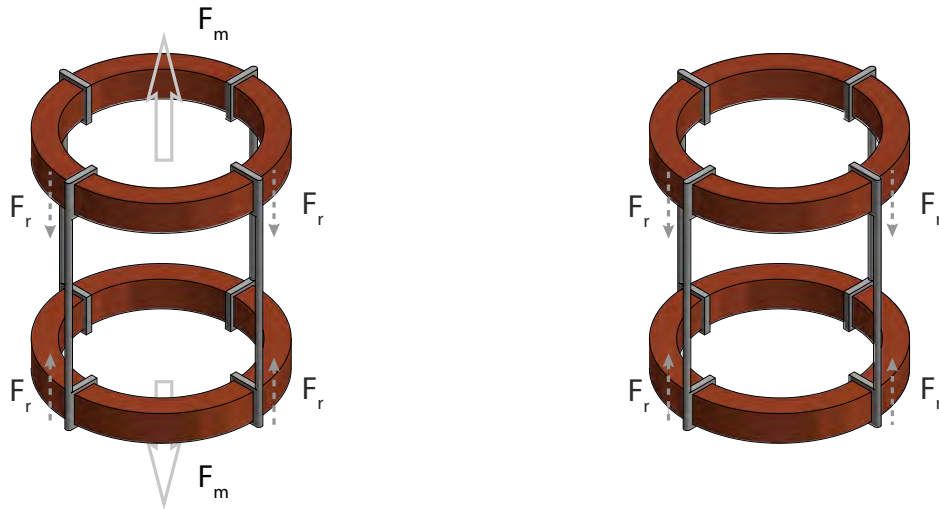


Figure 4.4: Diagram of the forces acting on the coils (a) When the system is on equilibrium, with a constant current running, the base that holds the coils reacts with a force F_r of equal magnitude but opposing direction F_m . (b) When the field is switched off a transient occurs, applying force to the base and creating vibrations. These vibrations must be dissipated on a timescale of 1 ms.

Figure 4.4 shows a diagram of the forces acting on the system in equilibrium (a) and during switching (b). In equilibrium, all the forces must add up to zero. Therefore, the base applies a force F_r with equal magnitude but opposing direction as F_m . When the field is switched off, a force imbalance occurs as F_m becomes zero in 0.1 ms. Then, the force applied by the base is dissipated, creating vibrations. The amplitude of these vibrations must be dissipated in 0.05 ms. Also, the long term mechanical stability must not be influenced by these vibrations. In section 4.5, we show how this issue is addressed.

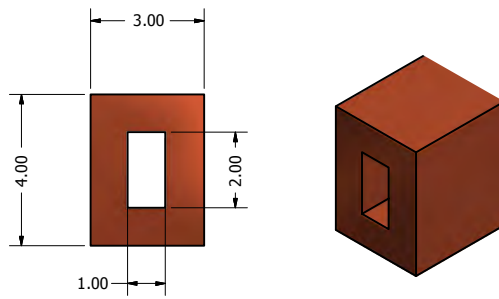


Figure 4.5: Sketch of the wire geometry. Dimensions are given in mm.

4.1.4 Dissipated Electrical Power

The dissipated electrical power due to Joule heating follows the relation:

$$P = V I = \frac{V^2}{R} = R I^2 \quad (4.40)$$

For our coil system, we need a total current of 150 A to obtain a field gradient of 52 G/cm. The total resistance of the wire is ≈ 43 m Ω . Using Eq. (4.40) we obtain a total dissipated power of ≈ 500 W. This power will be dissipated in the wire, heating it. In the absence of water cooling, for a current of 60 A, we measured a temperature higher than 60 °C using our final magnetic system. To be able to run such high currents, we used water cooled wire. A sketch of the wire geometry can be found in Fig. 4.5. The thickness of the wire is 3 mm \times 4 mm. The wire is hollow inside with the dimension of the inner part being 2 mm \times 1 mm.

More importantly, the power dissipated in the wire is approximately independent on the coil configuration. For a fixed distance between the coils, the power dissipated in the wire only depends on the available conducting cross section of the solenoid. To understand this, we need to take into account that the resistance of the wire follows the relation:

$$R = \frac{\rho L_w}{S}, \quad (4.41)$$

where L_w is the length of the wire, ρ is the resistivity of the conducting material and S is the cross section of the wire.

The length of the wire is $L_w = 2 \pi R N$ where N is the number of windings. If the total available cross section of the solenoid S_t is constant, then the cross section of the wire, S is $S = S_t/N$. The total resistance then scales as :

$$R = \frac{\rho L_w}{S} = \frac{\rho 2 \pi R N^2}{S_t}. \quad (4.42)$$

For our experiment, we need a magnetic field gradient of 52 G/cm. Using this gra-

dient and Eq. (4.10) we obtain:

$$I = \frac{52 \text{ G/cm}}{C' N} \propto 1/N. \quad (4.43)$$

The total dissipated power becomes:

$$P = R I^2 = \left(\frac{52 \text{ G/cm}}{C' N} \right)^2 \frac{\rho 2 \pi R N^2}{S_t} = \left(\frac{52 \text{ G/cm}}{C'} \right)^2 \frac{\rho 2 \pi R}{S_t}, \quad (4.44)$$

This equation is independent of N . Ideally, the total conducting cross section of the solenoid S_t needs to be maximized to minimize the dissipated power in the wire. In our case, however, we choose the geometry of the wire to minimize the interference with other parts of the experiment.

In the final setup, each of the coils shown for the experiment has 36 windings. Each of these are made with 3 different coils to increase the water flow through the system.

To decrease the resistance of the wire connectors, a custom made set of connectors was designed. The design is shown in Fig. 4.6. The leads of the wire are soldered to copper blocks of dimensions $25\text{mm} \times 35\text{mm} \times 20\text{mm}$. A pipe thread in the other side allows water flow. On the top side, a set of jumpers allows modification of the directions of current through the coil system.

4.2 Current Control

Current Measurement

In section 4.1.1 we showed that the required current stability for operation of the red MOT is $\frac{\Delta I}{I} \approx 10^{-3}$. Assuming infinitely thin wires, we showed that this to be independent of the coils. To measure the current in the circuit, one could use a resistor in series with the coil. By measuring the voltage drop across it and using Ohm's law, one can obtain the current. Two things must be consider:

- The power dissipated in the resistor is $P = R I^2$. For a 0.1Ω resistor and the current of the red MOT $\approx 6 \text{ A}$, we need a power coefficient of the resistor² of $2.7 \times 10^{-6} \Omega/\text{W}$ to obtained the desired stability in the measurement of the voltage. Moreover, for the operation of the blue MOT, the current rating of the resistor must be 150 A.
- Due to the high voltage present during the transient a direct measurement is undesirable.

²The power coefficient is defined as the change in resistance ΔR as a function of dissipated power P in the absence of external cooling.

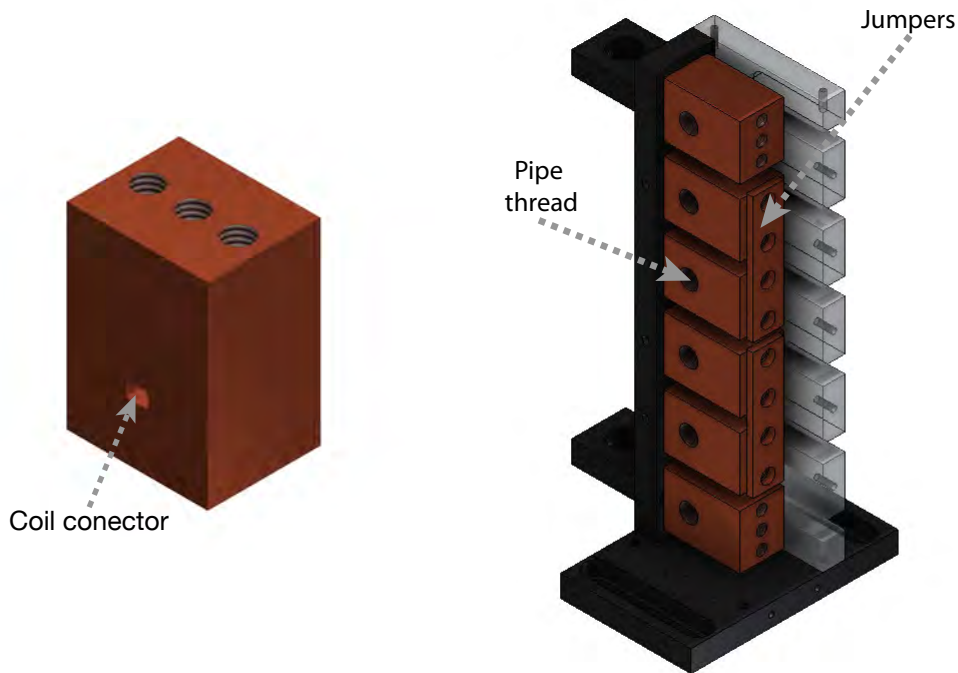


Figure 4.6: Left: Blocks to connect for the wires. The wires are soldered directly into the coil connectors. Right: Complete assembly of the connectors. The black parts are made from polyoxymethylene, the brown parts are made from copper, and the transparent parts are made from acrylic glass.

For these reasons we use a different approach. A current transducer from LEM (It 205-S ultrastab) can provide a high precision current measurement, $\frac{\Delta I}{I}$ of 0.1 ppm. The device works using an indirect measurement of the current. The current transducer works by measuring the magnetic flux through a ferrite material created by the magnetic field of the wire. The specifics on how this is done are very complex and will not be explained here. An explanation of the working principle of the transducer can be found in Refs. [37, 38].

The output of the transducer is a current proportional to the current running through the MOT coils with a conversion factor of 10^{-3} :

$$I_{tr} = 10^{-3} I_c, \quad (4.45)$$

where I_{tr} is the output current of the transducer and I_c is the current running through the coil. Precise measurement of I_{tr} is required. This can be done using a stable resistor and measuring the voltage drop across it.

The measurement electronics are described in Fig. 4.7. We use a 30Ω ultra-stable resistor from Vishay (VPR211-SZT). The power coefficient of the resistor is 4 ppm/W. During operation of the red MOT, the current running through the resistor 30Ω will

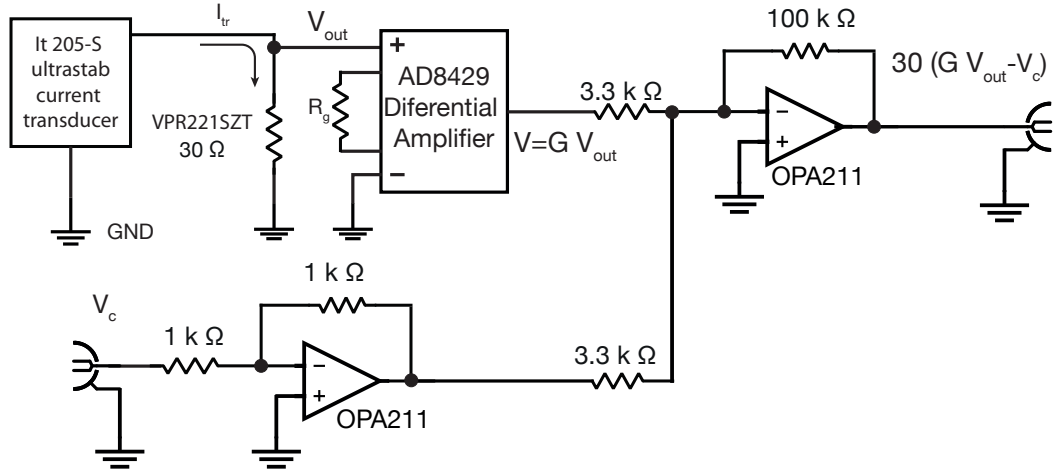


Figure 4.7: Simplified schematic of the current measurement electronics. A current transducer generates a current proportional to the total current running through the MOT coils. A $30\ \Omega$ resistor transforms this current into a voltage. This output is amplified by an AD8429 instrumentation amplifier set at gain $G=4$. The voltage noise of the amplifier will limit the operation of the circuit at low currents to $\frac{\Delta I}{I} = 1.6\text{ppm}/\sqrt{\text{Hz}}$.

be $\approx 6\ \text{mA}$. This results in a total dissipated power of $\approx 1\text{mW}$. For this power, we estimate the change in resistance as $\Delta R = 4 \cdot 10^{-3}\text{ppm}$ (This value is obtained by taking into account the value of the power coefficient of the resistor). The change in resistance during the operation of the blue MOT will be $2.7\ \text{ppm}$. The voltage drop across the resistor is amplified using a differential amplifier (AD8429) by a factor $G = 4$. The voltage noise of the amplifier of $\approx 50\ \text{nV}/\sqrt{\text{Hz}}$ shows that a total current noise power spectral density of $\frac{\Delta I}{I} \approx 1.6\ \text{ppm}/\sqrt{\text{Hz}}$ must be expected. We expect the differential amplifier to be the limiting factor for the performance of the circuit.

As described in the circuit diagram in Fig. 4.7, we use a voltage adder built with two operational amplifiers to generate the error signal for feedback control (the difference between the desired and measured signal). There is an extra current monitoring path which is not shown in the figure. A complete diagram of the circuit along with schematics of the PCB is shown in appendix B.

The total output voltage of the circuit in terms of the current running through the coils is $V = 30 (30 G_{tr} G I_c - V_c)$, where G_{tr} is the gain in the transducer and I_c is the current running through the coils.

To characterize the circuit, we measure the output of the circuit when the control voltage is grounded. The results are shown in Fig. 4.8. The red dots are the measured data points and the black dashed line is a linear fit to the data points. The slope of the fit is $m = 3.536\ \text{V/A}$ with a standard deviation of $0.007\ \text{V/A}$. The standard deviation is limited by the amperemeter used to measure the current. The standard deviation of

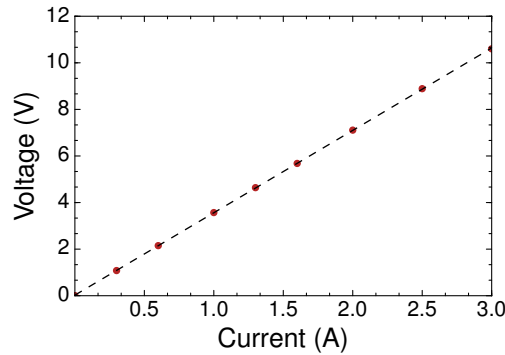


Figure 4.8: Response of the sensing circuit for different currents when V_c is put to ground. The size of the y error bars is much smaller than the size of the dots. This were given by the noise of the voltage measurement device to be $\approx 500\mu\text{V}$. The error in the current measurement is given by the amperimeter used to calibrate the current to be 10 mA. The measured slope is 3.536, $\sigma = 0.007$.)

the fit gives an upper bound on the precision of the current measurement to be $\frac{\Delta I}{I} < 10^{-3}$ and shows that the desired current stability of $\frac{\Delta I}{I}$ can be achieved. The calculated gain using $V = 30(30 G_{tr} G V_{out})$, shows a transducer gain of $9.8 \cdot 10^{-4}$. The difference between this value and the expected transducer gain of 10^{-3} given by the data-sheet can be explained by the tolerances in the value of the resistors used in the electronics.

Current Control

To stabilize the current during operation of the blue and red MOT, we use a power metal–oxide–semiconductor field-effect transistor (MOSFET) from Semikron (SKM111-AR)³. The current rating of the MOSFET is 600 A, and the breakdown voltage is 100 V. The MOSFET is used in series with the IGBT. We use a single proportional-integral (PI) feedback loop to control the current through the coil as shown in Fig. 4.9. The feedback is performed at the gate of the MOSFET⁴. A custom made PI PCB was designed for this purpose. A diagram of the control circuit is shown in Fig. 4.10⁵.

4.3 Fast Switching Circuit

Consider the simplified switching circuit shown in Fig. 4.11. At $t_0 = 0$, the switch starts opening. In a finite time interval $\Delta t = t_f - t_0 = t_f$, the current goes to zero. Using Kirchhoff's circuit laws [34], we can calculate the voltage drop across the switch to be:

$$\Delta V_s = V_+ - \Delta V_L = V_+ - V L dI/dt. \quad (4.46)$$

³See Ref. [39] for an explanation on the working principles of MOSFETs.

⁴The specifics on feedback control are not described here, see Ref. [28] for review on feedback control.

⁵The specifics of PI controller design can be found in Ref. [34] and are not given here.

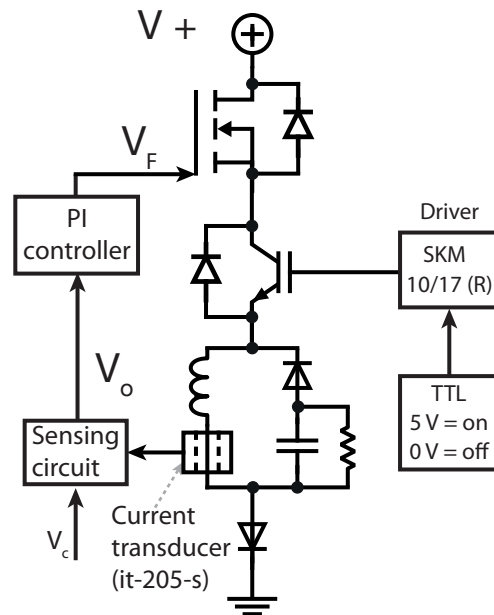


Figure 4.9: Schematic of the complete switching circuit where we have added the feedback elements for current control. Here V_c is the control voltage. The control voltage is a function of the desired current as $V_c = 120 I_c A$. A driver [SKM 10/17 (R)] is used for fast switching of the insulated gate bipolar transistor (IGBT). The details on the fast switching circuit are explained in the next section. For 5 V input signal the IGBT is conducting, for 0 V signal the IGBT is non-conducting.

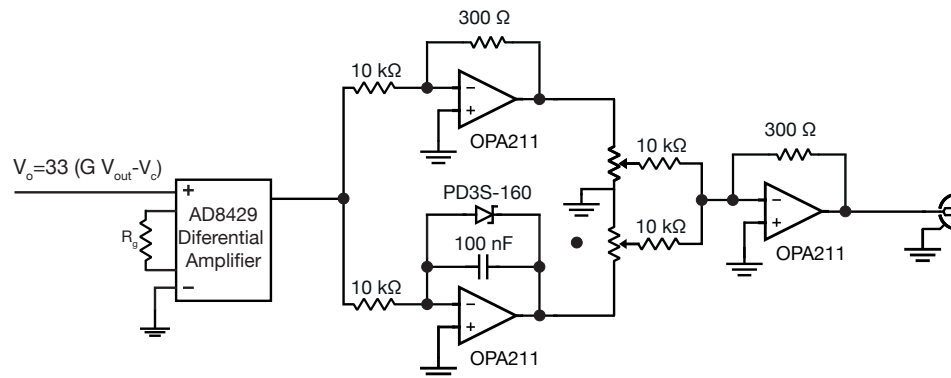


Figure 4.10: Simplified diagram of the control PCB board. For feedback control we used a proportional and integral stage. To prevent integrator windup (this is a typical issue with feedback in non-linear systems. An explanation of this issue can be found in Ref. [28]). We use a Schottky diode (PD3S-160) which prevents the 100 nF capacitor from having reverse negative voltage. This has the disadvantages of adding a non-linear element on the feedback circuit. Alternatively an analog switch could be used.

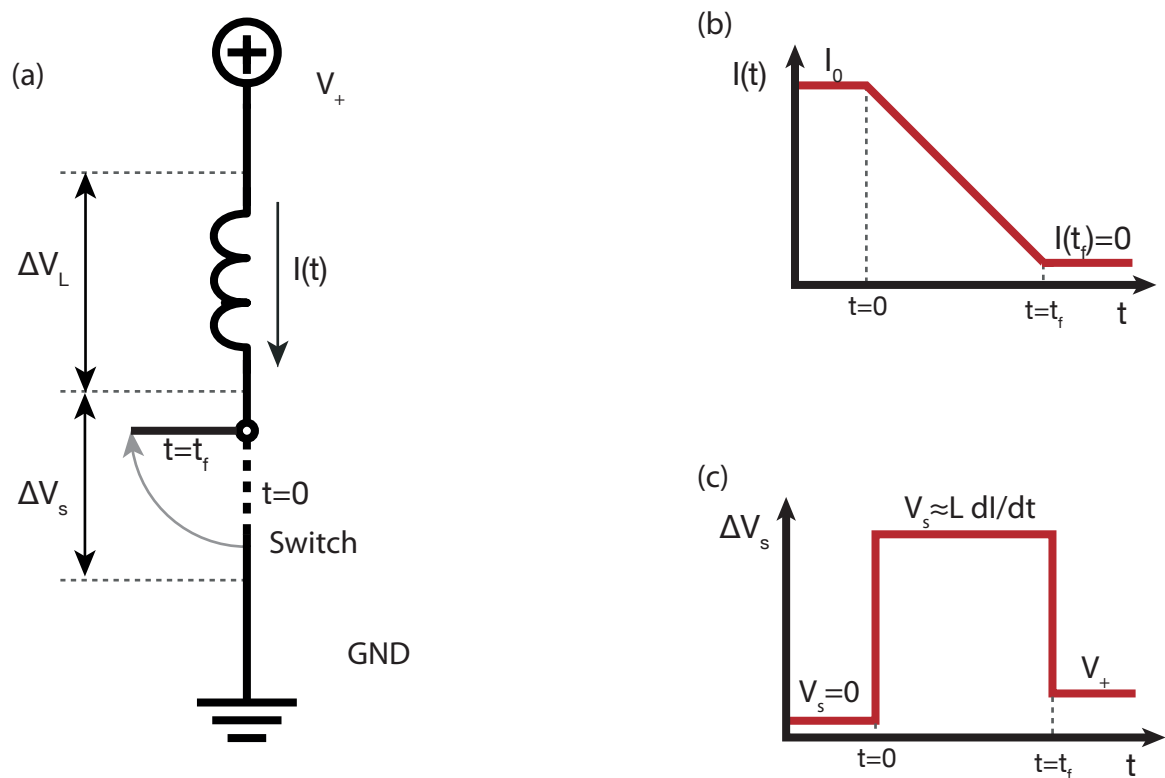


Figure 4.11: (a) Simplified schematic of the switching circuit. (b) Sketch of the current dependence as a function of time. At $t = 0$ the switch starts opening. At $t = t_f$ the current is switched off. (c) Sketch of the voltage drop over the switch. For $t < 0$ the switch is fully conducting and the voltage drop is zero. During the transient, from $t = 0$ to $t = t_f$, the voltage drop follows the relation $V_s = V_+ - V_L \approx V_L = L \, dI/dt$ (here we assume that $V_+ \ll V_L$ and a linear current change during the transient). For $t > t_f$ the voltage drop in the coils is zero and all the voltage drop of the switch is V_+ .

If $V_+ \ll L \, dI/dt$ then Eq. (4.46) becomes:

$$\Delta V_s \approx \Delta V_L = -V L \, dI/dt. \quad (4.47)$$

In a very simplified manner, a real switch can be characterized by two values: its response time or the time it takes to completely switch of the current and the breakdown voltage. The breakdown voltage V_{br} defines the point where the switch starts conducting again i.e. when $V_s > V_{br}$, the switch closes and the current starts flowing.

The voltage drop across our coil system during switching is given by Eq. (4.24) to be $\Delta V \approx 460$ V. Equation (4.47) shows that $\Delta V_s \approx \Delta V_L$, therefore the breakdown voltage of our switch V_{br} must be higher than this value, $V_{br} > 460\text{V}$. Moreover, the response time of the switch must be $\ll 0.05$ ms.

Equation (4.24) assumes the current change during switching is linear during the transient and zero elsewhere [See Fig. 4.11 (b)]. This current change assumes a voltage change of the form shown in Fig. 4.11 (c). The voltage here is discontinuous at $t = 0$ and $t = t_f$, which is clearly a non-physical situation. In reality, the voltage change is smoother, limiting the current change. Therefore, $\Delta V = 460\text{V}$ must be taken as a lower limit for the breakdown voltage of the switch to obtain the desired switching time (the derivative of the current is $dI/dt = V/L$).

During the continuous operation of the blue MOT, a current of 150 A will run through the switch. The current rating of the switch must be higher than this value. To address these switching requirements, we used a similar setup as the one described in Ref. [40].

A schematic of the switching circuit is given in Fig. 4.12 (a). We use an insulated gate bipolar transistor (IGBT) from Semikron (SKM-600GA-12T4) as a switch⁶. The breakdown voltage of the IGBT is 1200 V, the maximum current rating is 600 A. The time required for the current flowing through the IGBT to go from 90 % of its initial value to 10 % of its initial value is $0.6 \mu\text{s}$. These values were taken from the datasheet of the SKM-600⁷.

Figure 4.12 (b) shows a more accurate model that takes into account several non-ideal characteristics of the IGBT (the input capacitances with each of the terminals). These non-ideal characteristics are described in Ref. [39]. For switching, the input capacitances C_1, C_2 and C_3 must charge and discharge rapidly. If these are not taken into account, the capacitors will severely limit the switching time of the transistor. For this purpose, we use a commercially available IGBT driver (SKHI 10/17 R). A custom made interface guarantees fast signal transfer with the driver and protects it from voltage spikes coming from the power supply. The full interface diagram and the printed circuit board are shown in appendix B.

⁶The working principle of IGBTs can be found in Ref. [39].

⁷The convention followed in the datasheets of the power transistor can be confusing. For an explanation of this convention see Ref. [39].

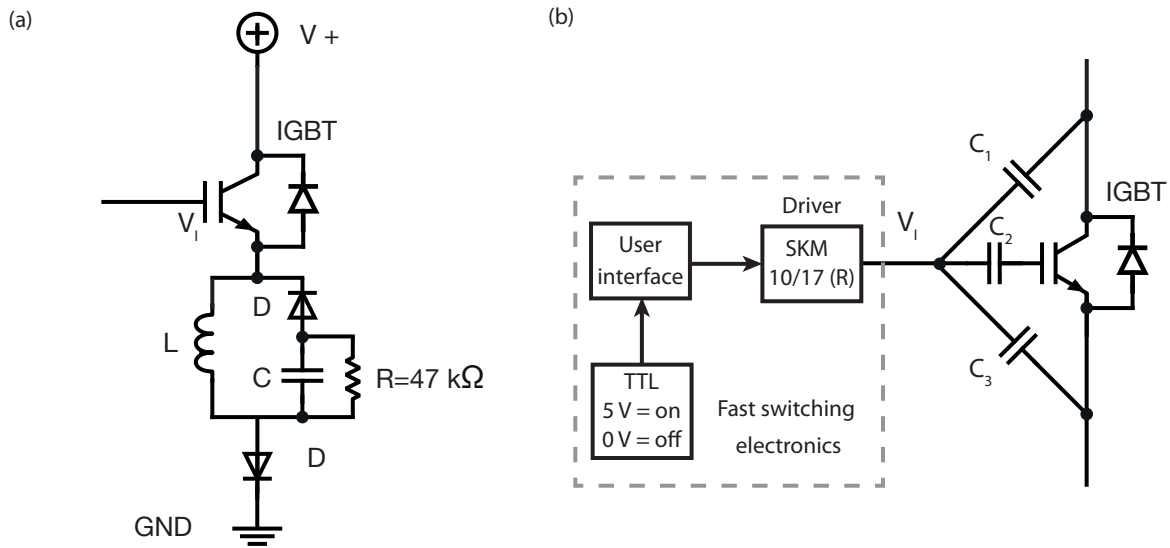


Figure 4.12: (a) Simplified schematic of the switching circuit. An insulated gate bipolar transistor, (IGBT), acts as a switch for the current. When the current is switched off, the LC circuit starts oscillating and the capacitor gets charged. The diode prevents the capacitor of discharging through the coils, and in a time given by, $\tau = C R$ the capacitor discharges through the resistor (b). Description of a more accurate model for a non-ideal IGBT. The input capacitances limit the charge and discharge time of the gate voltage V_L limiting the total switching characteristics.

To control the discharge time of the coils we use a capacitor parallel to them.

The capacitor and the inductor form an LC circuit which follows the equation:

$$\frac{d^2}{dt^2} I(t) = \frac{I(t)}{C L}. \quad (4.48)$$

When the current is switched off, the LC circuit starts oscillating and the energy stored in the magnetic field is transferred to the capacitor. The solutions of Eq. (4.48) is:

$$I(t) = I_0 \cos\left(\frac{t}{\sqrt{L C}}\right), \quad (4.49)$$

where we have used the initial conditions:

$$I(t = 0) = I_0 \quad \frac{dI}{dt}(t = 0) = 0 \quad (4.50)$$

Note that Eq. (4.49) predicts that the current oscillates, transferring the energy from the capacitance back to the coils (see Fig. 4.13 (a), red curve). The diode prevents this transfer of energy from happening as shown in the black dotted curve of Fig. 4.13 (a). Due to the finite response time of the diode, the current overshoots slightly as depicted in the blue curve of Fig. 4.13 (a)

The capacitor then discharges through the resistor on a timescale given by:

$$\tau = R C. \quad (4.51)$$

Where R is the resistance of the resistor, in our case 47 kΩ. This value must be chosen to be shorter than the experimental cycle time.

The first zero crossing of the current follows the relation;

$$\frac{t}{\sqrt{LC}} = \frac{\pi}{2}. \quad (4.52)$$

From the discharge curves of Fig. 4.13 (b) and using Eq. (4.52) the inductance can be measured. The first zero crossing of the current occurs 0.13 ms after the switching starts⁸. In this case, the capacitor used was a $30 \pm 3 \mu\text{F}/1200\text{V}$ GTO MKP from WIMA. This gives a total inductance of the coils to be $L = 228 \pm 20 \mu\text{H}$.

The voltage drop through the coils as a function of time follows the relation:

$$V = L \frac{dI}{dt} = I_0 \sqrt{\frac{L}{C}} \sin\left(\frac{t}{\sqrt{LC}}\right). \quad (4.53)$$

From equation Eq. (4.53) follows that the peak voltage during switching, V_{max} is :

$$V_{max} = I_0 \sqrt{\frac{L}{C}}. \quad (4.54)$$

For switching a $15 \mu\text{F}$ capacitor from WIMA($15 \mu\text{F}/1500\text{V}$ GTO MKP) will be used. The maximum voltage will be $V_{max} \approx 570\text{V}$.

One of the main advantages of this system, is that the switching timescales are independent of the switching current, as shown in Fig. 4.13 (b).

4.4 Coil Geometry Optimization

In the following we will follow the convention shown in the figure Fig. 4.14 to denote as N_r the number of windings in the radial direction and N_z to denote the number of windings on the vertical direction. Figure 4.14 shows the optimized coil geometry. The geometry was optimized based on three factors:

- We need to minimize the inductance of the coils to improve the switching time.

⁸The switching time can controlled by using a different capacitor. A $15 \mu\text{F}/1500 \text{V}$ GTO MKP from WIMA will give faster switching times

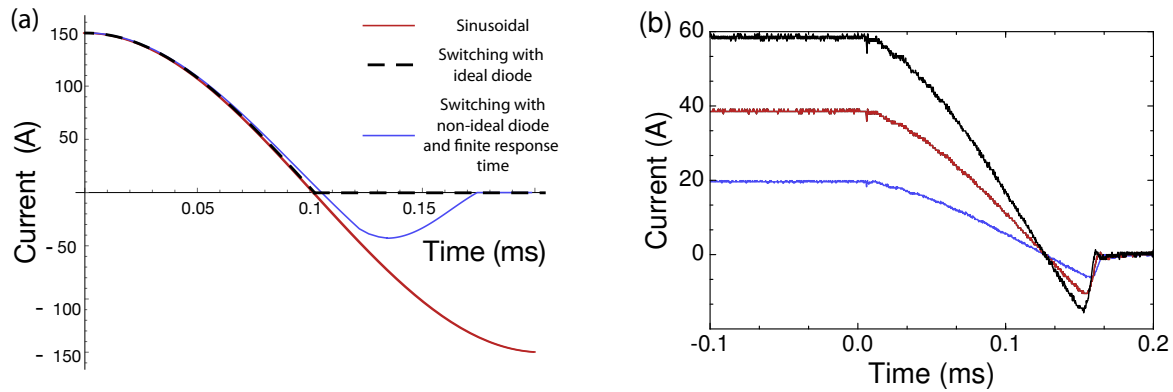


Figure 4.13: (a) Expected switching characteristics of the circuit shown in Fig. 4.12. Without the diode the current oscillates sinusoidally (red curve). The diode prevents the oscillation from happening (black dotted curve), and the capacitor discharges through the $47\text{ k}\Omega$ resistor. Due to the finite response time of the diode, the current overshoots slightly (blue curve). (b) Measured switching characteristics of the circuit of Fig. 4.12 (a). The switching timescales are independent of the current. The amplitudes depend linearly on the current. We measure the switching time to be $t \approx 0.13\text{ ms}$. For faster switching times a capacitor with lower capacitance could be used. For measuring this discharge curve we used a power supply from Elektro-Automatik (40 V 60 A PS 804060)

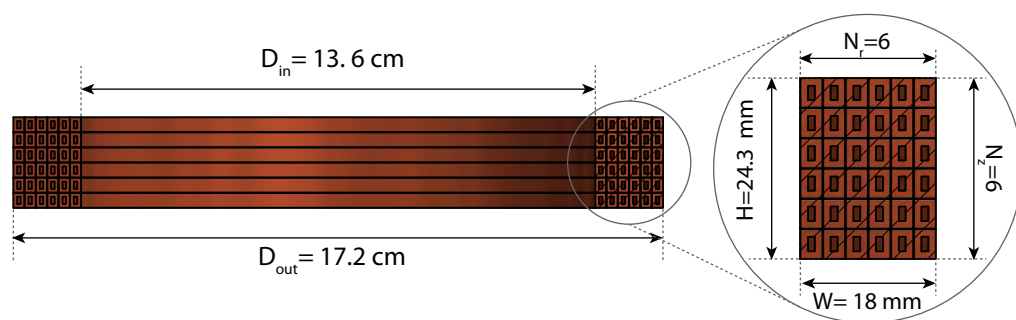


Figure 4.14: Cross section of the optimized coil geometry. We used $N_r=6$ windings in the radial direction, N_r and $N_z=6$ windings in the vertical direction.

- Due to the limitation of the total available current from our power supply (200 A), the current to obtain the desired field gradient must be smaller than this value of 200 A. The total output of the power supply is 400 A, as we intent to run both sets of coils with a single power supply, the total available current for each of the coils is 200 A.
- The interference of the magnetic system with other parts of the experiment must be minimal. The angle that the coils cover, viewed from the center point of the chamber (the desired position of the MOT cloud), must kept as large as possible.

To optimize the geometry, the first step was to calculate the off-axis magnetic field created by a circular loop of current. Assuming infinitely thin wire, the field can be calculated in terms of elliptical integrals as given in Ref. [30]:

$$\begin{aligned} B_z^1(z, \rho, R, I) &= \frac{\mu_0 I}{2 \pi} \frac{1}{\sqrt{(R + \rho)^2 + z^2}} \left[\frac{R^2 - \rho^2 - z^2}{(R - \rho)^2 + z^2} E(k^2) + K(k^2) \right], \\ B_\rho^1(z, \rho, R, I) &= \frac{\mu_0 I}{2 \pi} \frac{z/\rho}{\sqrt{(R + \rho)^2 + z^2}} \left[\frac{R^2 + \rho^2 - z^2}{(R - \rho)^2 + z^2} E(k^2) - K(k^2) \right], \end{aligned} \quad (4.55)$$

where

$$k^2 = \frac{4 R \rho}{(R + \rho)^2 + z^2} \quad (4.56)$$

and $K(k^2)$ and $E(k^2)$ are the complete elliptical integrals of first and second kind respectively. Here, $B_z^1(z, \rho, D, R)$ is the magnetic field along the z axis and $B_\rho^1(z, \rho, D, R)$ is the magnetic field along the radial axis.

To compute the magnetic field, we need to add the field created by each of the current loops shown in Fig. 4.14:

$$\begin{aligned} B_z^{N_r \times N_z}(z, \rho, R, I) &= \sum_{j=1}^{N_z} \sum_{i=1}^{N_r} B_z(z - j \Delta_z, \rho, R + i \Delta_r), \\ B_\rho^{N_r \times N_z}(z, \rho, R, I) &= \sum_{j=1}^{N_z} \sum_{i=1}^{N_r} B_\rho(z - j \Delta_z, \rho, R + i \Delta_r), \end{aligned} \quad (4.57)$$

where Δ_z is the height of the wire, the superscript $N_r \times N_z$ indicates the number of wire loops on each direction and Δ_r and Δ_z are the width and height of the wire respectively (see Fig. 4.5). (For our system $\Delta_z = 0.4$ mm and $\Delta_r = 0.3$ mm). We have chosen this values as it allows us to have more windings closest to the atoms. Alternatively one could rotate the wire to have $\Delta_r = 0.4$ mm, however we found this to be overall a less efficient configuration.

Equation (4.57) allows us to predict the field that each coil depending on its inner radius and the number of current loops used in each direction. The flux given by Eq. (4.57)

through the coils can be approximated as:

$$\phi \approx N_r \sum_{n=1}^{N_z} \int_{\rho=0}^{\rho=R} N_r \times N_z B_z(z = \Delta_r n, \rho, R, I) \pi \rho d\rho. \quad (4.58)$$

And the self-inductance follows from the relation:

$$L = \frac{\phi}{I}. \quad (4.59)$$

The equations so far might seem complicated, but a numerical calculation can be easily performed. To check whether the calculation of the self-inductance done in this manner is reliable, we compared the calculations with the measured inductances for different coils. We obtained an agreement of 10 % between the predicted value L_p and the measured value L_m ($\Delta L/L_m < 10\%$). For the coil system described in Fig. 4.14, we predict a self-inductance of 220 μH . This value is in agreement within error bars to the measured value of $228 \pm 20 \mu\text{H}$ (see section 4.3). Comparing this calculated value with the one obtained using Eq. (4.21) of 140 μH we see a important improvement. Equation (4.21) follows from Eq. (4.59) and using the expected scaling of the number of coils squared ($L \propto N^2$). However, this scaling is only valid if the coils are infinitely thin and therefore occupy the location in space. Moreover the approximation done in Eq. (4.22) can be incorrect.

We calculated the self-inductance for different coil configurations, and using Eq. (4.47), calculated the expected switching time for a IGBT with 1000 V breakdown voltage (see section 4.3) to obtain the data presented in Fig. 4.15 (a).

The field gradient at the origin created by the coil pair can be calculated as:

$$\frac{d}{dz} \left[B_z^{N_r \times N_z}(z - D/2, \rho, R, I) + B_z^{N_r \times N_z}(z + D/2, \rho, R, -I) \right] (z = 0) \quad (4.60)$$

Equation (4.60) allows us to obtain the current needed for each configuration. The results of these calculations are shown in Fig. 4.15. (b)

Figures 4.15 (a) and (b) also show the behaviour predicted by Eq. (4.25) in section 4.1.2. The configurations that require the lowest currents are the ones that have the highest inductance and therefore slower switching. More importantly, the configurations with lower current requirements are larger, and they maintain a lower solid angle from the center of the chamber.

For these reasons, we use as higher current as possible. We set an upper limit of 160 A (20 % lower than the available current from the power supply). This limit is given by the precision of our calculations for the field and the self-inductance of 10 %, and we add extra 10%. This extra 10% is arbitrarily added to guarantee that the system could be operated with the available equipment. The points in the grey area of Fig. 4.15 (b) correspond to points within the 140 A to 160 A region.

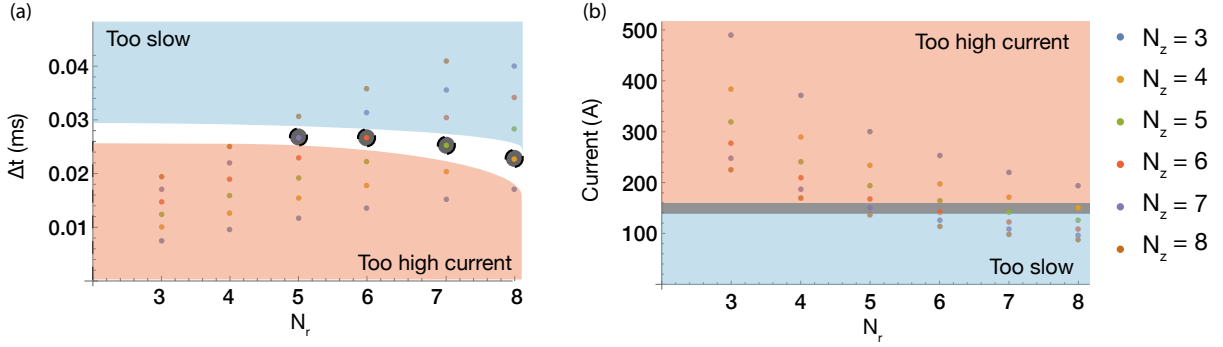


Figure 4.15: (a) Self-inductance of different coil geometries (different N_r and N_z). (b) Current for different coil geometries. The points contained in the grey area corresponds to configurations with currents in the region around 150 A. The corresponding points have been highlighted in (a). The points contained in the light red area were considered to have high current requirements, while the points in the blue area were considered to have slow switching times. Here we relate the switching time to the breakdown voltage with $\Delta t_{max} = L \Delta I / \Delta V$ and assume a maximum voltage during transient of 1kV. The inner diameter of the coil $D_{in} = 13.6$ cm and an outer diameter is dependent on the number of windings as $N_r \times 0.3$ cm. The height is $N_z \times 0.4$ cm (we follow the convention shown in Fig. 4.14).

The points contained in this area are highlighted in Fig. 4.15 (a) by grey dashed circles. In principle these configurations are the most optimal. They have the fastest possible switching time. The solid angle with respect to the center of the chamber by each of the coils can also be used to discriminate between these configurations. Due to the geometry of the experimental system, the maximum possible outer diameter of the coils is 17.4 cm and the distance between the coils and the atoms is 7.5 cm. Using these values, the angle sustained by each of the coils is given by:

$$\varphi = 2 \left[\frac{\pi}{2} - \arctan \left(\frac{7.5 + N_z 0.41}{8.7 - N_r 0.31} \right) \right]. \quad (4.61)$$

The result of this calculation is given in following table:

Configuration	$\varphi/2$
$N_r = 5, N_z = 7$	31.9°
$N_r = 6, N_z = 6$	31.7°
$N_r = 7, N_z = 5$	31.4°
$N_r = 8, N_z = 4$	31.1°

The solid angle limitation by the vacuum chamber is given by $\varphi/2 = 40^\circ$, which means that any of the former configurations limits the optical access.

To improve the power dissipation of each of the coils we decided to cool different parts of the coils separately. To do this we separated the sets of coils. It is convenient

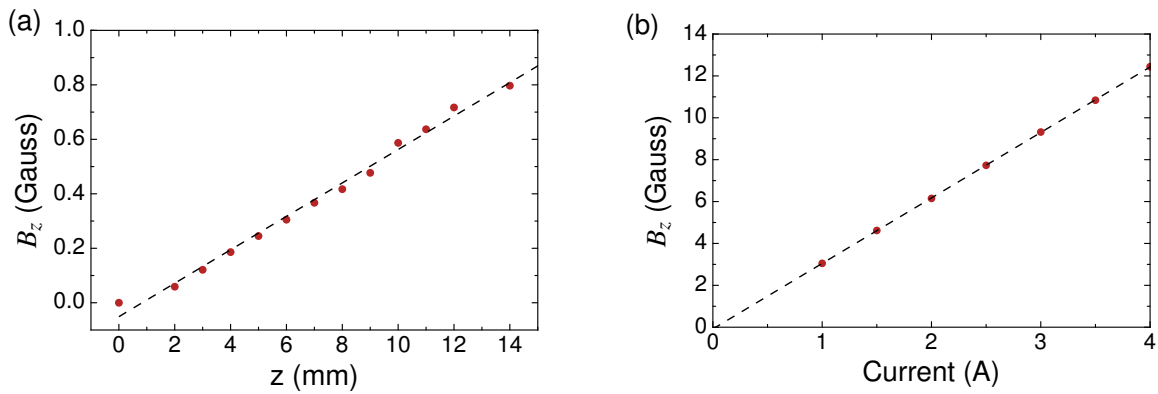


Figure 4.16: (a) Magnetic field in the z axis as a function of position. The red dots represent data-points, while the black dashed line is a fit to the data. The oscillations in the measured magnetic field were created by changes in the background magnetic field (these changes were given by unknown sources and Earth's magnetic field) and changes in the position of our measuring device. The current running through the coils was 2 A (b) Magnetic field at the center of one coil for different currents.

that all the coils forming the set are identical. The $N_r = 6, N_z = 6$ is the configuration that allows this division into identical coils with lower φ . For this reason, we choose this configuration. Therefore, we used 3 different sets of $N_r = 6$ and $N_z = 2$ for each solenoid. The final dimensions of the coils are shown in Fig. 4.14.

Finally, we measured the magnetic field generated by the coils. Figure 4.16 (a) shows the z component of the magnetic field, B_z for the coil system shown in Fig. 4.14 as function of the distance to the center. This values were measured for a current of 2 A and a distance between the coils of 15.4 cm. The red dots represent data-points. The black dashed line represents a linear fit to the data points. For calibration of Earth's magnetic field we subtracted it's value from the data. We determined the center of the symmetry axis of the coils by measuring B_ρ and finding the point where it vanishes. The slope of the linear fit is 0.61 G/cm (standard deviation of 0.01) while our calculation predicts 0.63 G/cm. Figure 4.16 (b) shows the magnetic field strength at the center of one of the coils as a function of the current. The red dots show data-points, while the black dashed line shows a linear fit to the data-points. The fitted slope was 3.12 G/A (standard deviation of 0.007) while the expected slope is given our calculation is 3 G/A.

4.5 Coil Mount Design

In section 4.1.3, we explained that the switching would induce a force change on the coil mount that would create oscillations. These oscillations must be dissipated on a time-scale of 0.1 ms. Two measures were taken to damp these oscillations:

The rods that hold the two mounts together were made from Grade 316Ti stainless

steel. The rods are hollow inside and filled with lead and sand to damp the oscillations. The base is made with PEEK (Polyether ether ketone) a plastic with high mechanical resistance. The coils are clamped to the base and held by friction. To prevent the oscillations from transferring to the experiment, the base is mechanically disconnected from the experimental setup. A drawing of the coil mount is shown in Fig. 4.17.

4.6 Power Dissipation

The IGBT voltage drop in the conducting state is 1.5 V, and the total power dissipated during operation of the blue MOT is 225 W. For the MOSFET in the conducting state, the voltage drop is 1.1 V, and a total dissipated power is 165 W. The diode in its conducting state has a voltage drop of 2 V and a total power dissipated of 300 W. Due to the high power consumption of all of these components, they are actively cooled. These components along with their respective water cooled heat sinks are marked in Fig. 4.18.

For safety reason all these electrical components are mounted inside a box made of HGW 2082.5. The walls of the box are 1 cm thick. To minimize the resistance of each of the components, the internal connections between the different components are made with thick copper bars with cross section $\approx 1\text{cm}^2$. A simplified 3D image of the box, where all the control and switching electronics are missing, is shown in Fig. 4.18.



Figure 4.17: MOT coil mount.

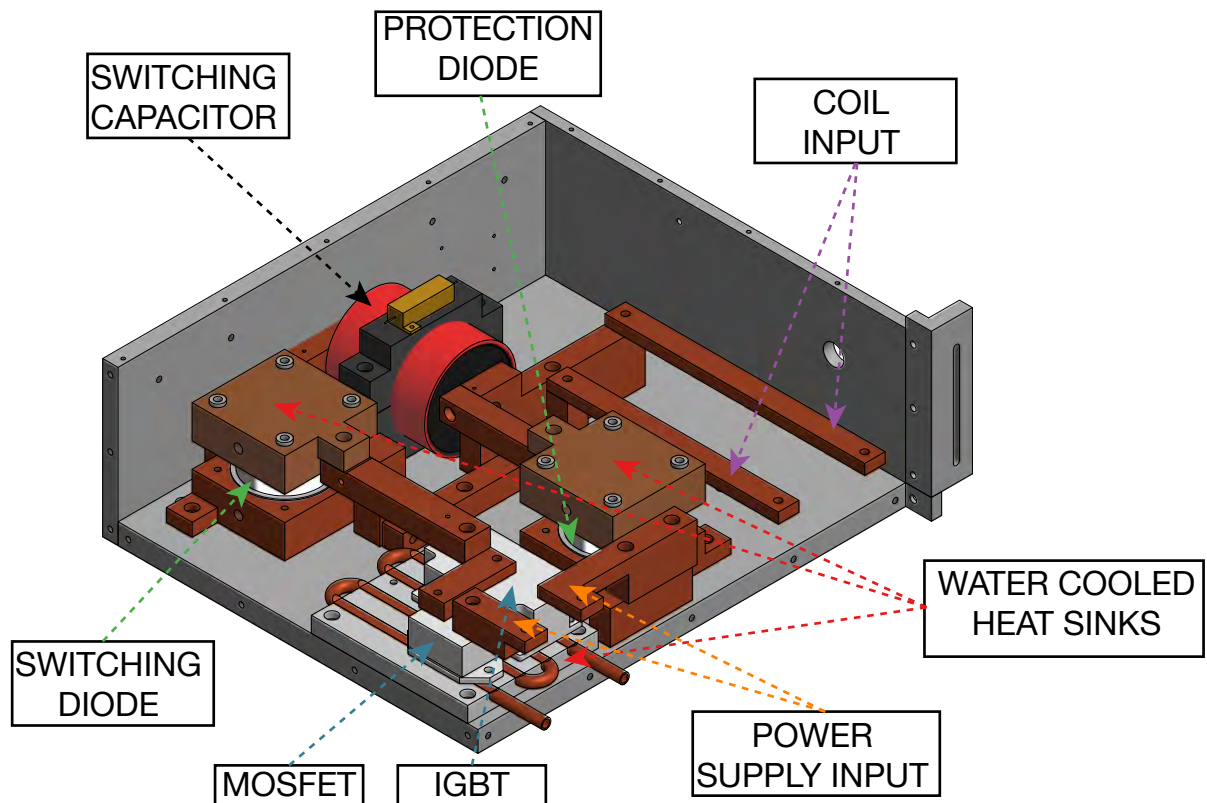


Figure 4.18: Simplified 3D image of the switching box. The current control, switching boards, PI-board and the current transducer were built into the box. In the image these components have been omitted. To monitor the temperature of all the components during switching, a temperature monitoring device was also added to the design, this also has been omitted. As noted in the figure all the elements that handle high power are water cooled. The rest of the components are marked in the figure. In the experiment two of these boxes will be used to switch each of the MOT coils.

4.7 Compensation Coils

To compensate for the offset in the magnetic field of the MOT created by Earth's magnetic field we use 6 sets of coils, two in each of the axes. Additionally, if it is required by the experiment, these coils will allow the possibility to create higher magnetic fields than the magnetic field created by the Earth. The geometry of the compensation coils was determined by the available space in the experimental setup.

For compensation of the magnetic field in the vertical axis we use two identical circular solenoids. The geometry of one of the solenoids is given in Fig. 4.19. In the experiment the solenoids will be at a distance of 15 cm from each other. They are designed to be mounted with the MOT coils in the same base described in Fig. 4.17. With these coils we expect to be able to create a maximum field of 6 G with a current of 1.7 A. For this

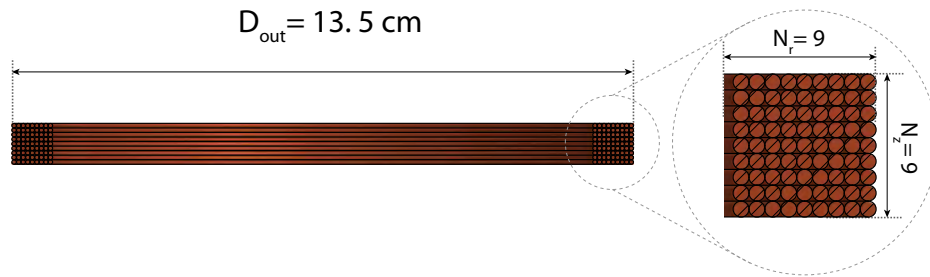


Figure 4.19: Geometry of the solenoid used to compensate the Earth's magnetic field along the z -axis

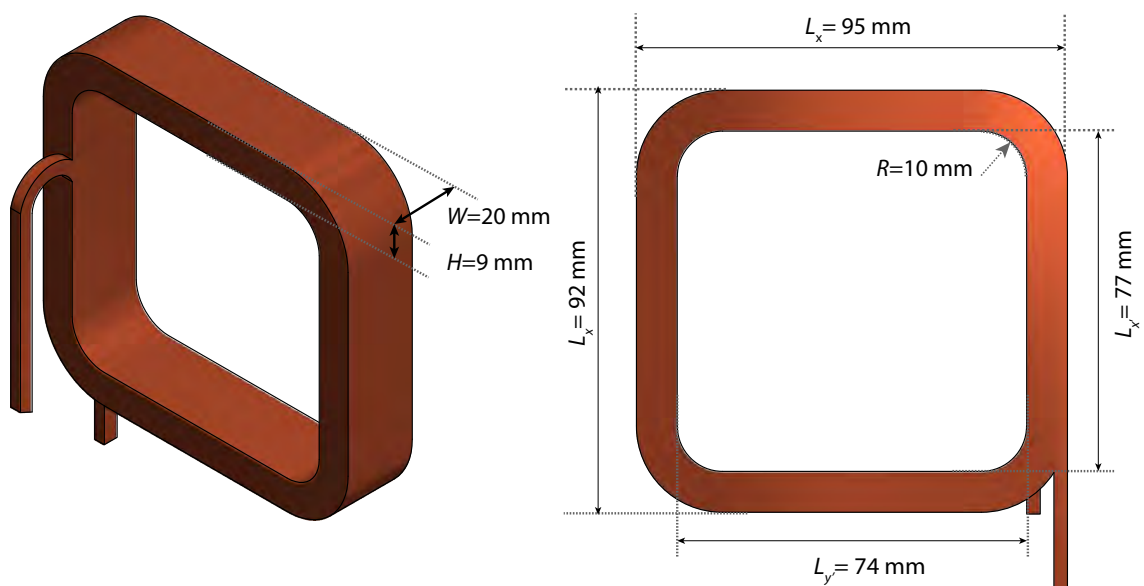


Figure 4.20: Geometry of the coils used to compensate the Earth's magnetic field around the x and y axis.

current the dissipated power is 2 W.

For compensation in the horizontal plane (the plane parallel to the optical table) we will use two pairs of identical coils. These coils will be located at a distance 22 cm from each other. The geometry of one of the coils is described in Fig. 4.20. For these coils we will need a current of 27 A to obtain a field of 6 G on each of the axes. The dissipated power will be 9 W. With such high power the coils will overheat. To avoid the overheating we use the same water cooled wire described in Fig. 4.5. The width W and the height H (see Fig. 4.20) is given by the number of windings on each direction.

$$W = 3 \text{ mm} \times N_W = 9 \text{ mm} \quad H = 4 \text{ mm} \times N_H = 20 \text{ mm} \quad (4.62)$$

where $N_H=5$ and $N_W=3$ is the number of windings in the direction given by H and W respectively.

Acknowledgements

I would like to start with a quote from my supervisor, Dr. Sebastian Blatt. Something that he said one of the first times I came to the Strontium laboratory.

The learning curve is exponential

I must say that when he said this I pictured something more similar to a logarithmic function than an exponential one. I know now how completely wrong I was. He has motivated me to learn about so many different areas of science. Not only in our specific field of ultra-cold quantum gases but also many others. Moreover I learnt that the technical details related to the development of science can also be exiting. For this I would like to thank him. I would also like to thank him for the advice that he gave me while writing this thesis.

I would like to thank Professor Immanuel Bloch for giving me the chance to work in such a great group. I have learned so many different things while working with him and his team. In this sense, I would also like to thank the other members of the group. From the first day I came to the institute I was impressed of how ready they were at the time to answer any questions I might have and to help me find any type of equipment I required. In this sense I would like to especially mention Dr. Ahmed Omran. From Immanuel's team I would also like to thank the kicker table, for those amazing times after lunch that it provided.

I would like to thank my family. My mother as she has been so worried about me since I spent so much time in the lab. I would like to thank my father and my sister for being supportive when I especially needed it. I would also like to thank Alejandro Pasamar, my cousin for worrying about me so much in the last days of my thesis while I was writing it. I would also like to thank my aunt Ines and her family.

I would like to thank the other members of the strontium team. Especially my office mate Annie Jihyun Park for helping during the writing of this thesis, making an exhaustive correcting of my grammar (although not as exhaustive as she would have liked) and in general helping me turn my gibberish into words. I would like to thank Nejc Janša and André Heinz for reading parts of my thesis and correcting them. I would also like to thank them for been such fun colleagues to work with. I thank Dr. Stepan Snigirev for teaching me how to write decent codes in Mathematica, and Python.

I would like to thank the technical staff of the institute, especially Karsten Förster and Anton Mayer, for taking part of their time to answer my questions and in general helping me as much as they possibly could.

I would like to thank my friends, those that are back at home, and those that are here in Munich. For always making me feel at home, independently whether I am in Munich or in Madrid.

Appendices

Appendix A

Hall Probe Sensing Circuit

Figure 21 (Top) shows a schematic of the transducer electronics. The current output of the transducer (coming from pin 6) passes the VPR221sz ultra-stable resistor. A set of jumpers (JP1) allows us to invert the signal when necessary. The gain of a differential amplifier (AD-8429) is set to $G = (1 + \frac{6k\Omega}{R_g}) \approx 4$. A voltage follower (made using a LF356 operation amplifier) monitors the output of the differential amplifier. The terminal "signal in" receives the desired control voltage. A voltage adder made from two operational amplifiers subtracts both voltages. The error signal is sent to a PI controller. In the voltage adder a capacitor is added to filter high frequency noise coming from the transducer. Note that the bandwidth of the transducer is 100 kHz. Figure 22 (down) shows the configuration of the voltage regulators used to power the system. These protect the transducer from over-voltages coming from the power supply. A schematic of the printed circuit board (PCB) is shown in Fig. 22.

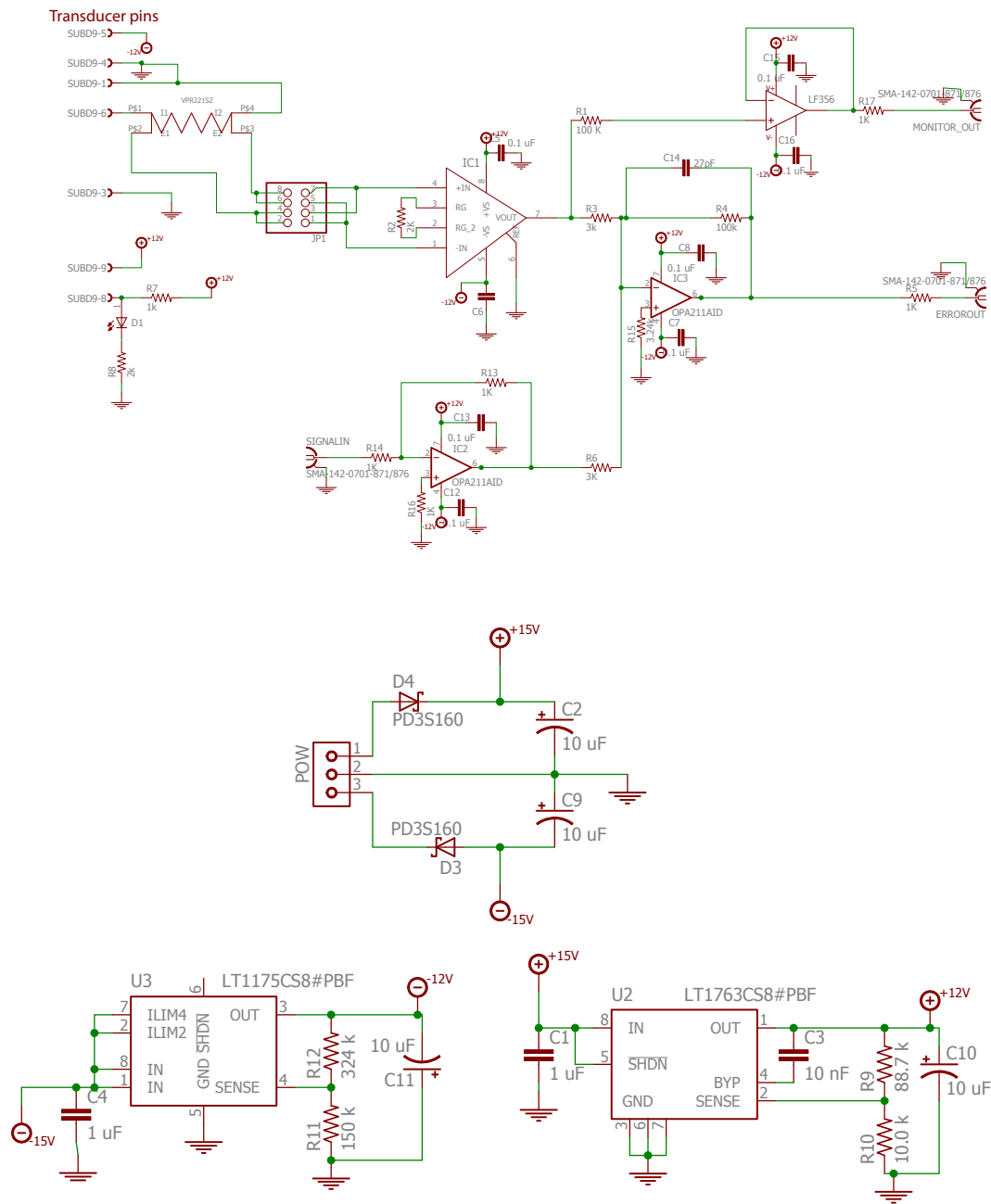


Figure 21: Top: Schematic of the main signal path. Down: Schematic of the voltage regulators.

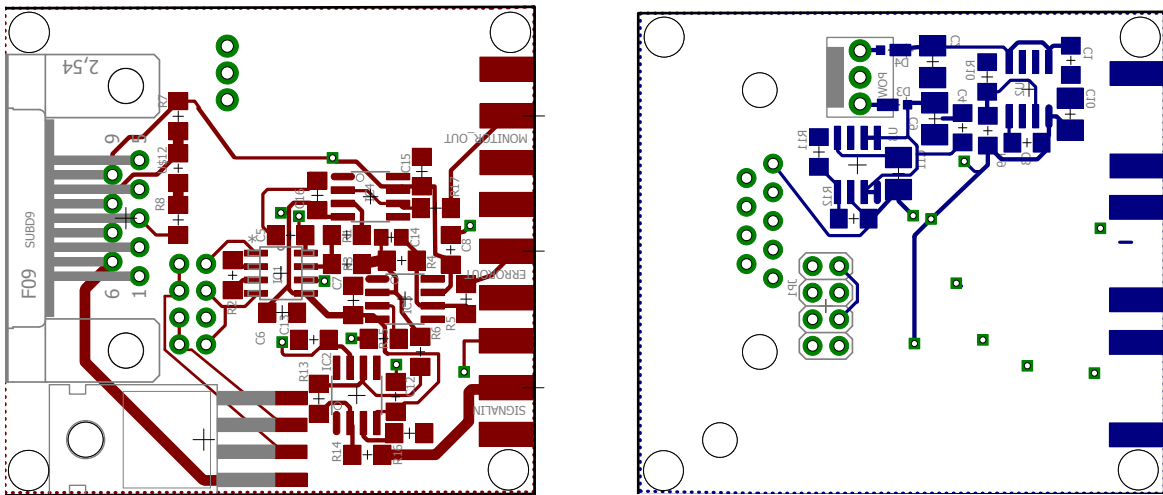


Figure 22: Schematic of the PCB board, left top view, right bottom view. For cleanliness all the ground planes have been omitted.

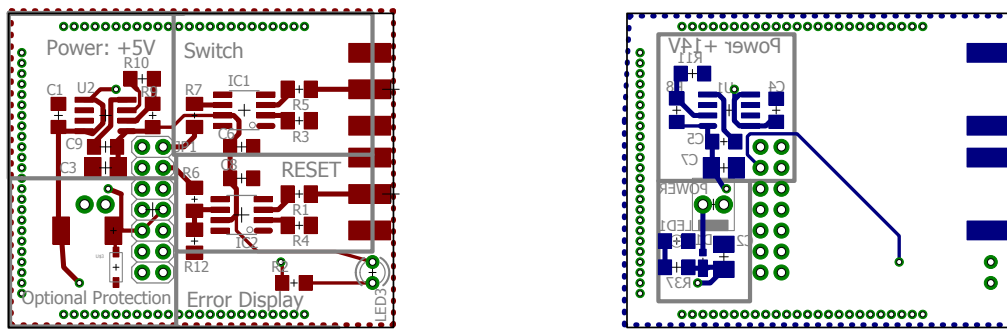


Figure 24: Schematic of the PCB board, left top view, right bottom view. For clearness all the ground planes have been omitted.

Bibliography

- [1] R. Feynman, “Simulating physics with computers,” 1982. (Cited on page 3)
- [2] I. Bloch, J. Dalibard, and S. Nascimbène, “Quantum simulations with ultracold quantum gases,” *Nat Phys*, vol. 8, no. 6293, p. 267–276, 2012. (Cited on page 3)
- [3] J.-y. Choi, S. Hild, J. Zeiher, P. Schauß, A. Rubio-Abadal, T. Yefsah, V. Khemani, D. A. Huse, I. Bloch, and C. Gross, “Exploring the many-body localization transition in two dimensions,” *Science*, vol. 352, no. 6293, pp. 1547–1552, 2016. (Cited on page 3)
- [4] S. Stellmer, *Degenerate quantum gases of strontium*. PhD thesis, University of Amsterdam, 2003. (Cited on pages 3, 5, 13, 14, 15, 47, 49, and 50)
- [5] X. Zhang, M. Bishof, S. L. Bromley, C. V. Kraus, M. S. Safronova, P. Zoller, A. M. Rey, and J. Ye, “Spectroscopic observation of SU(N)-symmetric interactions in Sr orbital magnetism,” *Science*, vol. 345, no. 6203, pp. 1467–1473, 2014. (Cited on page 3)
- [6] T. L. Nicholson, S. L. Campbell, R. B. Hutson, G. E. Marti, B. J. Bloom, R. L. McNally, W. Zhang, M. D. Barrett, M. S. Safronova, G. F. Strouse, W. L. Tew, and J. Ye, “Systematic evaluation of an atomic clock at 2×10^{-18} total uncertainty,” *Nat Commun*, vol. 6, Apr 2015. Article. (Cited on pages 3 and 13)
- [7] W. S. Bakr, J. I. Gillen, A. Peng, S. Folling, and M. Greiner, “A quantum gas microscope for detecting single atoms in a hubbard-regime optical lattice,” *Nature*, vol. 462, pp. 74–77, Nov 2009. (Cited on page 4)
- [8] M. F. Parsons, F. Huber, A. Mazurenko, C. S. Chiu, W. Setiawan, K. Wooley-Brown, S. Blatt, and M. Greiner, “Site-resolved imaging of fermionic ${}^6\text{Li}$ in an optical lattice,” *Phys. Rev. Lett.*, vol. 114, p. 213002, May 2015. (Cited on page 4)
- [9] M. A. Norcia and J. K. Thompson, “Simple laser stabilization to the strontium ${}^{88}\text{Sr}$ transition at 707 nm,” *Review of Scientific Instruments*. (Cited on pages 4, 20, 24, 29, 33, and 44)
- [10] C. Joachain and B. Bransden, *Physics of atoms and molecules*. Prentice Hall, 2 ed., 2003. (Cited on pages 5, 6, and 11)
- [11] H. J. Metcalf and P. van der Straten, “Laser cooling and trapping,” Springer, 1999. (Cited on pages 6, 7, 8, 10, 13, and 48)

- [12] R. Loudon, *The Quantum Theory of Light*. Oxford science publications, 3 ed., 2010. (Cited on pages 7 and 21)
- [13] F. Schwabl, “Statistical mechanics,” ch. 9, pp. 1–19, Springer, 2 ed., 2004. (Cited on page 7)
- [14] D. Diestler and H. Ladouceur, “An alternative derivation of the Wigner-Weisskopf approximation,” *Optics Communications*, Jan 1977. (Cited on page 7)
- [15] C. Pethick and H. Smith, *Bose-Einstein Condensation in Dilute Gases*. Cambridge, 2004. (Cited on page 8)
- [16] Y. Castin, H. Wallis, and J. Dalibard, “Limit of Doppler cooling,” *J. Opt. Soc. Am. B*, vol. 6, pp. 2046–2057, Nov 1989. (Cited on page 11)
- [17] M. M. Boyd, *High Precision Spectroscopy of Strontium in an Optical Lattice: Towards a New Standard for Frequency and Time*. PhD thesis, University of Washington, 2007. (Cited on pages 13 and 14)
- [18] N. Janša, “A frequency-stable diode laser system for spectroscopy and trapping of sr atoms,” Master’s thesis, Ludwig Maximilian University of Munich, 2016. (Cited on pages 13, 15, and 26)
- [19] *The National Institute of Standards and Technology (NIST) database*. September 2016. (Cited on page 13)
- [20] D. S. Barker, B. J. Reschovsky, N. C. Pisenti, and G. K. Campbell, “Enhanced magnetic trap loading for atomic strontium,” *Phys. Rev. A*, vol. 92, p. 043418, Oct 2015. (Cited on pages 14 and 44)
- [21] G. García and J. Campos, “Transition probabilities for triplet levels of Sr(I),” *Journal of Quantitative Spectroscopy and Radiative Transfer*, vol. 39, no. 6, pp. 477 – 483, 1988. (Cited on pages 15, 28, 31, and 34)
- [22] S. Blatt, *Ultracold Collisions and Fundamental Physics with Strontium*. PhD thesis, Leopold-Franzens-Universität Innsbruck, 2011. (Cited on page 20)
- [23] H. Müller-Kirsten, *Basics of Statistical Physics*. World Scientific, 2013. (Cited on pages 21 and 49)
- [24] W. Demtröder, *Laser Spectroscopy: Basic Concepts and Instrumentation*. Springer, 3 ed., 1993. (Cited on page 22)
- [25] S. R. Kurtz, “Mixers as phase detectors,” tech. rep., WJ Communications. (Cited on pages 23 and 27)

-
- [26] G. C. Bjorklund, M. D. Levenson, W. Lenth, and C. Ortiz, "Frequency modulation (fm) spectroscopy," *Applied Physics B*, vol. 32, no. 3, pp. 145–152, 1983. (Cited on page 23)
- [27] D. J. McCarron, S. A. King, and S. L. Cornish, "Modulation transfer spectroscopy in atomic rubidium," *Measurement Science and Technology*, vol. 19, no. 10, p. 105601, 2008. (Cited on page 23)
- [28] K. J. Astrom and R. M. Murray, *Feedback Systems: An Introduction for Scientists and Engineers*. (Cited on pages 29, 59, and 60)
- [29] G. T. Hickman, J. D. Franson, and T. B. Pittman, "Optically enhanced production of metastable xenon," *Opt. Lett.*, vol. 41, pp. 4372–4374, Sep 2016. (Cited on page 34)
- [30] T. Bergeman, G. Erez, and H. J. Metcalf, "Magnetostatic trapping fields for neutral atoms," *Phys. Rev. A*, vol. 35, pp. 1535–1546, Feb 1987. (Cited on pages 45 and 66)
- [31] J. R. Reitz, F. J. Milford, and R. W. Christy, *Foundations of Electromagnetic Theory*. Oxford science publications, 4 ed., 2010. (Cited on pages 47, 49, 50, 51, 52, and 53)
- [32] S. Stellmer, R. Grimm, and F. Schreck, "Production of quantum-degenerate strontium gases," *Phys. Rev. A*, vol. 87, p. 013611, Jan 2013. (Cited on page 49)
- [33] S. Ramo, J. R. Whinnery, and T. V. Duzer, *Fields and Waves in Communication Electronics*. John Wiley & Sons, 3 ed., 1994. (Cited on page 50)
- [34] P. Scherz and S. Monk, *Practical Electronics for Inventors*. Mcgraw hill, 3 ed., 2013. (Cited on pages 52 and 59)
- [35] E. B. Rosa and L. Cohen., *Formulae for Mutual and Self-Inductance*. National Bureau of Standards, 1912. (Cited on page 53)
- [36] H. Nagaoka, "The inductance coefficients of solenoids," *The Journal of the College of Science, Imperial University of Tokyo*, vol. 27, Aug 1909. (Cited on page 53)
- [37] "Hall effect sensing and application," tech. rep., Honeywell. (Cited on page 57)
- [38] "High precision current transducers," tech. rep., LEM. (Cited on page 57)
- [39] M. H. Rashid, *Power Electronics Handbook*. Academic press, 3 ed., 2011. (Cited on pages 59 and 62)
- [40] T. Gantner, "Magnetic trapping of Lithium-6 and Lithium-7," Master's thesis, Technical University of Munich and Max Planck Institute of Quantum Optics, 2012. (Cited on page 62)

Declaration

I hereby declare that this thesis is my own work, and that I have not used any sources and aids other than those stated in the thesis.

date of submission

author's signature